

# CORTICAL SURFACE REGISTRATION AND SHAPE ANALYSIS

Ilwoo Lyu

A dissertation submitted to the faculty at the University of North Carolina at Chapel Hill in partial fulfillment of the requirements for the degree of Doctor of Philosophy in the Department of Computer Science in the University of North Carolina at Chapel Hill.

Chapel Hill  
2017

Approved by:

Martin A. Styner

Stephen M. Pizer

Marc Niethammer

John H. Gilmore

Hongtu Zhu

© 2017  
Ilwoo Lyu  
ALL RIGHTS RESERVED

## ABSTRACT

Ilwoo Lyu: Cortical Surface Registration and Shape Analysis  
(Under the direction of Martin A. Styner)

A population analysis of human cortical morphometry is critical for insights into brain development or degeneration. Such an analysis allows for investigating sulcal and gyral folding patterns. In general, such a population analysis requires both a well-established cortical correspondence and a well-defined quantification of the cortical morphometry. The highly folded and convoluted structures render a reliable and consistent population analysis challenging. Three key challenges have been identified for such an analysis: 1) consistent sulcal landmark extraction from the cortical surface to guide better cortical correspondence, 2) a correspondence establishment for a reliable and stable population analysis, and 3) quantification of the cortical folding in a more reliable and biologically meaningful fashion.

The main focus of this dissertation is to develop a fully automatic pipeline that supports a population analysis of local cortical folding changes. My proposed pipeline consists of three novel components I developed to overcome the challenges in the population analysis: 1) automatic sulcal curve extraction for stable/reliable anatomical landmark selection, 2) group-wise registration for establishing cortical shape correspondence across a population with no template selection bias, and 3) quantification of local cortical folding using a novel cortical-shape-adaptive kernel.

To evaluate my methodological contributions, I applied all of them in an application to

early postnatal brain development. I studied the human cortical morphological development using the proposed quantification of local cortical folding from neonate age to 1 year and 2 years of age, with quantitative developmental assessments. This study revealed a novel pattern of associations between the cortical gyrification and cognitive development.

## ACKNOWLEDEMENTS

I would like to express my gratitude to people who have supported my research and dissertation. First, I thank my advisor Martin Styner for his patience, encouragement, and guidance during the past five years. He was the best advisor, mentor, and friend I ever met. Without his supports, I won't be able to pursue my academic career. He taught me scientific principles in the field, helped me achieve all the doctoral milestones, and inspired me with his outstanding passion and dedication in research.

I also thank all my committee members. Stephen Pizer has been extremely eager to help me improve my writing skills and to provide his valuable feedback to my research. I learned his immense knowledge and understanding of the field. I thank John Gilmore for sharing his expertise and collaboration. I also thank Marc Niethammer and Hongtu Zhu for their insightful suggestions on my research.

I would like to thank my collaborators and fellow students in my department: Sun Hyung Kim, Joohwi Lee, Minjeong Kim, Colin Compas, Hongzhi Wang, Yu Cao, Sangwoo Cho, Junpyo Hong, Yaozong Gao, etc. In particular, Sun Hyung was my best collaborator. He helped me develop ideas and shared his knowledge. Joohwi was always happy to discuss interesting research topics. Minjeong helped me a lot especially for the first year of my study. Colin, Hongzhi, and Yu made me feel comfortable during my entire internship at IBM.

I thank all my Korean friends for giving me positive energy: Jonghyun Park, Ju-Hwan Kim, Jihoon Park, Minjun Cha, Junwoo Kim, Wontae Kim, Cheolgyu Park, Pil-Jae Rue,

Hyungil Seo, Hyunggu Jung, Kijung Yoon, Yong Jin Park, Sangwook Yoo, Donghoon Sagong, Junseong Lee, Min Kim, Yukyung Choi, Geunmok Park, etc.

Lastly, and most importantly, I would like to thank my family members for their invaluable support. My parents contributed hugely to this long journey with unconditional support and boundless patience. My father has been another best life/academic mentor, my mother always endless loves me, and my sister Saemee Lyu has been together as my great friend thus far. I really thank and miss my old friend Cha-dol who had stayed for a long time with me. I will keep my memories with him forever. I dedicate this dissertation to all my friends, dear family, and lovely wife YooJin Jung.

## TABLE OF CONTENTS

<b>LIST OF FIGURES</b> . . . . .	<b>xiii</b>
<b>LIST OF TABLES</b> . . . . .	<b>xvi</b>
<b>Chapter 1: Introduction</b> . . . . .	<b>1</b>
1.1 Overview . . . . .	1
1.2 Previous Work . . . . .	3
1.2.1 Sulcal Landmark Extraction . . . . .	3
1.2.2 Sulcal Landmark Labeling . . . . .	5
1.2.3 Cortical Surface Correspondence . . . . .	6
1.2.4 Quantification of Cortical Folding . . . . .	9
1.2.5 Cortical Morphological Development in Early Stage . . . . .	11
1.3 Thesis Statement . . . . .	12
1.4 Overview of Chapters . . . . .	13
<b>Chapter 2: Background</b> . . . . .	<b>15</b>
2.1 Cortical Surface Reconstruction . . . . .	15
2.2 Curvature Metrics . . . . .	17
2.3 Spherical Harmonic Basis Functions . . . . .	19
2.4 Entropy for Group-wise Surface Correspondence . . . . .	21

2.5	Wavefront Propagation . . . . .	23
<b>Chapter 3: Automatic Sulcal Curve Extraction on the Cortical Surface . .</b>		<b>25</b>
3.1	Overview . . . . .	25
3.2	Objective . . . . .	26
3.3	Slicing and Contour Extraction . . . . .	27
3.4	Sulcal Point Detection . . . . .	29
3.5	Curve Delineation . . . . .	31
3.6	Materials . . . . .	34
3.7	Results . . . . .	35
3.7.1	Noise Sensitivity . . . . .	36
3.7.2	Reproducibility . . . . .	36
3.8	Summary . . . . .	39
<b>Chapter 4: Robust Estimation of Surface Correspondence . . . . .</b>		<b>41</b>
4.1	Overview . . . . .	41
4.2	Preprocessing . . . . .	43
4.2.1	Automatic Sulcal Curve Labeling and Landmark Correspondence . .	43
4.2.2	Rigid Transformation for Initial Alignment on Sphere . . . . .	44
4.3	Landmark-based Pair-wise Surface Correspondence . . . . .	45
4.3.1	Objective . . . . .	45
4.3.2	Consistent Displacement Encoding Scheme . . . . .	46
4.3.3	Initial Deformation Field . . . . .	47
4.3.4	Optimization . . . . .	48

4.3.5	Optimal Pole Selection . . . . .	50
4.4	Extension to Group-wise Surface Correspondence . . . . .	51
4.4.1	Objective . . . . .	51
4.4.2	Entropy of Landmark Errors . . . . .	53
4.4.3	Entropy of Multidimensional Geometric Properties . . . . .	55
4.4.4	Entropy Minimization . . . . .	55
4.4.5	Hierarchical Optimization . . . . .	56
4.5	Shape Correspondence Evaluation . . . . .	58
4.5.1	Average Shape Model Construction . . . . .	58
4.5.2	Correspondence Evaluation via Surface Coloring . . . . .	58
4.6	Materials . . . . .	59
4.6.1	Macaque Cortical Dataset . . . . .	59
4.6.2	IBIS Paediatric Cortical Dataset . . . . .	60
4.6.3	Non-human Primate Molar Shape Dataset . . . . .	61
4.7	Results . . . . .	61
4.7.1	Optimal Pole Selection . . . . .	62
4.7.2	Sulcal Curve Variability . . . . .	64
4.7.3	Variance over Sulcal Depth Maps and Cortical Thickness . . . . .	65
4.7.4	Visual Validation on Macaque Dataset . . . . .	65
4.7.5	Evaluation of Average Shape Models . . . . .	66
4.7.6	Principal Component Analysis on Molar Shapes . . . . .	67
4.8	Summary . . . . .	69

<b>Chapter 5: Sulcal Shape-Aware Quantification of Cortical Folding . . . . .</b>	<b>71</b>
5.1 Overview . . . . .	71
5.2 Objective . . . . .	72
5.3 Outer Hull Creation and Correspondence Establishment . . . . .	75
5.4 Sulcal/Gyral Curve Extraction . . . . .	75
5.5 Travel-time Map . . . . .	76
5.6 Tensor Field . . . . .	77
5.6.1 Principal Propagation Direction . . . . .	77
5.6.2 Principal Propagation Speed . . . . .	78
5.6.3 Tensor Matrix . . . . .	80
5.7 Adaptive Kernel and Local Gyrification Index . . . . .	80
5.8 Materials . . . . .	83
5.8.1 IBIS Living Phantom . . . . .	84
5.8.2 KIRBY Dataset . . . . .	84
5.8.3 Simulated Cortical Folding . . . . .	84
5.9 Results . . . . .	87
5.9.1 Reproducibility . . . . .	87
5.9.2 Evaluation of Simulated Cortical Folding . . . . .	90
5.9.3 A Choice of Kernel Size . . . . .	91
5.10 Methodological Issues . . . . .	92
5.10.1 Local Gyrification Index . . . . .	92
5.10.2 Cortical-Shape-Adaptive Kernel . . . . .	95
5.10.3 Computation Issues . . . . .	96

5.11 Summary . . . . .	97
<b>Chapter 6: Cortical Morphometry and Cognitive Development in Early Post-natal Stage . . . . .</b>	<b>99</b>
6.1 Overview . . . . .	99
6.2 Objective . . . . .	99
6.3 The UNC Early Brain Development Studies (EBDS) . . . . .	100
6.3.1 MR Image Acquisition . . . . .	100
6.3.2 Mullen Scales of Early Learning (MSEL) . . . . .	101
6.3.3 Data Exclusion Criteria . . . . .	102
6.3.4 Surface Model Reconstruction and Local Gyrification Index . . . . .	102
6.4 Linear Mixed Model for the Longitudinal Study . . . . .	105
6.5 Findings of Early Morphometry and Cognitive Development . . . . .	106
6.5.1 Cortical Gyrification in Early Stage . . . . .	106
6.5.2 Association of Cognitive Development . . . . .	109
6.5.3 Comparisons with FreeSurfer . . . . .	110
6.6 Summary . . . . .	116
<b>Chapter 7: Summary and Conclusion . . . . .</b>	<b>118</b>
7.1 Summary of Contributions . . . . .	118
7.2 Limitations . . . . .	121
7.3 Future Work . . . . .	123
7.3.1 Computational Issues . . . . .	123
7.3.2 Applications . . . . .	124

REFERENCES . . . . . 126

## LIST OF FIGURES

1.1	Schematic overview of the entire pipeline . . . . .	14
3.1	Schematic overview of the sulcal curve extraction . . . . .	27
3.2	Contour extraction . . . . .	29
3.3	Sulcal point detection . . . . .	30
3.4	Schematic overview of the line simplification method . . . . .	30
3.5	Candidate sulcal points . . . . .	32
3.6	Endpoint detection . . . . .	34
3.7	An example of estimated endpoints . . . . .	35
3.8	Robustness to noise . . . . .	37
3.9	Sulcal curve extraction . . . . .	38
3.10	Sulcal curve extraction errors . . . . .	39
4.1	Schematic overview of the pair-wise method . . . . .	42
4.2	Schematic overview of the spectral matching . . . . .	44
4.3	Landmark distribution after applying different methods . . . . .	45
4.4	Displacement encoding and estimated deformation field . . . . .	47
4.5	Artifacts in the standard polar coordinate system and reduced artifacts . . . . .	51
4.6	Schematic overview of the group-wise registration . . . . .	52
4.7	Cortical surface coloring . . . . .	59
4.8	Primate fossil molar shapes . . . . .	62
4.9	Reconstruction errors . . . . .	63
4.10	Sulcal curve alignment by different methods . . . . .	64

4.11	Visual comparison of correspondence results . . . . .	66
4.12	Average model reconstruction . . . . .	67
4.13	Shape correspondence evaluation using reconstruction error . . . . .	68
4.14	Primate fossil molar shape space . . . . .	69
5.1	Schematic overview of the local gyrification index . . . . .	73
5.2	Overview of the tensor field computation . . . . .	74
5.3	Two different types of synthetic normalized travel-time maps . . . . .	81
5.4	Kernels at an arbitrary point using different approaches . . . . .	83
5.5	Simulated equally-spaced sulci . . . . .	86
5.6	Reproducibility . . . . .	89
5.7	Local gyrification index of the sine waved plane . . . . .	91
5.8	The average local gyrification indices on the Kirby dataset . . . . .	93
6.1	Pearson’s correlation coefficients of the early childhood brain dataset . . . . .	103
6.2	Correlation of gyrification index within subject . . . . .	107
6.3	Age effect on cortical gyrification . . . . .	108
6.4	Gender effect on cortical gyrification . . . . .	109
6.5	Gestational age effect at birth on cortical gyrification . . . . .	109
6.6	Raw association with cognitive development using optimal kernel size . . . . .	111
6.7	Corrected association ( $q < 0.05$ ) with cognitive development . . . . .	112
6.8	Local gyrification change over age and its association with ELC . . . . .	113
6.9	Comparison: association with demographic effects using large kernel size . . . . .	114
6.10	Comparison: association with cognitive development using large kernel size . . . . .	115

6.10 Comparison: association with cognitive development using large kernel size  
(continued) . . . . . 116

## LIST OF TABLES

4.1	Sulcal curve entropy . . . . .	64
4.2	Variances of cortical properties . . . . .	65
5.1	Average closest distance of the adaptive kernel . . . . .	88
5.2	Coefficient of variation . . . . .	90
6.1	Early brain development studies (EBDS) dataset . . . . .	104

## CHAPTER 1: INTRODUCTION

### 1.1 Overview

Cortical brain morphometric measures such as cortical surface area or thickness have been widely investigated in neuroimaging studies of brain development and degeneration. These measures enable analyses of global or local developmental trajectories over age of anatomical changes and their relationships with cognitive function or environment factors. In addition, quantification of cortical folding has evolved to be an important measure for such cortical analyses. The cortical gyrification is a dynamic process on the cortex involving surface expansion/shrinkage as the number of neurons increases/decreases during brain growth. However, the complete trajectory of cortical gyrification of the human brain is currently unknown, which makes it difficult to determine an optimal measure of cortical folding as no generic ground truth of the trajectory is available. There have been increasing attempts to quantify gyrification in brain developmental studies and pathological disorders via a surface expansion/shrinkage rate over the cortex of adults [2, 67, 35, 110, 56], infants [68, 62, 49], and non-human primates [143, 144]. The main challenge comes from the nature of the cortical shape with its highly complex and variable cortical folding patterns, which hampers the consistency of cortical analyses. Thus, a key aspect to cortical folding analyses is to determine where and how to measure a folding region in a consistent way.

As mentioned above, well-defined quantification of cortical folding is a prerequisite for a

cortical folding pattern analysis. However, the cortical folding patterns are highly complicated and variable in both intra- and inter-subject comparisons, which makes quantification of cortical folding challenging. Even if such quantification is well defined in a single subject, the complexity and variability of the cortical shape yield significant challenges to a population study without an appropriate establishment of inter-subject cortical correspondence. Therefore, successful analyses of cortical folding patterns need to address two critical issues: consistent anatomical/geometric landmark extraction and cortical surface correspondence.

Recently, with the advent of 3D cortical surface reconstruction, fundamental geometric landmarks such as local curvature are easily accessible and thus commonly used in the field of the 3D cortical surface-based analysis. Of many potential geometric properties, it is well-known that sulcal landmarks are one of the most invariant, stable features across cortical regions. Currently, two popular ways exist to define sulcal landmarks. The most prevalent way is based on regional parcellation, given a shape correspondence to a template (or reference) model. However, this approach often suffers from inaccurate boundaries due to high sulcal variability across subjects. Another way is to extract sulcal landmarks without utilizing any predefined template model. In this context, the main advantage comes from no template selection bias, but the approach casts a critical question of how to define/design sulcal landmarks.

A consistent cortical surface correspondence across a population is a significant step in a statistical analysis, providing reliability to better capture population variability as well as to provide reproducibility. To overcome high inter-subject variability, an inclusion of anatomical characteristics such as sulcal landmarks can better support the establishment of cortical correspondence. Particularly, the sulcal fundic regions can serve as robust landmarks in

terms of relative invariance and stability across a population. Once a set of well-described anatomical features is obtained, the next step is to properly fuse those features into the cortical shape correspondence establishment.

To address a cortical shape correspondence problem for a population analysis, the necessary solutions/methods can be separated into the following sub-problem steps:

- Anatomical/geometric landmark extraction
- Cortical surface correspondence
- Quantification of cortical folding patterns
- Population analysis for a brain development study

## **1.2 Previous Work**

### **1.2.1 Sulcal Landmark Extraction**

As discussed already, sulcal fundic regions are known as one of the most invariant, stable features across cortical regions and thus have been widely used as robust features for cortical registration. Sulcal fundic region recognition has been proposed in several studies [81, 111, 71] and employed as critical features for a cortical correspondence [28, 3, 130, 73]

Curvature-based sulcal region extraction methods have been reported in [47, 84, 93, 61]. Curvature measures have the nice property of capturing local, geometric characteristics at a given point. However, such measures are quite sensitive to noise. To alleviate that, a smoothing kernel is commonly employed, which needs to be chosen carefully as otherwise large portions of the surface are smoothed out. Moreover, sulcal curves do not always pass

through points with the maximum curvature, as discussed in [55].

Shi et al. [114] applied the Hamilton-Jacobi equation to the cortical surface to extract sulcal curves by solving the Eikonal equation (a special form of the Hamilton-Jacobi equation). Seong et al. [111] further proposed a more general solver that computes anisotropic geodesics. In their method, the cortical surface is first segmented into seed regions by thresholding a sulcal depth map, and anisotropic skeletons are then computed by solving the Hamilton-Jacobi equation. This method requires careful parameter tuning to determine candidate points that belong to potential sulcal curves. Moreover, since the initial seed regions for the wavefrontal propagation are based on a sulcal depth map, the sulcal curve extraction could be quite sensitive to the initial definition of the seed regions especially in cortical fissures with wide sulcal fundi like the Sylvian fissure.

Sulcal depth information has also been proposed for sulcal curve extraction. Kao et al. [46] used sulcal depth measures to select candidate sulcal points and connected/refined them to have a set of curve segments. Le Troter et al. [55] utilized a geodesic density map using sulcal depth to extract sulcal curves. In this method, sulcal basins are segmented from the cortical surface to compute the shortest geodesic paths between all possible two points of the basins. To determine sulcal points, they compute a density map of the paths that measure how often each vertex belongs to all possible paths. This is based on the assumption that the shortest paths are highly likely to have an intersection with sulcal curves. However, this method is sensitive to initial computation of the sulcal depth map as well as a parcellation of the sulcal basins prior to the processing.

### 1.2.2 Sulcal Landmark Labeling

Many geometric methods discussed above tackled the sulcal landmark extraction problem by exploiting geometric information such as geodesic distance or sulcal depth. However, such a geometry-based approach generally cannot distinguish the primary cortical sulci effectively from the secondary or tertiary sulci without an incorporation of prior knowledge about sulcal landmarks. The recognition of the primary sulci is useful in neuroimaging applications [97, 40], in that they are more consistent in sulcal fundic regions across different brains. For the recognition of sulcal landmarks, one could employ cortical parcellation methods either by analyzing structural neuroimaging data [102, 12] or by combining prior neuroanatomical information and cortical geometry [33]. However, these parcellation-based approaches often suffer from inaccurate boundaries of the cortical parcellation due to the high variability across subjects.

For labeling cortical features, Sandor and Leahy [109] used a manually labeled brain atlas. An atlas encodes neuroanatomical labeling conventions determined by knowledge on structure-function relationships and cytoarchitectonic or receptor labeling properties of regions. Their approach warps the atlas to an individual subject’s cortical surface in order to inherit the labels of cortical features from the atlas. Since this method depends on an atlas registration scheme, it requires a surface correspondence between a template and subjects and generally suffers from a template selection bias. Similar surface-registration methods have been reported in [135, 126, 63, 64, 124].

A graph-based approach was taken in [54, 82]. In this approach, cortical sulci were represented by nodes while their relationships were represented by arcs. The detected sulci

were then labeled based on a manually labeled training set. This approach was further extended to detection of major cortical sulci. In such an approach, joint sulcal shape priors between neighboring sulci were used in the learning process [115]. However, the approach simplified the sulcus detection problem by removing sulcal curves crossing over gyral regions and representing each sulcus as a simple curve. A watershed transform-based approach was presented in [63, 105], in which segmented regions were manually labeled by an expert. Learning-based techniques were also proposed in [106, 5, 132, 96] to detect and label sulci. However, these techniques depend on specific atlas registration schemes [106, 5, 96] or suffer from lacks of neuroanatomical conventions [132]. Graph-based learning techniques were integrated into a public-domain system BrainVisa [107], and cortical sulci that were detected or labeled by this system have been successfully used in many neuroimaging applications [10, 16, 15, 27, 24].

### 1.2.3 Cortical Surface Correspondence

Cortical correspondence methods can be categorized broadly into two main approaches: volume/voxel registration-based [57] and surface model-based registration [92, 65, 73]. While volume-based registration is computed on the three-dimensional image grid, the true structure of the cortical surface is a two dimensional manifold. Volume/voxel based methods in general do not sufficiently incorporate the folding pattern of that cortical surface to allow for a localized analysis [26]. In contrast, localized cortical correspondence is significantly improved with a surface based registration via a cortical surface model. Surface-based registrations can be further categorized as follows: 1) parametrized vs. non-parametrized surface representations and 2) pair-wise registration (individual registration to a template) vs. group-wise registration

(across a population at once).

Cortical surface registration employing parametrized representations is the most prevalent in the field. It is based on mapping the cortical surface onto a specific parametrized space. Several mapping spaces have been proposed including planar [3], hyperbolic [130] or spherical [123, 44] parametrizations. Spherical parametrizations are most popularly used due to their convenience, reduced distortions and computational efficiency [125, 31, 140, 95, 108, 74]. To reduce mapping distortions in parametrization, geometric features (e.g., local curvatures, curvedness, shape index, etc.) have been widely employed in popular pipelines such as Freesurfer. In recent work [69, 3, 130], sulcal landmark features were employed to reduce such mapping distortion. Alternatively, Shi et al. [116] proposed an embedding in the Laplace-Beltrami (LB) space that incorporates a spectral representation to reduce distortions. While these parametrization-based methods are able to provide appropriate parametrized representations, it is noteworthy that all such parametrizations possess significant residual mapping distortions.

Several researchers proposed cortical surface registration in a non-parametrized space. Non-parametric cortical representation is advantageous in that no cortical mapping is required to avoid distortion of the original surface representation. In one such approach, a spectral-based representation is applied to the cortical surface by solving the eigenfunctions of the LB operator, which provides an intrinsic features for cortical surface matching in the spectral domain [89, 65]. In [11, 92], particle-based registration is applied to cortical surface models on which particles are spread such that they establish a group-wise correspondence across subjects. Though these non-parametric methods are free from mapping distortions, it is difficult to establish a continuous correspondence, which necessitates the interpolation of the

implicit deformation field.

The well-studied template-based methods establish a correspondence via a prior template model in a pair-wise manner. Spherical mapping-based methods are most commonly used for cortical registration. Several studies [125, 31, 140, 95] have shown successful pair-wise registration in the spherical space to allow every subject to be aligned to a single template model. Van Essen [136] applied a surface registration method to human and even non-human primate subjects via spherical mapping. Lyttelton et al. [70] further proposed an iterative registration scheme that updates the initial template model for better correspondence establishment. Lyu et al. [73] also proposed a template-based cortical registration via spherical harmonic decomposition of the deformation field. Unfortunately, even if individual correspondence to the template is well developed, these pair-wise methods all possess an inherent bias to the initial template model. The specific template may also be a non-optimal choice for the data at hand, yielding lower sensitivity and specificity in the statistical population analysis.

As reported in [120, 91], group-wise correspondence methods generally yield better statistical shape models. In earlier work [21, 133, 121, 19], a minimum description length (MDL) scheme was proposed to describe shape models across a population in a group-wise manner. Also, Cates et al. [11] adapted an entropy minimization akin to MDL to formulate their particle-based registration without using a template model or prior information. Indeed, MDL under the Gaussian assumption is equivalent to entropy minimization as revealed in [52, 14]. Oguz et al. [92] further refined the particle-based registration by incorporating curvature features, leading to an improved correspondence and tight cortical thickness distributions over the entire cortical surface. However, a particle-based correspondence only

implicitly defines a deformation model without guarantee of topology preservation. In other words, this method is likely to yield over-folding of the cortical surface. Furthermore, this method does not provide an explicit estimation of the deformation field between subjects.

#### 1.2.4 Quantification of Cortical Folding

It is challenging to develop a good metric of cortical folding without deep insight into the developmental trajectory of cortical folding or the modeling of cortical gyrification. In earlier work [142, 85], the so-called gyrification index (GI) has proposed to quantitatively measure cortical folding in the volume space by computing a ratio of the pial<sup>1</sup> perimeter over the outer perimeter for each slice. This provides an easy interpretation of cortical folding by globally capturing the amount of cortical folding in each slice. Despite its clear representation, it comes with several shortcomings as pointed out in [110]. Particularly, it is highly likely for this 2D measure to be biased to a cutting plane selection (e.g., sagittal plane) due to loss of cortical spatial information that is inherently defined in 3D space. In this context, the cortical folding of a buried deep sulcus is rarely captured in a single slice. One can use 3D manual delineation of contours over the entire cortex to overcome such limitations, but this is a highly time-consuming and tedious task.

More recently, approaches have shifted to a 3D surface-based analysis [17, 137], which provides a higher potential for an appropriate cortical shape analysis. Several investigations have also been made based on various geometric representations of cortical folding. In [35],

---

<sup>1</sup> The pia is a membrane that covers the brain underneath the skull.

local mean curvatures computed over the entire cortex were employed as a surrogate local measurement of cortical folding. In [49], local shape analyses were performed using the so-called shape complexity index based on the shape index proposed by Koenderink and van Doorn [51] to measure a local cortical shape change over the years. Batchelor et al. [4] investigated several geometric properties as measures of cortical folding. Similar to the 2D GI, local gyrification can be measured in 3D space by the area ratio between the outer hull and the pial surface [128, 110, 122, 56, 62]. An outer hull-free gyrification index was also proposed in [117, 77]. As such measures are defined locally, regional quantification of cortical folding is generally obtained by computing the corresponding average within a specific region over the cortex.

Though various cortical folding measures have been proposed, there is yet a lack of methods that incorporate cortical shape into the cortical folding representation. Currently, the popular way to compute a local GI measure is instead to employ a kernel defined over the cortical surface: the Euclidean sphere kernel [128, 110], the geodesic distance kernel [35, 49], the nearest neighborhood-ring kernel [56, 62] or the ROI-based kernel [122]. In general, simple local kernel-based approaches tend to describe global cortical folding patterns reasonably well but do not incorporate local cortical shape. The corresponding measures are sensitive to the kernel size as well as the surface reconstruction (e.g., a degree of surface tessellation). Moreover, as these kernel-based methods do not take into account any prior knowledge of sulcal or gyral regions, the kernels merge and eventually smooth out cortical folding measures across the cortex over multiple sulci into a single measurement. Such smoothed multi sulcal/gyral folding measures might be prone to a non-optimal cortical folding analysis, as cortical regions within a single sulcus or gyrus are more functionally related than those

across multiple sulci/gyri [100].

### 1.2.5 Cortical Morphological Development in Early Stage

Several studies have found that the human brain changes dramatically during the early postnatal phase. Total brain volume doubles in the first year of life and reaches 80% of adult volume by the end of the second [50, 38]. Similarly, surface area grows fastest and reaches 70% of adult values in the early postnatal period; as well, cortical thickness exhibits a rapid thickening and reaches 97% of adult values [50, 38]. Cortical changes with respect to cortical thickness and surface area are also correlated to cortical folding development [118, 34]. In addition, the early postnatal phase (from neonate to 2 year) is a critical period in cognitive development [87], e.g., the development of primary sensory processing or language. According to [88], foster care before age 2 helped children have significantly better cognitive outcomes, as compared to kids raised in orphanages. Thus, it is important to investigate the association of cognitive development and brain growth in the early postnatal period. Unfortunately, there is a lack of studies that describe brain growth trajectories particularly in the early stage [39] and their relationship to cognitive development.

The Mullen scale at early learning (MSEL) [86] is a common quantification of cognition in early childhood. The MSEL has 6 major sub-scales quantitatively different aspect of cognition: fine motor, gross motor, visual reception, expressive language, receptive language, and the composite (a combination of all but gross motor). The scores in each category are represented as normalized  $t$ -scores ( $\mu = 50$ ,  $\sigma = 10$ , range=20-80), and the composite is a scaled to IQ score ( $\mu = 100$ ,  $\sigma = 15$ , range=49-155).

### 1.3 Thesis Statement

Thesis: *Template-free group-wise cortical surface correspondence can be established with the support of anatomical/geometric sulcal landmarks. Such cortical correspondence can be employed with a local-shape-adaptive quantification of cortical folding patterns to describe cortical gyrification trajectories in early postnatal brain development.*

The contributions of this dissertation include

1. *A novel sulcal curve extraction method:* Sulcal curves are automatically extracted from the cortical surface in a fashion robust to surface noise. My proposed method achieves high computational efficiency, improves robustness to noise, and high reliability in a scan-rescan dataset as compared to a well-known existing method.
2. *A template-free group-wise cortical surface correspondence:* A population correspondence is established and improved simultaneously in a group-wise fashion free from template selection bias. My novel group-wise registration method allows for local cortical shape analysis in human and non-human primate neuroimaging studies. The proposed method achieves superior results with respect to consistency across subjects as evaluated via quantitative and visual comparisons compared to well-known existing methods.
3. *A cortical-shape-adaptive local gyrification index:* A cortical-shape-adaptive kernel design is proposed to quantify cortical folding patterns. My novel shape-adaptive kernel measures local gyrification on the human cortex. At a higher reproducibility in multi-scan dataset. My proposed method further captures cortical folding in a more biologically and functionally relevant way, as compared to existing gyrification measures.

4. *A description of trajectories of cortical gyrification and early cognition development:*

This dissertation presents an application of my entire framework to a population study of early cortical morphometric development in local gyrification index and cognitive development.

5. *A publicly available software package:* The source codes of the proposed pipeline developed in this dissertation are publicly available at <http://github.com/ilwoolyu/>.

## 1.4 Overview of Chapters

Figure 1.1 illustrates a schematic overview of the entire pipeline proposed in this dissertation. The remainder of this dissertation is organized according to this overview in the following chapters. Chapter 2 provides an overview of the required background in this dissertation, including geometric properties, surface correspondence, quantification of cortical folding, and cortical surface analysis in early development. Chapter 3 presents automatic sulcal curve extraction on the cortical surface without incorporating a template model. Chapter 4 presents cortical surface correspondence modeled by spherical harmonics decomposition via entropy minimization. Chapter 5 presents local gyrification index based on the cortical-shape-adaptive kernel. Chapter 6 presents applications to early development of the human cortex and a relationship between local gyrification and cognitive development. Chapter 7 concludes the dissertation with a discussion of its contributions and some potential future work.

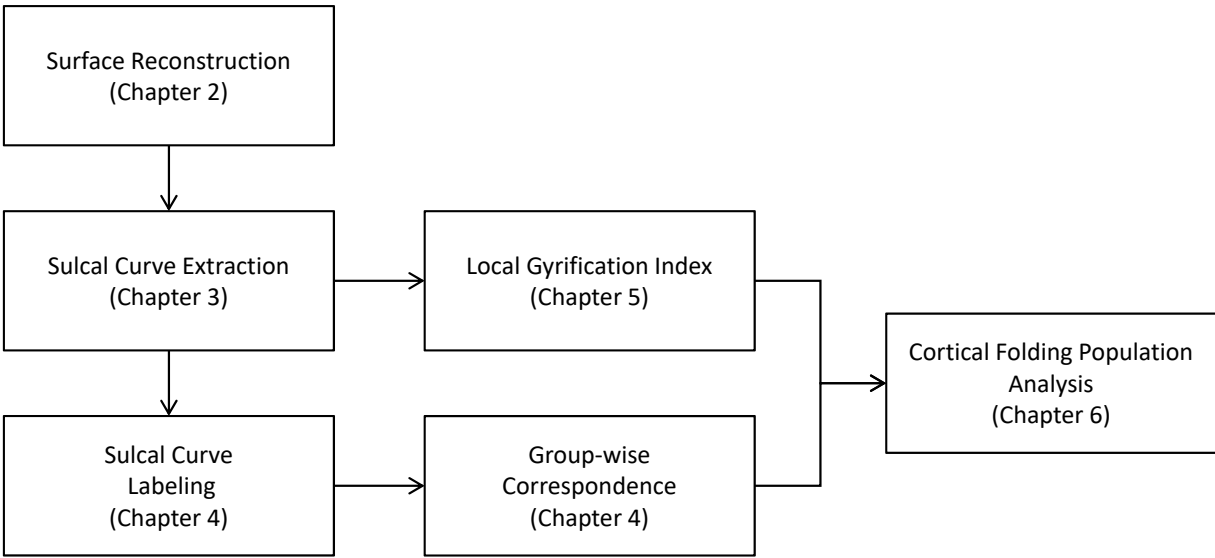


Figure 1.1: A schematic overview of the whole pipeline. A detailed discussion of the individual components is made for each corresponding chapter.

## CHAPTER 2: BACKGROUND

This chapter presents the background materials required for this dissertation. Section 2.1 describes an overview of popular cortical surface reconstruction methods. Section 2.2 provides the description of geometric curvature of smooth surfaces for surface handling and geometric property extraction throughout this dissertation. Section 2.3 briefly summarizes the spherical harmonic basis functions employed for the deformation field representation, and Section 2.4 presents an entropy model to find an optimal geometric property agreement for group-wise surface correspondence. At the end of this chapter, Section 2.5 presents a basic concept of wavefront propagation over the cortical surface model, formulated by the Hamilton-Jacobi partial differential equation (H-J PDE) for geodesic distance computation over surface models.

### 2.1 Cortical Surface Reconstruction

Surface properties can be measured directly from 3D images or reconstructed surfaces. Volume-based approaches to measure cortical surface properties are limited since the spatial information of the cortical surface is inherently defined on a 2D manifold. Due to that limited representation, volume-based approaches often lack the appropriate quantification of cortical surface properties to perform a cortical shape-based analysis of surface area and cortical thickness measures. As a consequence, surface-based approaches, in which a cortical surface model is reconstructed from the volume images, are the standard in the field to quantify surface properties.

Earlier studies proposed a cortical surface model obtained along the gray matter and CSF boundary by deforming a topologically corrected model like a sphere [78, 80]. However, such reconstructed models generally suffered from poor representations of the narrow and deep buried cortical folding because it is exceedingly difficult to design an energy functional that fits the deformable model through the narrow opening of the sulci to the true cortical folding as pointed out in [30].

More recently, approaches have sought to finding the white and gray matter boundary to reconstruct a surface model, for example, FreeSurfer [17] or CIVET [79] pipelines. These frameworks are quite similar in terms of two properties: 1) their surface model guarantees a spherical topology for the white matter surface model construction. 2) the gray matter surface is obtained by deforming the white matter surface to fit the gray matter and CSF boundary, in which the cortical correspondence between the white and gray surfaces is inherently established. Briefly, the overall pipeline is summarized as follows. The raw MR images are first refined by bias field correction and intensity normalization. Then the preprocessed images are aligned in a common space such as Talairach space for skull stripping (including neck and eyeball) and cortical structure segmentation. The cortical tissues are segmented to create a white matter mask by filling in the subcortical structures within the white matter. This white matter mask is then separated into left and right hemispheres. Finally, the initial white matter surface is obtained via a rough triangulated tessellation in FreeSurfer or via deforming a topologically correct model in CIVET. Once the white cortical surface is obtained, the gray cortical surface is reconstructed by deforming the white cortical surface using volume intensity information with several geometric constraints (e.g., curvature smoothing).

Although the deep sulcal folding was better represented in cortical surface models, it has

been observed that the cortical surface reconstruction is also susceptible to partial volume effects with narrow sulcal fundi (e.g., less than 1 *mm*) often poorly represented due to low MR image resolution. In FreeSurfer, there are two types of topological defects as a result of such partial volume effects in the resulting model: holes and handles are present since it creates the surface model using a tessellation technique for the volume-wise tissue segmentation result. In contrast, such topological defects do not exist in CIVET because a topologically correct model is employed to fit to the white and gray boundary. However, this approach still suffers from partial volume effects in the white and gray boundary due to the design difficulty in energy functional. Therefore, the postprocessing is required either for topological correction to guarantee a desirable topology [32] or for appropriate representation of narrow cortical fundi by estimating partial volumes correctly [127].

## 2.2 Curvature Metrics

In differential geometry, given a point  $\mathbf{x}$  on the smooth surface with the tangent (walking) direction  $\mathbf{T}$ , the normal curvature at  $\mathbf{x}$  quantitatively measures the amount of the surface bend along  $\mathbf{T}$  as measured by the swing of the surface normal  $\mathbf{N}$  at  $\mathbf{x}$ . Let  $\Omega$  be a smooth surface  $\in \mathbb{R}^3$  with a sufficient parametrization:  $\mathbf{x}(u, v) \in \Omega$  such that  $\mathbf{x}_u$  and  $\mathbf{x}_v$  are linearly independent, where  $u, v \in \mathbb{R}$ . Let  $D_{\mathbf{T}}$  denote the directional derivative along  $\mathbf{T}$ . The normal swing at  $\mathbf{x}$  along  $\mathbf{T}$  is decomposed into two components: the normal curvature  $\kappa_{\mathbf{T}}$  and its geodesic torsion  $\tau_{\mathbf{T}}$ :

$$D_{\mathbf{T}}\mathbf{N} = \kappa_{\mathbf{T}} \cdot \mathbf{T} + \tau_{\mathbf{T}} \cdot \mathbf{T}^{\perp}, \quad (2.1)$$

where  $\mathbf{T}^\perp$  is the orthogonal direction to  $\mathbf{T}$  on the tangent plane, and

$$\mathbf{N} = \frac{\mathbf{x}_u \times \mathbf{x}_v}{\|\mathbf{x}_u \times \mathbf{x}_v\|}. \quad (2.2)$$

Similarly, the normal swing at  $\mathbf{x}$  along  $\mathbf{T}^\perp$  is given by the normal curvature  $\kappa_{\mathbf{T}^\perp}$  and its geodesic torsion  $\tau_{\mathbf{T}^\perp}$ :

$$D_{\mathbf{T}^\perp} \mathbf{N} = \kappa_{\mathbf{T}^\perp} \cdot \mathbf{T}^\perp + \tau_{\mathbf{T}^\perp} \cdot \mathbf{T}. \quad (2.3)$$

These properties are represented as a matrix form:

$$\begin{bmatrix} D_{\mathbf{T}} \mathbf{N} \\ D_{\mathbf{T}^\perp} \mathbf{N} \end{bmatrix} = \begin{bmatrix} \kappa_{\mathbf{T}} & \tau_{\mathbf{T}} \\ \tau_{\mathbf{T}^\perp} & \kappa_{\mathbf{T}^\perp} \end{bmatrix} \begin{bmatrix} \mathbf{T} \\ \mathbf{T}^\perp \end{bmatrix}. \quad (2.4)$$

Call the  $2 \times 2$  matrix  $M_{\mathbf{II}}$ . The geodesic torsion is the same regardless of the tangent direction  $\mathbf{T}$ , i.e.,  $\tau_{\mathbf{T}} = \tau_{\mathbf{T}^\perp}$ . The associated eigenvalues of  $M_{\mathbf{II}}$  are called principal curvatures that capture the pure normal swing along the eigenvectors with no geodesic torsion. To improve the ability of shape description, the principal curvatures ( $\kappa_1 \leq \kappa_2$ ) are further extended to the following geometric properties: mean curvature  $H$ , Gaussian curvature  $K$ , shape index  $S$  [51], and curvedness  $C$  [51].

$$\begin{aligned} H &= \frac{1}{2}(\kappa_1 + \kappa_2), \\ K &= \kappa_1 \cdot \kappa_2, \\ S &= -\frac{2}{\pi} \tan^{-1} \left( \frac{\kappa_1 + \kappa_2}{-\kappa_1 + \kappa_2} \right), \\ C &= \frac{2}{\pi} \log \left( \sqrt{\frac{(\kappa_1^2 + \kappa_2^2)}{2}} \right). \end{aligned} \quad (2.5)$$

Here is a brief description of those curvature metrics. The mean curvature  $H$  is the average of the principal curvatures; it equals the average normal curvatures over all directions. This quantification is an extrinsic measure and is equivalent to a half of the trace of  $M_{\text{II}}$ . The Gaussian curvature  $K$ ,  $\log(\det M_{\text{II}})$ , summarizes the swings of the normal per unit area; also, it is intrinsic in a sense of invariance to local isometries. Both  $H$  and  $K$  are invariant to the choice of bases and to rigid transformation, whereas these measures are not invariant to scaling. The shape index  $S$  and curvedness  $C$  were originally proposed to describe local shape in a more intuitive way. For example, Koenderink and van Doorn [51] argued that although spheres with different sizes intuitively have the same shape,  $H$  and  $K$  fail to describe such a property.  $S$  captures the local shape in a sense of convexity, hyperbolicity, and concavity, ranging from -1 (concave sphere) to the interval  $(-\frac{1}{2}, \frac{1}{2})$  (hyperbolic) to 1 (convex sphere).  $C$  measures how curved the surface is, ranging from  $-\infty$  (flat point) to  $\infty$  (singular point).

### 2.3 Spherical Harmonic Basis Functions

Spherical harmonics are a special form of eigenfunctions of the Laplace-Beltrami operator, as defined on the sphere. At a point  $(\theta, \phi)$  on the sphere defined over  $\theta \in [0, \pi] \times \phi \in [0, 2\pi)$ , the spherical harmonic basis functions with degree  $l$  and order  $m$  ( $-l \leq m \leq l$ ) are given by

$$Y_l^m(\theta, \phi) = \sqrt{\frac{2l+1}{4\pi} \frac{(l-m)!}{(l+m)!}} P_l^m(\cos \theta) e^{im\phi}, \quad (2.6)$$

$$Y_l^{-m}(\theta, \phi) = (-1)^m Y_l^{m*}(\theta, \phi), \quad (2.7)$$

where  $Y_l^{m*}$  denotes the complex conjugate of  $Y_l^m$  and  $P_l^m$  is the associated Legendre polynomial

$$P_l^m(x) = \frac{(-1)^m}{2^l l!} (1-x^2)^{\frac{m}{2}} \frac{d^{(l+m)}}{dx^{(l+m)}} (x^2-1)^l. \quad (2.8)$$

The spherical harmonic basis functions are orthonormal over the sphere. A real form of the functions can be obtained as defined by

$$Y_{l,m} = \begin{cases} \frac{1}{\sqrt{2}}(Y_l^m + (-1)^m Y_l^{-m}) & m > 0, \\ Y_l^0 & m = 0, \\ \frac{1}{\sqrt{2}i}(Y_l^{-m} - (-1)^m Y_l^m) & m < 0. \end{cases} \quad (2.9)$$

Any signals  $x(\theta, \phi)$  on the sphere can be decomposed into a linear combination of spherical harmonic basis functions.

$$x(\theta, \phi) = \sum_{l=0}^{\infty} \sum_{m=-l}^l c_l^m \cdot Y_l^m(\theta, \phi), \quad (2.10)$$

where  $c_l^m$  is a spherical harmonic coefficient of  $Y_l^m$ . Typically, the coefficients can be obtained by least squares fitting. The degree controls the reconstruction level of the original signal, as the high degree spherical harmonic basis functions handle high frequency components of the original signal interpolation. In practice, the degree is employed to determine smoothness of the original signal. Several applications are available using spherical harmonic decomposition such as shape analysis [119] and surface smoothing [13]. Moreover, in order to handle geometric properties of the cortical surface over the sphere via spherical harmonics, a mapping from the surface to the sphere is a must. This can be achieved in two ways: area-preserved [9] or conformal (angular preservation) mappings.

## 2.4 Entropy for Group-wise Surface Correspondence

Surface correspondence is a prerequisite for a surface-based population analysis. Depending on the objective, the correspondence can be optimized in several ways: landmark matching, predefined model fitting, and tight statistical distribution. In landmark matching, the shape correspondence is established via a geometric landmark-based metric minimization incorporating landmark agreement and regularization of the deformation. Another approach is fitting a predefined model to each individual surface, e.g., using SPHARM-PDM or skeletal representations (s-reps) [98]. The main idea is to roughly fit the target shape by minimizing momentum and further to refine the shape correspondence across a population. On the other hand, Kotcheff and Taylor [52] proposed surface correspondence based on tightening the probability distribution. The principle behind this approach is based on Occam’s razor that states “simple descriptions generalize best.” Thus, the corresponding objective function is the shape variability across a population, measuring tightness from the covariance matrix of derived PDMs. Later, a different objective function was proposed based on an MDL scheme as a tightness measure of the probability distribution [21, 133, 121, 19]. In information theory, MDL is a single scalar encoding for data compression, so it quantifies the amount of information that needs to encode the distribution for given a query value. For any distribution  $p$ , therefore, it is possible to construct a code  $c$  such that the length (in bits) of  $p$  at  $\mathbf{x}$  is given by

$$c(p(\mathbf{x})) = -\log_2 p(\mathbf{x}), \tag{2.11}$$

which minimizes the expected code length. In this framework, a shape correspondence is established by updating a current parametrization that minimizes MDL of the population

variability. More formally, the MDL for a population variability is equivalent to computing  $\sum \log \lambda$ , where  $\lambda$  are eigenvalues of the covariance matrix.

In the MDL framework both a proper shape parametrization and a update scheme are necessary at each optimization step. To avoid reparametrization every single step, Cates et al. [11] adapted entropy minimization akin to MDL to formulate particle-based registration on cortical surface models. In information theory, entropy describes the average of the information, i.e., the uncertainty removed when specifying the entity. For a given distribution  $p$ , its entropy is given by

$$H(p(\mathbf{x})) = E[c(p(\mathbf{x}))] = - \int_{-\infty}^{\infty} \int_{-\infty}^{\infty} \cdots \int_{-\infty}^{\infty} p(\mathbf{x}) \log_2 p(\mathbf{x}) d\mathbf{x}. \quad (2.12)$$

Under the Gaussian assumption of  $p$ , the entropy reduces to a simplified form:

$$\frac{1}{2} \log (\det (2\pi e \cdot \Sigma)) = \frac{N}{2} \left[ \{\log(2\pi) + 1\} + \frac{1}{N} \sum_{i=1}^N \log \lambda_i \right], \quad (2.13)$$

where  $\Sigma$  is a covariance matrix and  $\lambda$  are the eigenvalues of  $\Sigma$ . This implies that MDL is equivalent to entropy minimization under the Gaussian assumption as revealed in [52, 14]. In the entropy-based framework, pre-labeled particles are employed for shape correspondence establishment. The entropy encodes particle behaviors controlled in two different ways: for intra-subject similarity, the corresponding particles move over the surfaces to minimize entropy of their locations. In each subject, particles tends to move away from each atlas as far as possible to maximize entropy of their locations. Though they did not provide a weighting scheme, the particle-based shape correspondence needs to be leveraged by

introducing weighting factors as discussed in [131]. It can be easily observed that a particle-based shape correspondence implicitly defines a deformation model without guarantee of topological preservation. Also, particle-based methods were difficult to provide an explicit estimation of a deformation field between subjects.

## 2.5 Wavefront Propagation

A geodesic distance can be computed via formulating the wavefront propagation over the surface model. Given a medium  $\Omega$  and its boundary  $\partial\Omega$  (tangent space of the cortical surface with a speed at every point for example) in  $\mathbb{R}^2$ , the minimum travel-time from one (or multiple) source  $\in \partial\Omega$  to a point  $\mathbf{x} \in \Omega$  in the medium,  $u(\mathbf{x})$ , follows the propagation equation for some propagation speed function  $F$ :

$$\begin{aligned} \|\nabla u(\mathbf{x})\| F\left(\mathbf{x}, \frac{\nabla u(\mathbf{x})}{\|\nabla u(\mathbf{x})\|}\right) &= 1, \quad \mathbf{x} \in \Omega \subset \mathbb{R}^2, \\ u(\mathbf{x}) &= 0, \quad \mathbf{x} \in \partial\Omega. \end{aligned} \tag{2.14}$$

Such a formulation of the wavefront propagation is the so-called Hamilton-Jacobi partial differential equation (H-J PDE). A special case of the H-J PDE is as known as the Eikonal equation that solves the wavefront propagation with a constant speed function  $\alpha(\mathbf{x})$  in every direction. Like several applications (curvature-based speed [94], diffusion tensor [41]), now consider a special form of  $2 \times 2$  tensor matrix  $M(\mathbf{x})$  on the tangent plane such that

$$F\left(\mathbf{x}, \frac{\nabla u(\mathbf{x})}{\|\nabla u(\mathbf{x})\|}\right) = \frac{\nabla u(\mathbf{x})^T}{\|\nabla u(\mathbf{x})\|} M(\mathbf{x}) \frac{\nabla u(\mathbf{x})}{\|\nabla u(\mathbf{x})\|}. \tag{2.15}$$

If  $M$  is symmetric and positive,  $M$  is of an elliptic form along its eigenvectors. The wavefront propagation behaves according to the design of the tensor matrix  $M$ .

Although efficient Dijkstra-like solvers called fast marching [129, 112] are well developed for solving the Eikonal equation, the general H-J PDE cannot be directly solved using that solver because the characteristics of the PDE do not coincide with its gradients [113]. As pointed out in [41], therefore, PDEs with proper initial boundary conditions are classically solved by decomposing them into an independent system of ordinary differential equations by the method of characteristics [90]. However, this classic solution may not exist because the H-J PDE develops a discontinuity without smoothing constraints. Several alternative numerical approaches to a viscosity solution equipped with additional smoothing term are available as well. Single-pass approaches [113] solve the H-J PDE along the characteristic directions, whereas iterative approaches [45, 101] do in a number of pre-defined directions. In this dissertation, the ordered upwind method was employed with  $O(\gamma N \log N)$  complexity akin to Dijkstra's shortest path finding, where  $N$  is the number of discrete points over  $\Omega$  with an upper bound of its anisotropy coefficients  $\gamma$ , proposed by Sethian and Vladimirsky [113].

## CHAPTER 3: AUTOMATIC SULCAL CURVE EXTRACTION ON THE CORTICAL SURFACE

### 3.1 Overview

The recognition of sulcal regions on the cortical surface is an important task for shape analysis and landmark detection. However, it is a challenging task especially for the complex, folded human cortex. This chapter focuses on the extraction of sulcal curves from the human cortical surface. Current sulcal curve extraction methods are time-consuming in practice and often delineate curves incorrectly in the presence of significant noise.

This chapter presents a novel sulcal curve extraction method<sup>1</sup> on the cortical surface using the line simplification method originally proposed by Ramer [103] and by Douglas and Peucker [25]. The method approximates a polyline/polygon with a small number of the original points. It denoises a given curve by selecting a minimum sufficient number of the extremal points that are part of the original curve. The algorithm has been widely applied in the field of data compression, digital cartography, and denoising over range data from robotic sensors. In neuroimaging studies, sulcal fundic regions are known to have a higher stability than other cortical regions. Even though one can determine appropriate sulcal regions by applying a simple thresholding of the local curvature or sulcal depth information, those

---

<sup>1</sup>The work is based on the previously published paper: Lyu et al. [76]. This chapter partially adapts text descriptions and figures from the published paper.

approaches often suffer from the existence of noise over the sulcal regions. In my approach the sulcal curves are determined in a more robust way via the proposed line simplification method. In particular, the proposed method has several advantages over existing methods in terms of 1) no template model being required (or no prior information), 2) providing more robust sulcal curve extraction even at a high noise level, and 3) fast processing (high scalability).

The sulcal curve extraction method proposed in this chapter is briefly summarized as follows. First, a set candidate points is selected by thresholding the principal curvature map on the cortical surface. Since the line simplification has been originally defined for 2D curves, the surface is then cut to produce 2D contours at all candidate points with respect to the principal direction. The line simplification determines candidate sulcal points by denoising over the extracted contours. Finally, this reduced set of candidate points are connected in a piece-wise manner to obtain a set of complete sulcal curves. Section 3.2 states the objective of this chapter. Section 3.3 presents the transformation of the 3D cortical surface into several 2D slice contours to feed an input into the line simplification method. In Section 3.4, the candidate sulcal points are selected by the line simplification method. Finally, Section 3.5 presents piece-wise curve extraction from the selected sulcal points.

## 3.2 Objective

Given a triangulated mesh  $\Omega$  with a set of vertices  $V$ , the objective is to find a subset  $U \subseteq V$  that consists of sulcal points located at the deepest sulcal region so as to represent sulcal curves. The entire process consists of two main parts: sulcal point extraction and sulcal curve delineation.

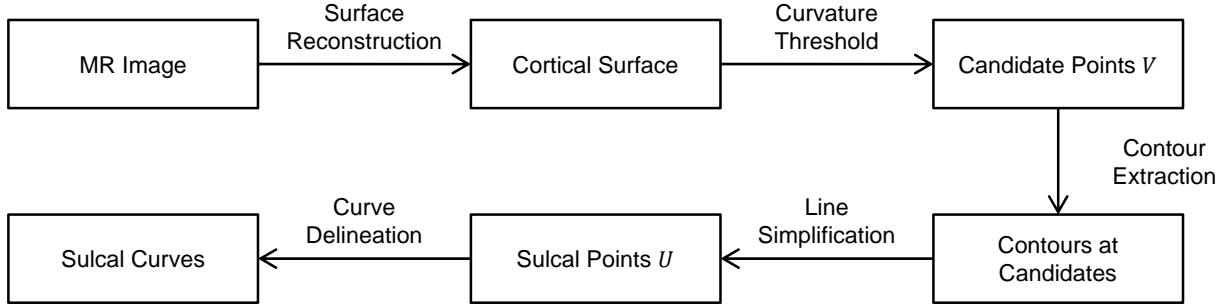


Figure 3.1: A schematic overview of the sulcal curve extraction. For each candidate sulcal point, a single contour is extracted. The line simplification is then employed to filter non-sulcal candidates.

In the sulcal point extraction a set of candidate points is first selected via a relatively generous thresholding of the maximum principal curvature at each location  $\in \Omega$ . Then, a cutting plane is computed such that it is orthogonal to the first principal direction at each point  $\mathbf{v} \in V$ , and the corresponding intersection is obtained between that plane and the surface. A point is added to  $U$  if it is preserved after the line simplification process. In the sulcal curve delineation, the selected points are connected using a geodesic kernel over  $\Omega$  with additional smoothing term. A schematic overview of the proposed method is illustrated in Figure 3.1.

### 3.3 Slicing and Contour Extraction

The line simplification method has been originally designed for 1D polylines. To extend the idea to a surface, a novel definition is necessary for most meaningful lines from the surface at every vertex/point. Here, the proposed method utilizes a planar intersection along a given direction. In particular, at a given point  $\mathbf{v} \in V \subset \Omega$ , the normal curvature with respect to a

given tangent direction  $\mathbf{T}$  is obtained by

$$k(\mathbf{T}) = D_{\mathbf{T}}\mathbf{N} \cdot \mathbf{T}, \quad (3.1)$$

where  $\mathbf{N}$  is the surface normal at  $\mathbf{v}$ . Since the objective is to check if  $\mathbf{v}$  is potentially identified as a sulcal point, a proper tangent direction  $\mathbf{T}$  needs to be determined to find a maximum curvature  $k$  in 2D space, in which the surface bends highly along its sulcal bank. The maximum curvature is defined here along the direction associated with the second principal curvature  $k_2 \geq k_1$ , where  $k_1$  is the first principal curvature (see also Section 2.2 for details). Thus, the first principal direction defines a plane for each vertex  $\mathbf{v} \in V$ . Let  $\mathbf{T}_{k_1}$  be the first principal direction associated with  $k_1$  at  $\mathbf{v}$ . Thus, the plane equation is given by

$$\mathbf{T}_{k_1} \cdot (\mathbf{x} - \mathbf{v}) = 0. \quad (3.2)$$

Assume that there are neither holes on the surface nor self-intersections. Thus, a cut between the plane and the surface yields a (or multiple) closed loop with no self-intersection. Here I propose a discrete version of [18] to produce a contour at any location of the surface. On the discrete surface model, a planar intersection test requires an exhaustive, computationally demanding test for every edge on the surface, where Equation 3.2 is satisfied. Thanks to an edge culling technique, this can be efficiently addressed by an incorporation of hierarchical axis-aligned bounding boxes (AABB). Finally, by sorting these intersections in counter-clockwise order with respect to the curve tangent  $(\mathbf{x} - \mathbf{v})$ , the ordered closed loop(s) is easily obtained for  $\forall \mathbf{v} \in \Omega$ . Figure 3.2 illustrates an example of contour extraction for both a

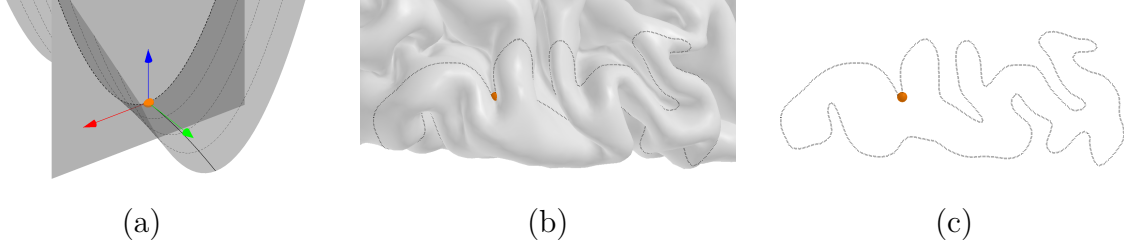


Figure 3.2: Contour extraction. (a) Schematic situation with dotted curves indicating several cutting planes. (a) The second (maximum curvature) principal directions is colored by *red*, respectively. (b) The cutting plane orthogonal to the second principal direction represents a sulcal point with the maximum surface bend. (c) An example contour on actual cortical surface (b) without the surface for better visualization.

synthetic and an actual cortical surface. The principal direction captures the maximum curvature as an optimal representation of the sulcal fundus in terms of its surface bend.

### 3.4 Sulcal Point Detection

Once the proposed contour is obtained at  $\mathbf{v} \in \Omega$ , my method applies the line simplification approach to the contour to select the minimum sufficient number of extremal points that represent the contour itself and to check if  $\mathbf{v}$  is filtered out after the line simplification method, as illustrated in Figure 3.3. Here is a brief summary of the line simplification method [103, 25]. For a given polyline, the two endpoints  $\mathbf{p}_0$  and  $\mathbf{p}_1$  are connected as a horizontal (base) line. Then, the extremal point  $\hat{\mathbf{p}}$  along the polyline with the maximum distance from the line is selected as follows:

$$\hat{\mathbf{p}} = \operatorname{argmax}_{\mathbf{p}} \|(\mathbf{p}_1 - \mathbf{p}_0) \times \mathbf{p}\| \cdot \|\mathbf{p}_1 - \mathbf{p}_0\|^{-1}. \quad (3.3)$$

The initial curve is split into two segments at the selected point  $\hat{\mathbf{p}}$  and the two endpoints. The method is then recursively applied to the two curve segments until the maximum distance is below a given threshold. Note that there can be various point selection strategies rather

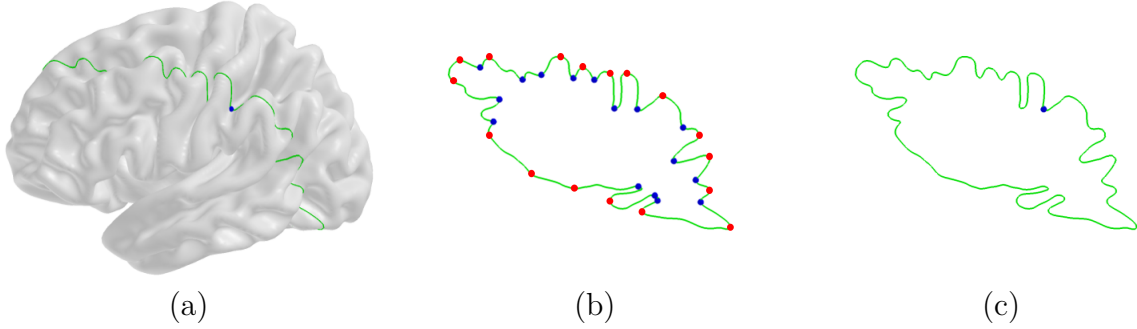


Figure 3.3: Sulcal point detection. (a) The contour that represents the maximum surface bend at a query point is obtained with respect to the principal direction. (b) In order to simplify the contour, the line simplification method selects a minimum sufficient number of the convex (*red*) and concave (*blue*) points that are part of the original contour. (c) The query point survives and is selected as a candidate point after the line simplification method.

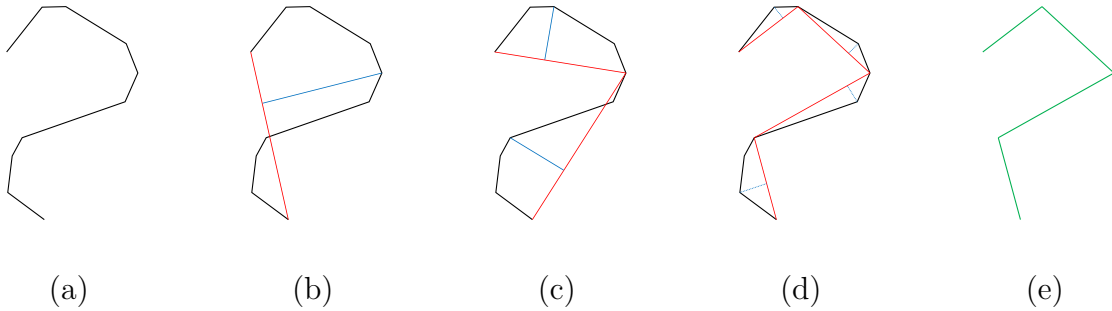


Figure 3.4: A schematic overview of the line simplification method. (a)-(b) Given a piece-wise curve, a horizontal line (*red*) is obtained by finding the two farthest points, and the extremal point is selected, having the farthest distance (*blue*) from the horizontal line. (c)-(d) The selected extremal point is then employed to connect a new horizontal line and the procedure is recursively applied until the distance from the horizontal line to a new extremal point is below a threshold. (e) The final simplified line is obtained by connecting all the detected extremal points.

than the maximum deviation [104], depending on the application. Figure 3.4 illustrates a schematic overview of the line simplification method.

In this problem setting, two endpoints are determined by finding the largest distance on the plane of  $\mathbf{T}_{k_2}$  among all possible pairs of points on the contour to split it into two longest possible curves by finding two extremal points as stated in [103, 25]. The line simplification

method is then applied to one of the two curves that contains the testing point  $\mathbf{v}$ . If  $\mathbf{v}$  is reported as a local maximum by the line simplification method,  $\mathbf{v}$  is collected into  $U$  as a sulcal point. Overall, the proposed method collects a set of candidate points whose number varies according to a user-defined threshold value. Figure 3.5 shows an example of candidate points chosen by the line simplification method. Since potential sulcal points lie along valley regions, they have a positive principal curvature. For expediting the process, the number of tests is further reduced by choosing a generous thresholding of curvatures. In the experiment, this threshold was empirically set to 0.01. Such thresholding is mainly for computational time reduction.

### 3.5 Curve Delineation

In order to connect the candidate points into complete curves, potential endpoints of (yet unknown) sulcal curves need to be estimated. For  $\forall \mathbf{u} \in U$ , thus, sulcal candidates points are collected within a geodesic distance  $r$  defined by an indicator function:

$$R(\mathbf{u}, \mathbf{v}) = \begin{cases} 1 & \text{if } L_{\mathbf{u}}(\mathbf{v}) \leq r, \\ 0 & \text{otherwise,} \end{cases} \quad (3.4)$$

where  $L_{\mathbf{u}}$  is a geodesic distance from  $\mathbf{u}$  to  $\mathbf{v} \in \Omega$ . The geodesic distance  $L_{\mathbf{u}}$  can be computed by the Eikonal equation (see Equation 2.14). Assign  $\mathbf{u}$  to a source of the wavefront propagation by letting the tensor matrix  $M(\mathbf{v}) = I$  for  $\forall \mathbf{v} \in \Omega$  in Equation 2.14, where  $I$  is the  $2 \times 2$  identity matrix. Thus, with a sufficient boundary condition  $L_{\mathbf{u}}(\mathbf{u}) = 0$ , the speed function in

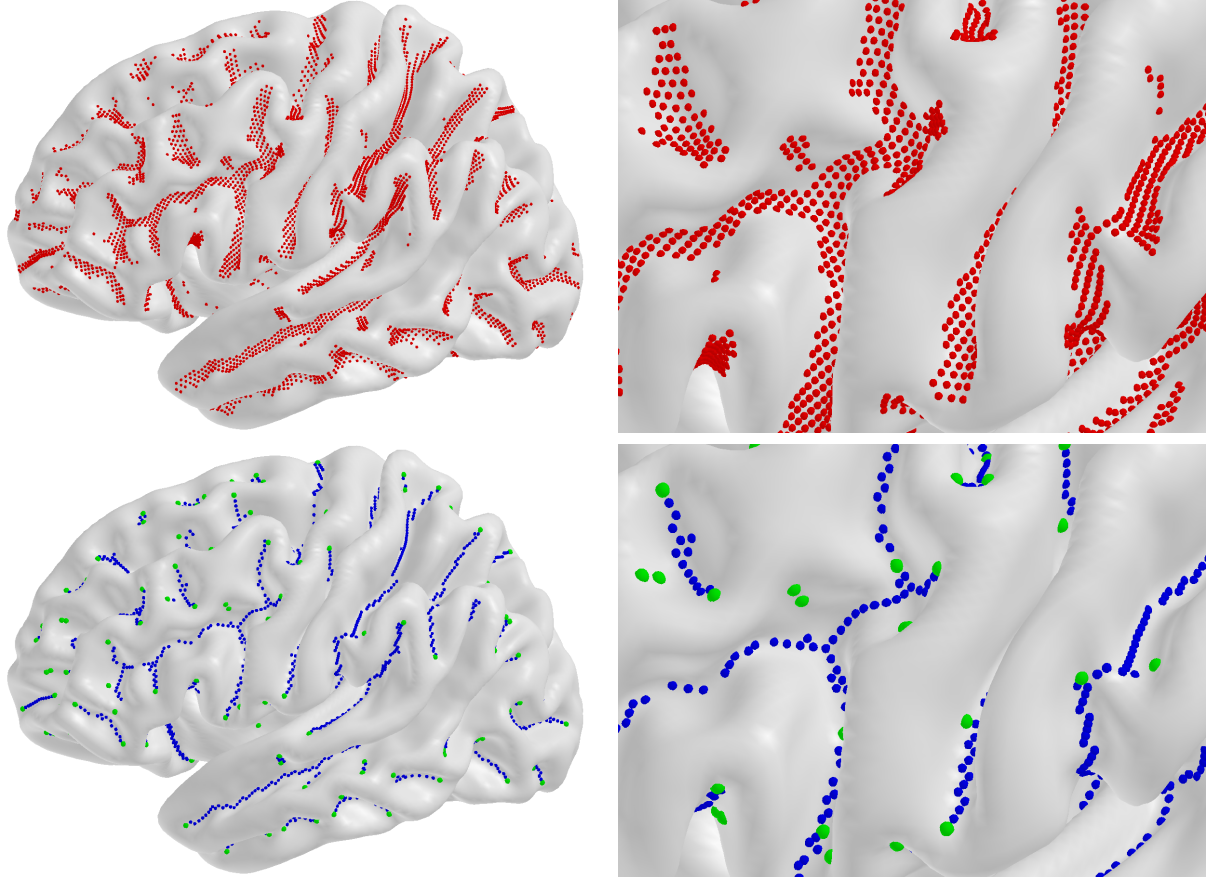


Figure 3.5: Maximum curvature points (*top*) and detected sulcal points (*bottom*, where sulcal endpoints are colored in *green* and *blue*). The vertices with positive curvatures are selected for candidate sulcal points. Since the candidate vertices are spread over a large portion of the sulcal fundic regions, they are further filtered out by the proposed method that eventually selects sulcal points (*blue*). The endpoints (*green*) are then selected from the selected sulcal points.

Equation 2.15 becomes

$$F\left(\mathbf{x}, \frac{\nabla L_{\mathbf{u}}(\mathbf{x})}{\|\nabla L_{\mathbf{u}}(\mathbf{x})\|}\right) = 1. \quad (3.5)$$

For  $M = I$ , this simplifies the H-J PDE to the Eikonal PDE:

$$\|\nabla L_{\mathbf{u}}(\mathbf{x})\| = 1. \quad (3.6)$$

The solution provides a geodesic distance  $L_{\mathbf{u}}$  for all locations of  $\Omega$ . The geodesic distance  $r$  in Equation 3.4 is chosen under the assumption that the sulcal regions are separated from each other by at least  $r$ . In this chapter, this quantity was empirically set  $r = 4.0 \text{ mm}$  based on the average width of the sulcal regions in the MNI-305 template [70]. This geodesic distance can be adjusted depending on the target population.

The candidate points are determined as endpoints if every point holding  $R(\mathbf{u}, \cdot) = 1$  is located within an octant centered at  $\mathbf{u}$  as shown in Figure 3.6. This is easily achieved by testing the sign of the inner products of all neighboring points holding  $R(\mathbf{u}, \cdot) = 1$ , i.e., no line between the neighboring points and the center point  $\mathbf{u}$  has a separating angle above 90 degrees. Let  $E \subseteq U$  be the set of the endpoints determined by this way. To find the neighboring sulcal point at  $\mathbf{u} \in E$ , the weighted shortest distance is employed from  $\mathbf{u}$  to  $\mathbf{s}$ , such that  $\mathbf{s}$  holds  $R(\mathbf{u}, \mathbf{s}) = 1$ . The distance weighting is based on the assumption that the tangent direction of the sulcal curve changes smoothly along the curve. Thus, the weighted distance is given by the following form:

$$C(\mathbf{s}, \mathbf{u}) = \|(\mathbf{s} - \mathbf{u}) \times \mathbf{T}(\mathbf{u})\|, \quad (3.7)$$

where  $\mathbf{T}(\mathbf{u})$  is the tangent vector at  $\mathbf{u}$ . Therefore, the neighboring sulcal point  $\hat{\mathbf{s}}$  at  $\mathbf{u}$  is obtained by

$$\hat{\mathbf{s}} = \underset{\mathbf{s}}{\operatorname{argmin}} C(\mathbf{s}, \mathbf{u}). \quad (3.8)$$

However,  $\mathbf{T}(\mathbf{u})$  is unknown due to no prior knowledge of the sulcal curve available. Instead  $\mathbf{T}(\mathbf{u})$  is estimated using the local principal direction,  $\mathbf{T}_{k_2}(\mathbf{u})$ . This is an incremental procedure; once  $\hat{\mathbf{s}}$  is determined, the same procedure is applied at  $\hat{\mathbf{s}}$  with its neighboring points holding

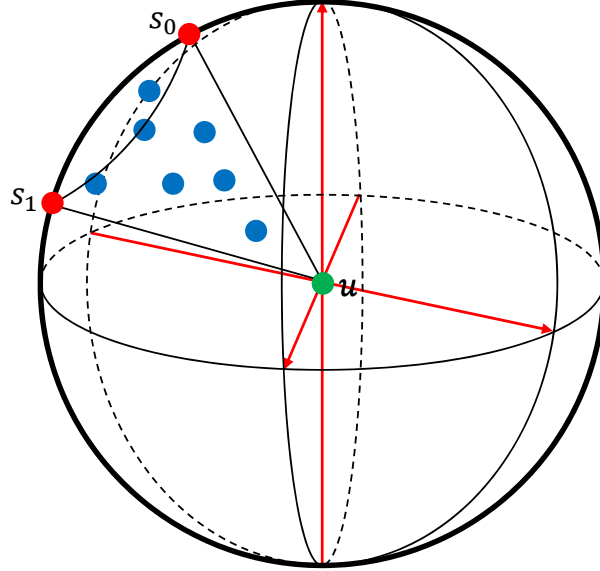


Figure 3.6: A schematic overview of the proposed endpoint detection. An example of the octant of the sphere is determined by three orthogonal axes.  $\mathbf{u}$  is determined as an endpoint if its neighboring points in a geodesic kernel  $S(\mathbf{u})$  belong to one of the octants.  $\overline{\mathbf{u}\mathbf{s}_0}$  and  $\overline{\mathbf{u}\mathbf{s}_1}$  form the maximum angle across every possible line starting from  $\mathbf{u}$ , such that  $R(\mathbf{u}, \mathbf{s}_0) = 1$  and  $R(\mathbf{u}, \mathbf{s}_1) = 1$ .

$R(\hat{\mathbf{s}}, \cdot) = 1$  and it stops if  $\hat{\mathbf{s}} \in E$  or  $\hat{\mathbf{s}}$  is a part of the other already delineated curve (junction point). Starting at an arbitrary endpoint, the curve estimation is finished if every element in  $E$  has been connected. Figure 3.7 shows the estimated curves from sulcal points. The sulcal endpoints are located in the end of each sulcal curve.

### 3.6 Materials

I chose the Kirby reproducibility dataset [53] to evaluate my sulcal extraction method for reproducibility. Briefly, the Kirby reproducibility dataset was acquired on 21 healthy volunteers with no history of neurological disease and is publicly available on NITRC<sup>2</sup>. Scan-

<sup>2</sup><http://www.nitrc.org/>, Neuroimaging Informatics Tools and Resources Clearinghouse

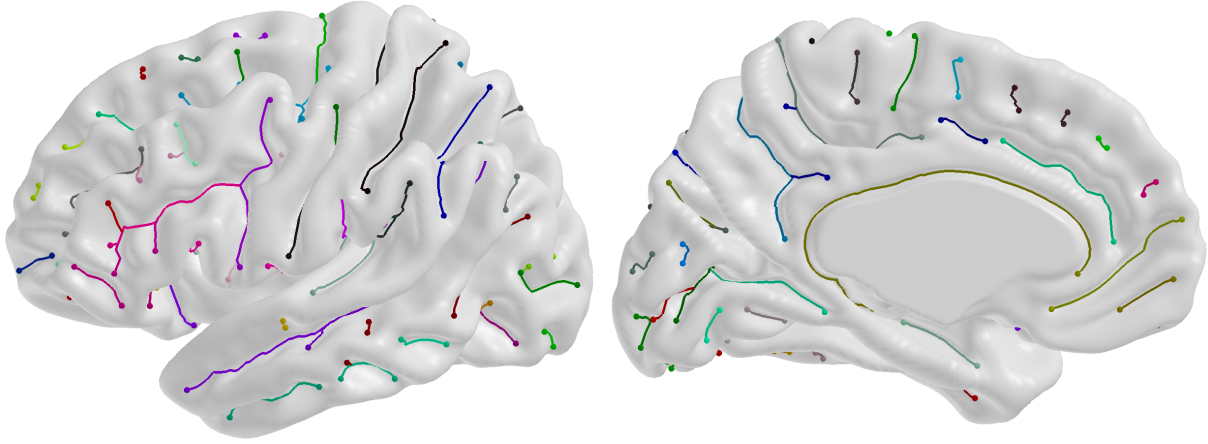


Figure 3.7: The estimated curves with endpoints in the lateral (*left*) and medial (*right*) views. The sulcal curves are reconstructed from the detected sulcal points. Each curve is labeled with a distinct color. End points are highlighted via larger dots. Sulcal regions with branches are represented as several curves with junction points.

rescan imaging sessions with  $T_1$ -weighted scans were acquired at the F.M. Kirby Research Center (Baltimore, MD, USA), using the MP-RAGE sequence on 3T Philips Achieva scanners at  $1.0\text{ mm} \times 1.0\text{ mm} \times 1.2\text{ mm}$  resolution (204 slices with  $\text{TR} = 6.7\text{ ms}$ ,  $\text{TE} = 3.1\text{ ms}$ , flip angle =  $8^\circ$ , matrix =  $240 \times 256$ ) scans. The central cortical surfaces were created using the standard Freesurfer v5.3 pipeline. For validation, the left hemispheres were resampled with 163,842 points via spherical icosahedron subdivision.

### 3.7 Results

All experiments were performed on a PC equipped with an Intel Core (TM) i5-3570K 3.4 GHz CPU with 12.00 GB memory, and only a single core was used. It took 1-2 minutes to obtain a full set of complete curves on a cortical surface on average. Quantitative verification on clinical data is extremely difficult as there is no ground truth for such sulcal curve data. Qualitatively I compared the results to standards in the field such as BrainVisa. The following

sections mainly focus on the reliability and reproducibility of the proposed method versus other methods.

### 3.7.1 Noise Sensitivity

To evaluate noise sensitivity, synthetic surfaces were generated by vertex-wise perturbation of an existing brain surface model. Perturbations were simulated via uniformly distributed independent displacements of the vertices. The left hemisphere of the MNI-305 average healthy control template surface was used for this evaluation purpose, also employed in [70], as the original brain surface model. Figure 3.8 shows the detected sulcal curves with different levels of perturbation. Visually, there is no significant difference from the original surface. For quantitative evaluation of the robustness to noise, for each sulcal point on the original surface, the Euclidean distance was measured to the closest point on the perturbed surface as no ground truth is available. Quantitatively, the experimental result showed that for each level of noise, the average distance was  $0.505 \pm 0.616$ ,  $0.776 \pm 0.629$ , and  $0.982 \pm 0.702$  *mm*, respectively. This indicates that the average distances are reasonable given the original MR image resolution (1.0 *mm*).

### 3.7.2 Reproducibility

From the KIRBY dataset, the BrainVISA pipeline<sup>3</sup> [107] was used to generate surfaces from the dataset with sulcal ribbon extraction, and the extracted sulcal ribbons then were projected onto the sulcal fundi to have sulcal curves for comparison. Figure 3.9 shows an example of

---

<sup>3</sup><http://brainvisa.info/>

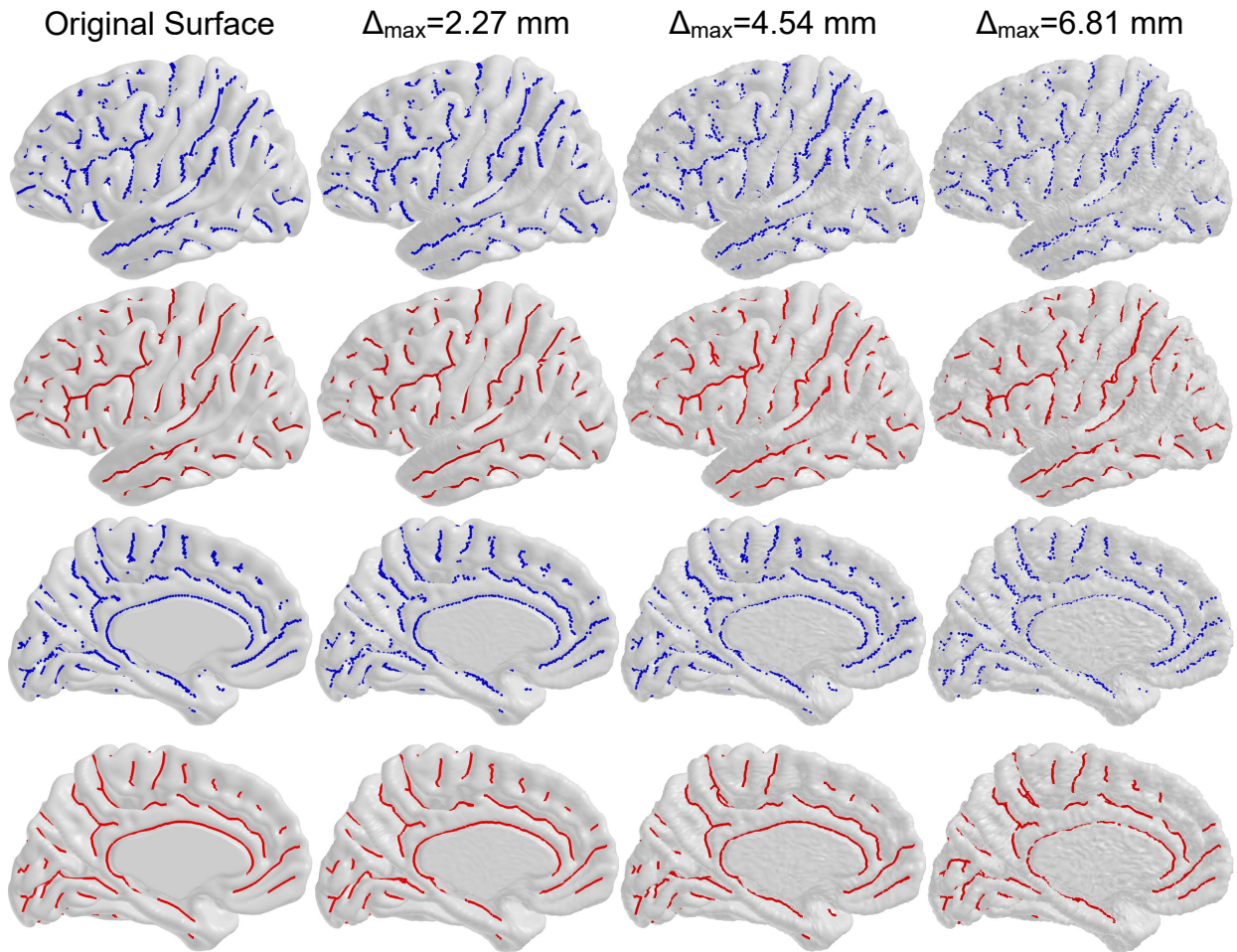


Figure 3.8: Robustness to noise. Sulcal points are detected on the surface perturbed by a random noise.  $\Delta_{\max}$  indicates the maximum displacement of the vertex. The detected sulcal points (*blue*) and the estimated curves (*red*) are stable across levels of noise. The quantitative evaluation also shows that the average distance to the corresponding points is less than 1.0 *mm*.

the sulcal curves extracted by using the proposed method. Again, the closest distances were measured at sulcal points between two corresponding surfaces and then averaged along each sulcus. Since the closest distance computation is asymmetric (one-way), it took the maximum of the two possible distances from both corresponding surfaces. Figure 3.10 illustrates a statistics on the maximum average distances of the corresponding surfaces. Importantly, the sulcal extraction in the BrainVISA pipeline generates only the set of the labeled major

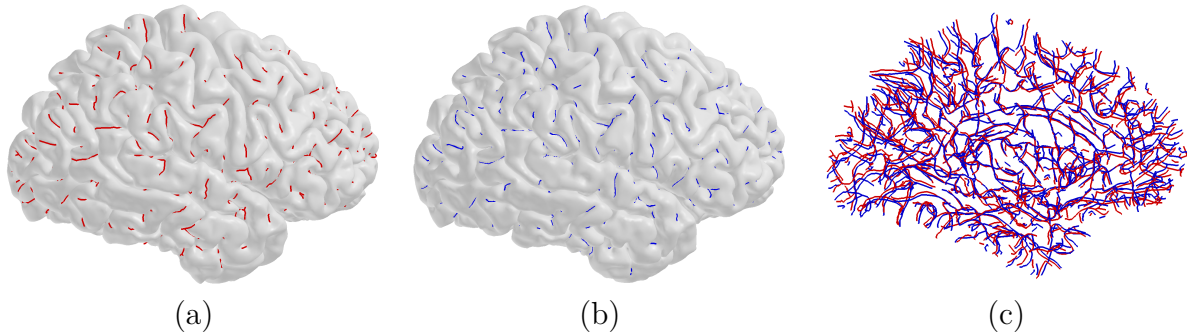


Figure 3.9: Sulcal curve extraction from the different scans for the same subject. (a)-(b) Two sets of curves are labeled with respective colors (*red* and *blue*). (c) The two sets are well aligned in the same space.

curves as its output (unlabeled curves provided in this pipeline). On the other hand, the proposed method extracted both major and minor curves (major curve labeling is out of scope in this chapter). Thus, it could be a unfair evaluation for the proposed method without a major curve labeling procedure as one would expect higher reproducibility errors in those smaller curves. Despite that disadvantage, the experimental results show that the proposed method has less average distance than BrainVISA. The proposed method achieved  $2.01 \pm 0.33$  mm (average  $\pm$  standard deviation across all 21 cases), whereas BrainVISA showed an average distance of  $2.89 \pm 0.73$  mm. To obtain statistical significance, I applied a paired  $t$ -test between the maximum average distances obtained from BrainVISA and the proposed method (total 21 maximum average distances for each method as shown in Figure 3.10). This reveals that the proposed method achieves a statistically significant smaller average distance ( $p \ll 0.0001$ ).

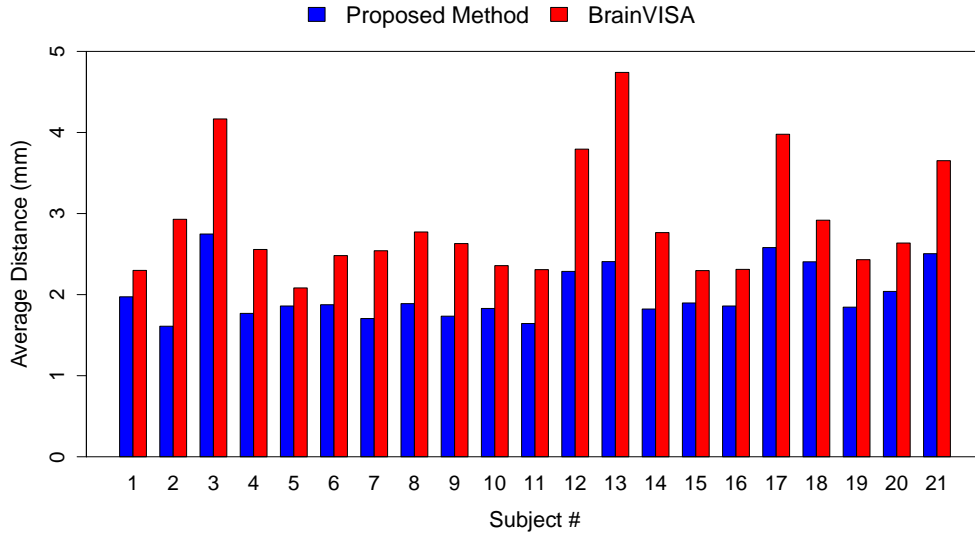


Figure 3.10: The maximum average distances of the extracted sulcal curves on the 21 subjects in the Kirby reproducibility dataset. The proposed method achieves consistent results over those obtained in the BrainVISA pipeline.

### 3.8 Summary

This chapter presented a fast and accurate automatic sulcal curve extraction method to provide cortical geometric landmarks based on the observation that sulcal fundic regions are well defined as local extrema. A set of candidate sulcal points is chosen by the line simplification method. The extracted sulcal points are further connected to form a set of sulcal curves on the cortex. The resulting landmarks showed a high reliability in the multi-scan dataset as well as robustness to a high level of noise.

The experimental results showed that the proposed method captures sulcal curves robustly in the presence of noise and shows high computational efficiency. In comparison to BrainVISA, a standard neuroimaging tool, the proposed method showed significantly improved reproducibility. The proposed method has several advantages: First, the parameter tuning is quite simple as there is a small set of parameters and the results are robust to reasonable

changes in the parameters. Second, no preprocessing is required on the cortical surface.

## CHAPTER 4: ROBUST ESTIMATION OF SURFACE CORRESPONDENCE

### 4.1 Overview

Establishing surface correspondence is a critical step for a population analysis of surface properties. While template-based cortical surface correspondence is standard in the field, it is known to introduce a bias to the template selection for the statistical analysis. This chapter presents my novel approach to establish cortical shape correspondence via a group-wise cortical correspondence method using a spherical harmonic decomposition of a smooth deformation field matching sulcal landmarks and sulcal depth maps. Since the pair-wise correspondence potentially has a template selection bias, I expect group-wise correspondence to establish a better correspondence for the purpose of population analysis such as a cortical thickness analysis.

I propose here a group-wise approach<sup>1</sup> with the following contributions: (a) robust entropy estimation to reduce the influence of landmark extraction and labeling errors, (b) the accelerated computation by employing orthonormality of the harmonic basis functions, (c) a novel surface coloring for visual comparison, (d) experiments with respect to robustness and comparisons with existing methods. The overall framework of the proposed group-wise

---

<sup>1</sup>The work is based on the previously published papers: Lyu et al. [73, 74, 75]. This chapter partially adapts text descriptions and figures from the published papers.

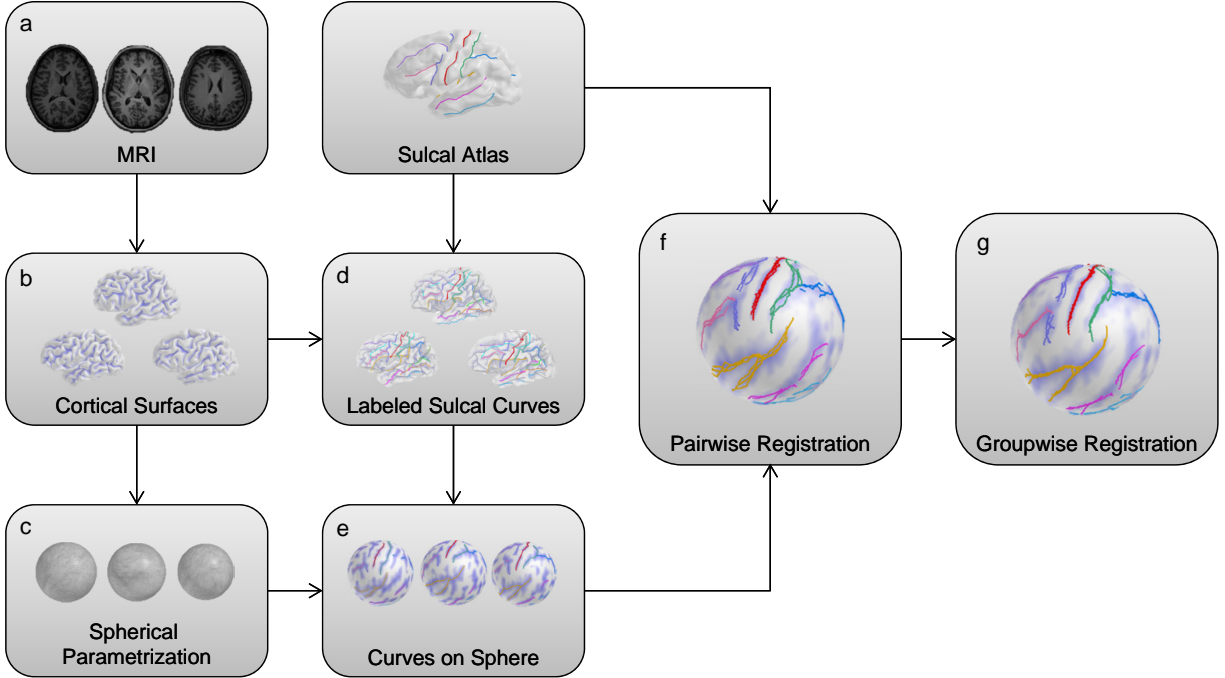


Figure 4.1: A schematic overview of the pair-wise method. From the cortical surface, sulcal/gyral curves are extracted and their correspondence is established by the proposed evolutionary algorithm. The complete gyrification index map is obtained via a Gaussian propagation.

correspondence method is summarized as follows. 1) Cortical surfaces are reconstructed from MRIs with spherical parametrization. 2) Sulcal curves are automatically extracted with their labels and mapped onto the sphere. 3) Pair-wise registration is performed on the mapped sphere (common space) to establish an individual correspondence to a prior template. 4) Group-wise registration is applied initialized by the pair-wise correspondence for unbiased estimation regardless of the template choice. Figure 4.1 illustrates a schematic overview of the proposed method.

As preprocessing, Section 4.2 demonstrates the previous methods of sulcal curve extraction and their labeling as well as the rigid alignment of landmarks. In Section 4.3, the labeled sulcal curves are employed for shape correspondence establishment in a pair-wise manner.

Section 4.4 describes the group-wise shape correspondence to remove the template-selection bias. Finally, Section 4.5 presents the shape correspondence evaluation methods.

## 4.2 Preprocessing

This section describes preprocessing of the input surface models including sulcal landmark extraction/labeling and rigid alignment using landmarks.

### 4.2.1 Automatic Sulcal Curve Labeling and Landmark Correspondence

Two methods are employed as preprocessing of the proposed framework: my automatic sulcal curve extraction described in Chapter 3 and the automatic sulcal curve labeling [71] proposed during my earlier work. First, the unlabeled sulcal curves consisting of ordered sets of points without branching are extracted from the triangulated surface by my sulcal curve extraction method. While no branching is taken into account, each sulcal curve can be (and is often) composed of multiple separated curve segments. Then, pre-labeled sulcal curves (according to the protocol in [73] for the macaque subjects and [71] for the human subjects) are employed to label corresponding unlabeled sulcal curves while discarding minor and extraneous curves. This labeling method further establishes a point-by-point correspondence on these sulcal curves called sulcal landmarks that are employed in the proposed sulcal correspondence methods.

Here is a brief description of my sulcal curve labeling procedure. Given a set of input (unlabeled) sulcal curves automatically extracted from a cortical surface (input) and a collection of prelabeled major sulcal curves (template), the objective is to identify the input major sulcal curves while establishing point-wise correspondence with template curves. Given

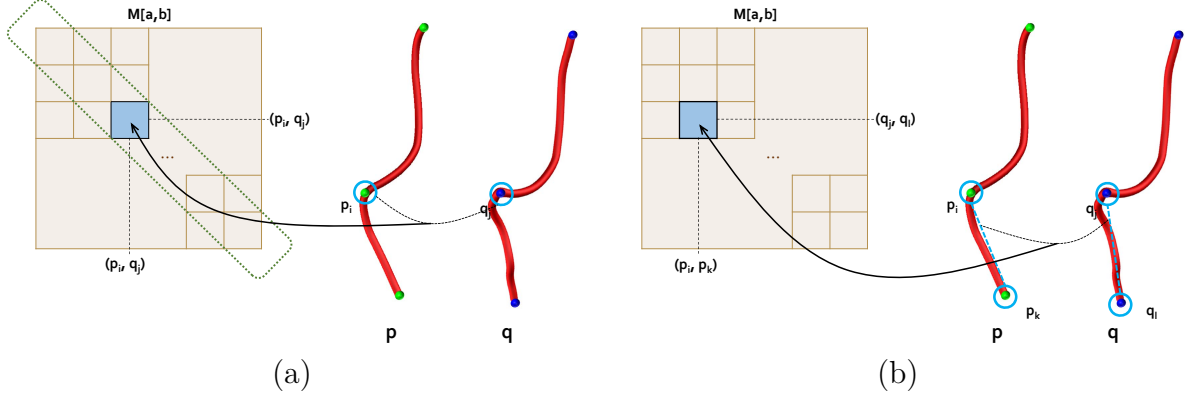


Figure 4.2: A schematic overview of the spectral matching. The spectral matching establishes a point-wise correspondence by taking into account both individual point similarity (a) and relative relation similarity (b). Given two curves,  $p$  and  $q$ , the individual similarity is measured between  $p_i$  and  $q_j$  (left), and the relative relation similarity is measured between  $(p_i, p_k)$  and  $(q_j, q_l)$  (right). The affinity matrix  $M$  encodes those similarities, and its corresponding eigenvalue guides the point-wise correspondence between curves.

a raw input sulcal curve set, the most similar template curves are chosen to label the raw curves, based on the point-wise curve correspondence. To establish curve correspondence, the spectral matching algorithm [60] is employed to choose the best matched curve by exploiting the sulcal curve features and their relationship. Figure 4.2 shows an example of the spectral matching using point-wise correspondence.

#### 4.2.2 Rigid Transformation for Initial Alignment on Sphere

Given a set of point landmarks (sulcal curves for example), the landmark geodesic distance errors over the unit sphere are employed for rigid alignment. Thus, the objective here is to find proper spherical rotations that minimize the sum of landmark geodesic distance errors. Specifically, there are two rotations used in this alignment. First, for each subject the mean spherical position of its landmarks is obtained via computing the Fréchet mean. Let  $\mathbf{M}_i$  be the mean landmark position of subject  $i$ . All subjects are aligned to an arbitrarily

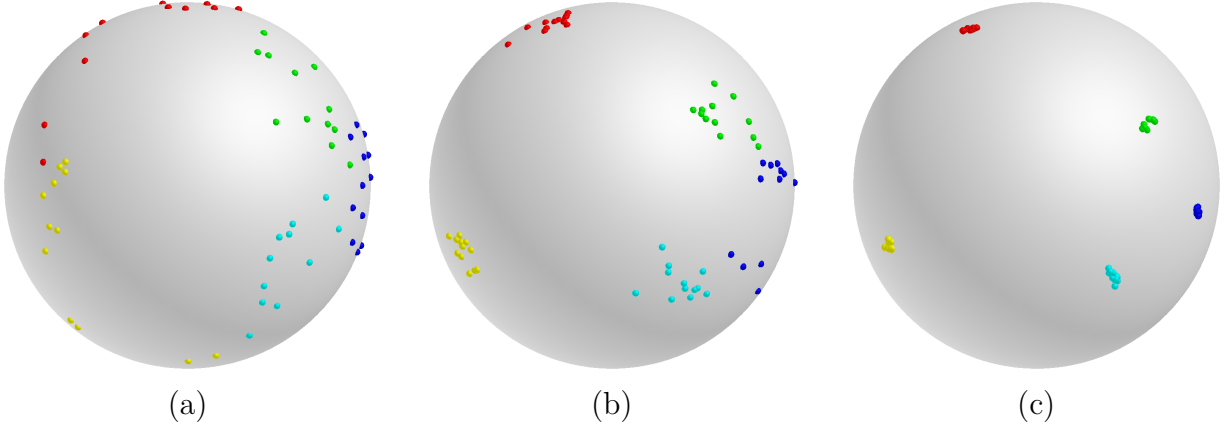


Figure 4.3: Landmark distribution of 12 primate molar shapes on the sphere with 5 manually annotated landmarks. Each color indicates the corresponding landmark. (a) initial parametrization determined via SPHARM-PDM, (b) aligned landmarks after rigid transformation on the sphere, and (c) final landmark alignment via the proposed group-wise method.

selected subject  $j$  by simply rotating  $\mathbf{M}_i$  to  $\mathbf{M}_j$ . Let  $\mathbf{M}'_i$  denote the rotated position of  $\mathbf{M}_i$ . Second, once  $\mathbf{M}'_i$  are obtained, another rotation with respect to  $\mathbf{M}'_i$  is computed by minimizing the sum of landmark geodesic errors over the sphere, which needs to be optimized. The optimization uses the NEWUOA optimizer [99] for finding two rotational angles. In Figure 4.3, for example, 5 manually annotated landmarks are roughly aligned after rigid transformation of primate molar shapes. Such a rigid transformation is used for initialization of the proposed group-wise method.

### 4.3 Landmark-based Pair-wise Surface Correspondence

#### 4.3.1 Objective

For two given triangulated cortical surfaces (template and subject), denote the template and subject surfaces by  $V_{\text{temp}}$  and  $V_{\text{subj}}$ , respectively. The objective is to estimate a continuous

cortical correspondence  $M : \mathbb{R}^3 \rightarrow \mathbb{R}^3$  such that

$$u = M(v) , \tag{4.1}$$

where locations  $v$  on the subject surface  $V_{\text{subj}}$  are mapped to the corresponding locations  $u$  on the template surface  $V_{\text{temp}}$ .

### 4.3.2 Consistent Displacement Encoding Scheme

To take advantage of the well known spherical parametrization, an invertible spherical mapping  $\psi(\cdot) : \mathbb{R}^3 \rightarrow \mathbb{S}^2$  is established in the preprocessing stage. All vertices of the cortical surfaces are then mapped onto the common unit sphere. This reduces the correspondence estimation to finding  $M : \mathbb{S}^2 \rightarrow \mathbb{S}^2$ . This spherical mapping establishes an initial cortical correspondence that is further improved first by this pair-wise method followed by the group-wise method.

In this correspondence framework, a novel encoding scheme is necessary for the deformation representation as a displacement in local spherical polar angles of elevation  $\Delta\theta$  and azimuth  $\Delta\phi$ . It is well-known that the local spherical angles at different locations on the sphere based on a single frame of reference (spherical coordinate system) yield inconsistent representations of the same arclength. For example, a given displacement  $(\Delta\theta, \Delta\phi)$  at the equator yields a longer geodesic arclength than the same displacement closer to the pole. To address this issue, I employ a locally normalized polar system to provide an arclength consistent encoding.

Let  $p$  and  $q$  be corresponding landmarks from a subject and the template, respectively. First, a rotation matrix  $\mathbf{R}_p$  is defined with an angle ( $\leq 90^\circ$ ) along the longitude circle passing

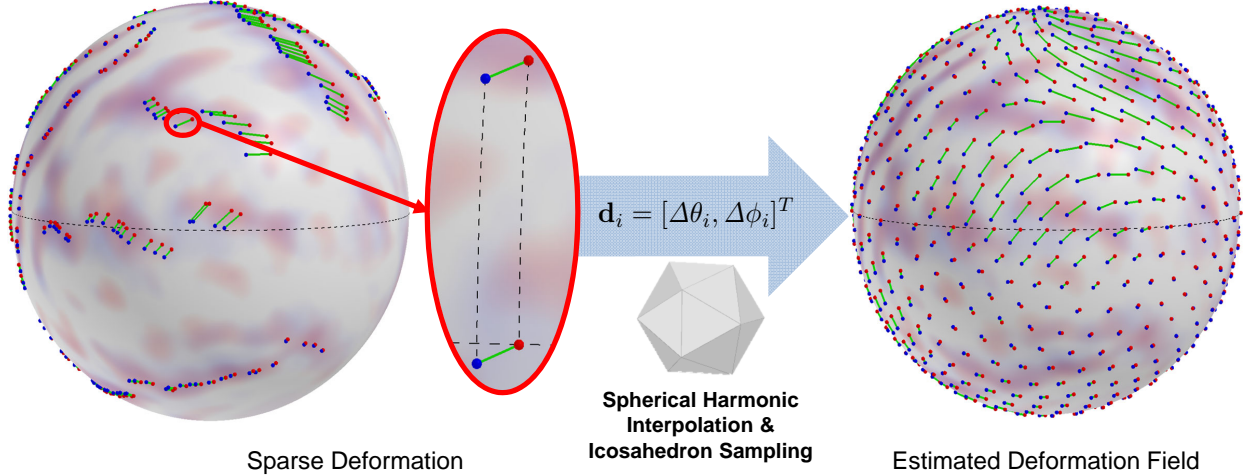


Figure 4.4: Displacement encoding and estimated deformation field (an icosahedron sampling of continuous representation). A spherical displacement is encoded as change in spherical angles after rotation onto the equator for arclength preservation, which avoids distorted displacement representation. The interpolation of the deformation field is obtained by spherical harmonic decomposition.

through  $p$  and the two poles, such that  $p$  is exactly located on the equator. By applying  $\mathbf{R}_p$  to  $p$  and  $q$ , it can yield the normalized local polar displacement vector  $\Delta\theta$  and  $\Delta\phi$ . Thus, the local landmark displacement at spherical vertex  $i$  ( $\theta_i, \phi_i$ ) on the unit sphere is represented as a vector  $\mathbf{d}_i = \psi(\mathbf{R}_{p_i} \cdot p_i) - \psi(\mathbf{R}_{p_i} \cdot q_i) = [\Delta\theta_i, \Delta\phi_i]^T$  (see Figure 4.4).

### 4.3.3 Initial Deformation Field

To find an initial deformation field over the entire surface, a least squares fitting of spherical harmonic basis functions is applied to displacements of the sulcal landmarks established in the sulcal labeling step [71]. This fitting employs standard spherical harmonic decomposition of the  $[\Delta\theta_i, \Delta\phi_i]$  spherical signal. At a point  $(\theta, \phi)$  on the sphere, the spherical harmonic basis functions with degree  $l$  and order  $m$  ( $-l \leq m \leq l$ ) are described in Equation 2.9. Given the degree  $l$  of spherical harmonic decomposition, assume that the number  $n$  of the landmarks is larger than the dimension of  $(l + 1)^2$  spherical harmonic basis functions to

prevent a rank-deficient problem. The coefficients can then be estimated by standard least squares fitting.

$$\mathbf{C} = (\mathbf{Y}\mathbf{Y}^T)^{-1} \mathbf{Y}\mathbf{D}^T, \quad (4.2)$$

where  $\mathbf{D} = [\mathbf{d}_1, \mathbf{d}_2, \dots, \mathbf{d}_n]$  and  $\mathbf{Y}$  is a  $(l + 1)^2$  by  $n$  matrix that incorporates the spherical harmonic bases. Once the coefficients of the spherical harmonic decomposition are computed, for a point  $v \in V_{\text{subj}}$  subject space, its deformed position in the template space is easily reconstructed by the spherical mapping function  $\hat{M}$ .

$$\hat{u} = \hat{M}(v) = \mathbf{R}_v^T \cdot \psi^{-1}(\psi(\mathbf{R}_v \cdot v) + \mathbf{C}^T \cdot \mathbf{Y}_v), \quad (4.3)$$

where  $\mathbf{Y}_v$  is a column vector of the spherical harmonic basis at  $\psi(v)$  and  $\mathbf{R}_v$  is a rotation matrix defined above that puts  $v$  on the equator. Figure 4.4 shows an example of the estimated deformation field.

The basis functions are linearly independent due to their orthogonality property. Thus, the initial deformation field is computed via a low degree ( $l = 5$ ) fit of the sulcal landmarks, while a higher degree representation is used in the optimization stage via an incremental scheme.

#### 4.3.4 Optimization

As discussed in the earlier section, the initial coefficients are determined only by the sulcal landmarks. This choice biases the cortical correspondence to the specific sulcal fundic regions affected by mislabeling errors in the sulcal labeling step. For improved correspondence establishment, a geometric metric is formulated by incorporating sulcal landmark errors

and agreements between sulcal depth maps via normalized cross-correlation (NCC) over the entire cortical surface. To regularize the impact of landmark errors, an M-estimator is employed based on a weighting function  $f$  under a Gaussian assumption in Equation 4.4. By incorporating  $d_{\min}$  as voxel size, landmark errors are ignored if below  $d_{\min}$  distance and reduced to a maximal contribution if over a maximum distance  $d_{\max}$ .  $d_{\max}$  was set about 10–20 times larger than  $d_{\min}$  based on experimental observations.

$$f(d) = 2 \int_{d_{\min}}^d \frac{I(d)}{\sigma\sqrt{2\pi}} \exp\left\{-\frac{1}{2}\left(\frac{x-d_{\min}}{\sigma}\right)^2\right\} dx, \quad (4.4)$$

$$I(d) = \begin{cases} 1 & d \geq d_{\min}, \\ 0 & \text{otherwise,} \end{cases} \quad (4.5)$$

where  $6 \cdot \sigma = d_{\max} - d_{\min}$ . Now, let  $L(\cdot, \cdot) = f(\eta \cdot \text{arclen}(\cdot, \cdot))$  be a regularized arclength, where  $\eta$  is a ratio of the geodesic distance between two points mapped on the unit sphere and on the template surface. Practically,  $\eta$  can be approximated as a ratio of the triangle size under the assumption that the template surface consists of uniform triangles. The resulting overall cost function is thus formulated with a regularization factor  $w$  by letting an operator  $\otimes$  denote normalized cross correlation between two sulcal depth maps.

$$\hat{\mathbf{C}} = \underset{\mathbf{C}}{\operatorname{argmin}} \left[ w \left\{ \frac{1}{n} \sum_{i=1}^n L(p_i, \hat{p}_i) \right\} + (1-w) \left\{ \frac{1}{2} (1 - S(\{u\}) \otimes S(\{\hat{u}\})) \right\} \right], \quad (4.6)$$

where  $p_i$  and  $\hat{p}_i$  are two corresponding sulcal points and  $S(\cdot)$  is a sulcal depth map (or any other property map such as a local curvature map) reconstructed from a set of vertices. The optimization procedure employs the NEWUOA optimizer [99] for minimizing  $\hat{\mathbf{C}}$ . The

optimizer finds an optimal solution without derivatives. In the experiment,  $w$  is empirically set to 0.5 based on the experimental results in [73].

### 4.3.5 Optimal Pole Selection

The direction of displacements varies with location in the proposed spherical polar coordinate system as shown in Figure 4.5. Depending on the location of the equator, two identical displacements have a different sign in polar angles if they are computed on opposite sites with respect to the poles. This can yield a deformation field with significant distortions leading to even sign changes close to the poles. Therefore, a proper choice of the pole  $\hat{\mathbf{e}}$  can significantly minimize this influence and yield mostly smooth deformation fields. In my experience, the presence of non-smooth deformations generally leads to high magnitude coefficients in high frequency bases. Thus, a coefficient-sum-based metric could be a reasonable choice as it weights higher frequency coefficients more strongly.

$$\hat{\mathbf{e}} = \underset{\mathbf{e}}{\operatorname{argmin}} \sum_{l=0}^k \sum_{m=-l}^l (l+1) \cdot \{|c_{\theta_{l,m}}| + |c_{\phi_{l,m}}|\} , \quad (4.7)$$

where  $c_{\theta}$  and  $c_{\phi}$  are coefficients for elevation and azimuth displacements, respectively. As this metric possibly has local minima, the optimization is initialized with multiple initial guesses spread across the sphere, and then the minimum is selected as the optimal pole. Figure 4.5 shows an example of artifacts in the standard polar coordinate system, which are significantly reduced after the optimal pole selection.

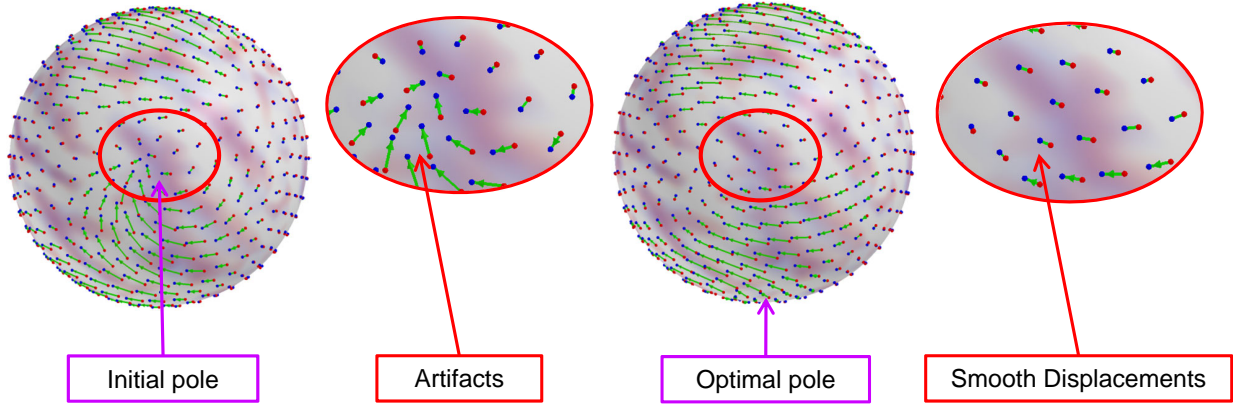


Figure 4.5: Artifacts in the standard polar coordinate system and reduced artifacts (smooth deformation field) by the optimal pole selection. The artifacts introduced by spherical harmonic interpolation are significantly reduced by choosing a proper pole.

#### 4.4 Extension to Group-wise Surface Correspondence

This section demonstrates a group-wise registration to further improve pair-wise registration results as well as to remove the template selection bias inherent to pair-wise registration as described in [73]. A group-wise correspondence is computed independently from any template and thus is expected to perform more stably across a population of surfaces. The group-wise correspondence method incorporates modified entropy terms computed over the landmark distributions and feature maps such as sulcal depth. Figure 4.6 shows a schematic overview of the group-wise registration.

##### 4.4.1 Objective

For  $N$  given triangulated cortical surfaces mapped onto the unit sphere, each of which has the same number  $n$  of the common corresponding vertices, let  $V^i$  be the  $i$ th surface,  $i = 1, \dots, N$ . The goal is to estimate continuous mapping functions of cortical correspondence

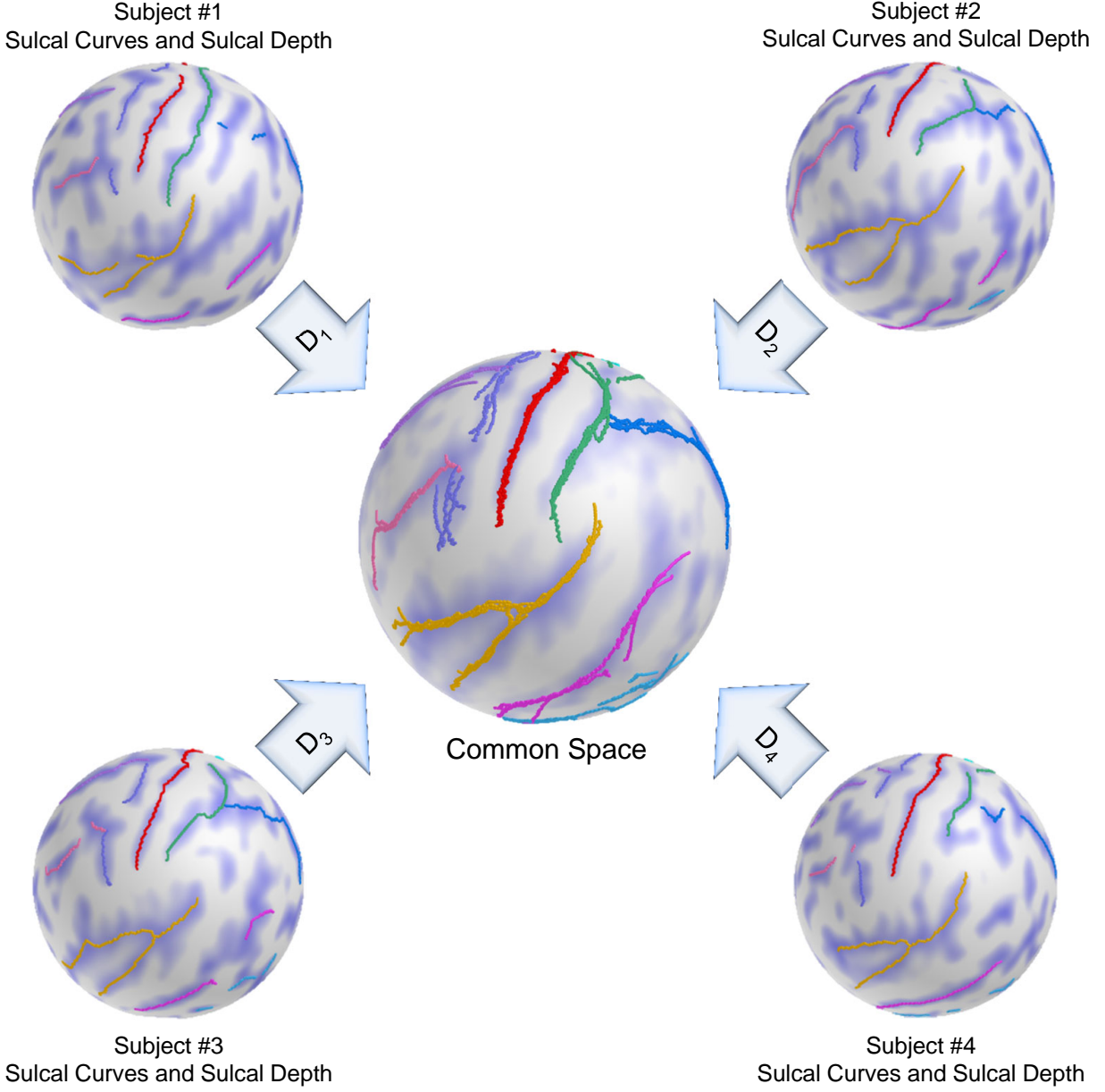


Figure 4.6: A schematic overview of the group-wise registration. An initial correspondence for each subject is established by the pair-wise correspondence. The deformed sulcal curves and depth maps are mapped onto the sphere based on the pair-wise correspondence. The group-wise correspondence is then iteratively updated across a population via entropy minimization.

$M_i : \mathbb{R}^2 \rightarrow \mathbb{R}^2$  that map surfaces into a common reference space such that

$$M_1(v^1) = M_2(v^2) = \dots = M_N(v^N) , \quad (4.8)$$

where  $v^i$  are the corresponding locations on the subject surface.

Let  $\mathbf{x}(M_j)$  be a column vector of the corresponding points of subject  $j$  deformed by  $M_j$ , i.e.,  $\mathbf{x}(M_j) = [M_j(v_1^j), \dots, M_j(v_n^j)]^T$ . As described in [11], assume that  $\mathbf{x}(M_j)$  are instances of  $\mathbf{X}$  drawn from a probability density function  $p(\mathbf{X})$ . The average amount of the information in the random sampling is given by the entropy  $H[\mathbf{X}]$ , and the minimization problem is then formulated as follows.

$$\{\hat{M}_1, \dots, \hat{M}_N\} = \underset{\{M_1, \dots, M_N\}}{\operatorname{argmin}} H[\mathbf{x}], \quad (4.9)$$

which drives mapped/deformed corresponding points closer to each other.

#### 4.4.2 Entropy of Landmark Errors

In the previous section, I described my pair-wise correspondence that is employed as initialization for my group-wise method. As the sulcal labeling procedure yields varying parts of sulcal curves being labeled across different cortical surfaces, the set of sulcal landmarks is selected to consist of only those that have a full correspondence set across all cortical surfaces. Now, a key step for landmark entropy computation is the density estimation of corresponding landmarks. However, appropriate density estimation on the sphere can be computationally demanding, as it involves geodesic distance computation. Here I propose two different methods for landmark mean estimation as well as weighting for the landmark error handling.

**Euclidean Mean as Landmark Mean Estimator** Similar to [11] for reasons of efficiency, assume that the initial mapping well centralizes corresponding landmarks, which allows a

mapping from the spherical space to the Euclidean space  $\mathbb{S}^2 \rightarrow \mathbb{R}^2$  under the assumption of proximity of corresponding landmarks. The average over corresponding landmarks is computed in the Euclidean space and is then rescaled to the sphere to guarantee the average to be located on the sphere. The landmarks are projected onto the tangent plane at that approximated average to enable Euclidean statistics.

**Euclidean Median as Landmark Mean Estimator** As stated in earlier studies [71, 72], the extracted sulcal curves can contain incorrectly identified sulcal labels, which can yield significantly large errors affecting the computation of the group-wise entropy over the sphere. Unfortunately, it is difficult to handle such mislabeled curves without manual modification. This issue can be robustly handled via landmark mean estimation by using the median of the corresponding points rather than the Euclidean mean. The median is more stable and reliable than the mean of the projected landmarks. For the  $k$ th landmark, the estimate is given by  $\bar{v}_k = \text{Median}\{M_1(v_k^1), M_2(v_k^2), \dots, M_N(v_k^N)\}$ . The tangential plane is defined at that median,  $\bar{v}_k$ , over the landmarks  $k$ .

**Weighting for Landmark Error Handling** As stated before, my sulcal labeling method can mislabel curves [71]. The mislabeled sulcal data can influence the covariance matrix; they generally lead to higher entropy. In order to minimize the influence of such mislabeled sulcal landmarks, a weighting function is employed to weight the Euclidean distances in the tangent plane similarly as employed in pair-wise registration; the same weighting function (Equation 4.4 and Equation 4.5) is employed for this purpose, where large distances contributes less during entropy computation as these landmarks are highly likely to be mislabeled.

### 4.4.3 Entropy of Multidimensional Geometric Properties

In addition to sulcal depth, my group-wise correspondence can be further improved by incorporating geometric properties (e.g. shape index, curvedness, etc.). The idea in [75] is to extend my method to incorporate a multidimensional geometric property map rather than using a single scalar map. Let  $\mathbf{s}(\cdot)$  denote a multiple tuple of the property map at a given point and  $v^j$  be the point in the  $j$ th subject such that  $u = M_j(v^j)$ , where  $u$  is a given point on the sphere. Given  $M_j$ , let  $v^j$  be a corresponding vertex to  $u$ . It holds  $\mathbf{s}(M_1(v^1)) \cong \dots \cong \mathbf{s}(M_N(v^N))$  if shape correspondence is well established. By the icosahedron subdivision-based spherical sampling of  $u$ , geometric properties are sampled and incorporated into the entropy minimization problem. To normalize the property maps, each property is then transformed into  $z$ -score prior to optimization.

### 4.4.4 Entropy Minimization

Consider a model  $\mathbf{x}(M_j)$  as an instance of  $\mathbf{X}$  such that

$$\mathbf{x}(M_j) = [proj_{\bar{v}_1}(M_j(v_1^j)), \dots, proj_{\bar{v}_n}(M_j(v_n^j)), S(\{M_j(v^j)\})]^T, \quad (4.10)$$

where  $proj(\cdot)$  denotes the projection of a vertex onto the tangential plane at the median over the corresponding landmarks, and  $S(\cdot)$  is multidimensional geometric properties.

For highly complex and variable shapes, surface triangle flips are often observed during optimization as there is no such regularization in Equation 4.12. This can lead to overfitting the resulting deformation fields. To address this issue, an additional term  $F$  is introduced to count the number of flips with respect to surface normals of the deformed spheres. Since

having no triangle flip is desired during optimization, the final entropy is therefore given by

$$H[\mathbf{X}] = \begin{cases} \frac{1}{2} \sum \ln \lambda & F = 0, \\ \infty & \text{otherwise,} \end{cases} \quad (4.11)$$

For the density estimation, assume a multivariate Gaussian distribution with covariance  $\Sigma$  and therefore, the entropy is obtained by

$$H[\mathbf{X}] \approx \frac{1}{2} \sum \ln \lambda + \text{const}, \quad (4.12)$$

where  $\lambda$  are the eigenvalues of  $\Sigma$ . By letting  $\bar{\mathbf{x}}$  be the sample mean and  $\mathbf{z} = [\mathbf{x}(M_1) - \bar{\mathbf{x}}, \dots, \mathbf{x}(M_N) - \bar{\mathbf{x}}]$ , the sample covariance is given by  $\frac{1}{N-1} \mathbf{z} \mathbf{z}^T$ . In general, the dimension of  $\mathbf{X}$  is much larger than  $N$ , which is computational demanding. Instead, the eigenvalues of  $\frac{1}{N-1} \mathbf{z}^T \mathbf{z}$  are computed in the dual space for computational efficiency. The optimization uses the same NEWUOA optimizer [99] for solving the entropy cost function as in the pair-wise correspondence.

#### 4.4.5 Hierarchical Optimization

There are two options available for hierarchical optimization to expedite the computation: incremental coefficient computation and hierarchical subgroup division.

**Incremental Coefficient Computation for High Degree of SPHARM** It can be easily observed that the computation time depends mainly on the number of landmarks and geometric properties (e.g., sulcal depth) over the sphere. Thus, the computational time is

directly associated and the eigenvalue computation. A nice property of the spherical harmonics decomposition is the orthonormality of its basis functions, which makes it possible to compute coefficients in an independent way for sets of basis functions. To reduce computation time, initial computation is performed on coefficients in blocks of  $l_{block}$  size. That is, the method starts with the first  $l_{block}$  low degrees, then the next lowest  $l_{block}$  degrees while fixing the already computed coefficients. Once all coefficients have been obtained this way, all coefficients are optimized over together to further tune the coefficients to reach optimal values.  $l_{block}$  is empirically set to 3 in the experiment.

**Subgroup Division Strategy for Large Population** The proposed group-wise correspondence is established via entropy minimization, depending heavily on computing the covariance matrix and a product of its eigenvalues (determinant). In general, the covariance matrix is non-sparse. As discussed in [1], therefore, the eigenvalue computation takes  $O(N^{2.373})$  time for an  $N \times N$  matrix under the assumption that an arithmetic operation with individual elements has complexity  $O(1)$ . This issue can be handled in a hierarchical manner to reduce the size of the covariance matrix. In particular, a population can be divided into several subgroups, and then each subgroup’s correspondence can be established to create the subgroup’s average model. This is a recursive process, in which subgroups of the (prior average) shape models are hierarchically generated. Once such a hierarchical optimization is completed, the intermediate coefficients are employed to deform the sphere for shape correspondence across the entire population. For better subgroup division, one can use any shape-based clustering such as PCA.

## 4.5 Shape Correspondence Evaluation

This section presents two shape correspondence evaluation methods: average shape model reconstruction and surface coloring.

### 4.5.1 Average Shape Model Construction

An advantage of the spherical harmonics representation is the continuous, smooth reconstruction of signals on the sphere. This allows surface models to determine their corresponding points at any given points. To take advantage of this spherical harmonic property, these surfaces are resampled via the icosahedron subdivision and find their corresponding points from the deformation field defined by the proposed spherical harmonic representation. For each sampling point, the average location ( $x$ -,  $y$ -, and  $z$ -coordinates) over the corresponding points was computed to generate a average surface model after Procrustes alignment based on the proposed shape correspondence.

### 4.5.2 Correspondence Evaluation via Surface Coloring

I also propose a sulcal curve-based coloring by propagating colors assigned to sulcal curves over the entire cortical surface in order to provide a visual quality assessment of the established correspondence. Since only few curves with distinct colors are available, I aim at propagating those colors over the entire surface. To generate the reference colorized template surface, each RGB channel was independently interpolated to the full surface via spherical harmonic decomposition on the spherical parametrization (see Figure 4.7). Due to no ground truth being available in my experiments, this visualization allows evaluating correspondence between multiple surfaces effectively, as corresponding locations are visualized with the same

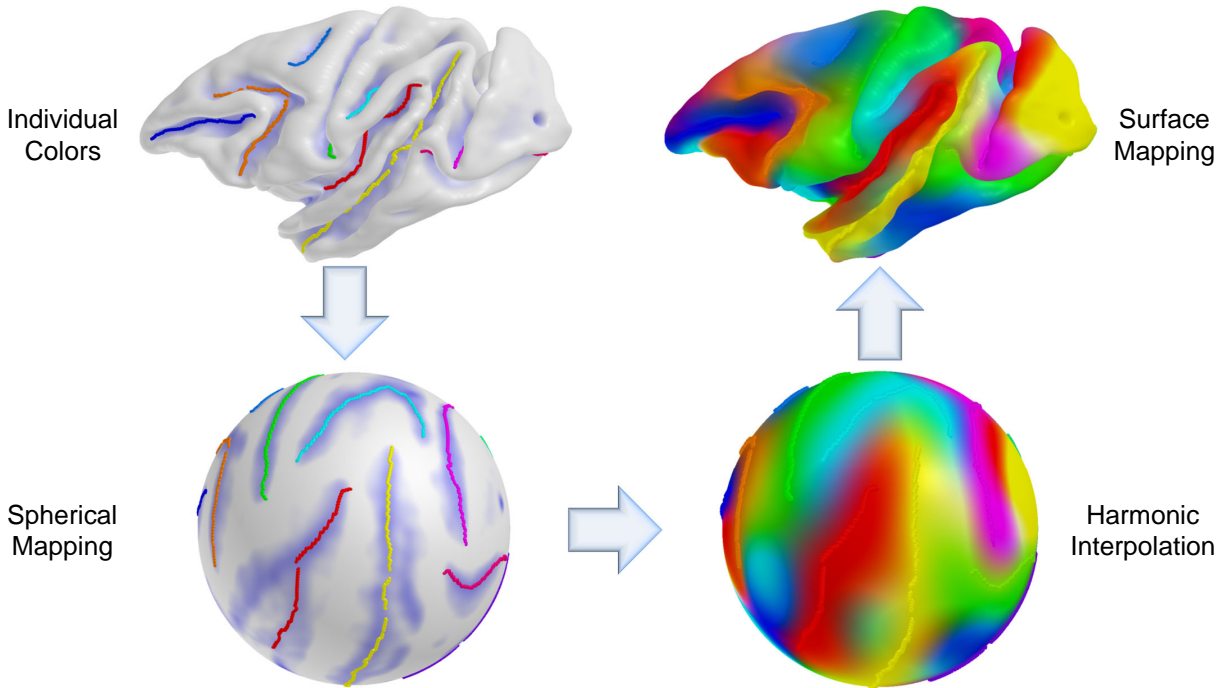


Figure 4.7: Cortical surface coloring using spherical harmonic interpolation. An individual curve has its own color for propagation and the sulcal curves are then mapped onto the sphere. For each RGB channel, a color intensity is interpolated with a combination of harmonic basis functions, and the color maps obtained via interpolation are remapped onto the original space (cortical surface).

color.

## 4.6 Materials

I applied my method on non-human primate/human cortical surfaces for quantitative evaluation, and I used an additional primate molar dataset to highlight the flexibility and extendibility of my method.

### 4.6.1 Macaque Cortical Dataset

18-month-old macaques were imaged under anesthesia at the Yerkes Imaging Center (Emory University, GA) on a 3T Siemens Trio scanner with an 8-channel phase array trans-

receiving volume coil using MPRAGE with GRAPPA optimized to a high resolution at  $0.6 \text{ mm} \times 0.6 \text{ mm} \times 0.6 \text{ mm}$  (TR = 3,000 ms, TE = 3.33 ms, flip angle =  $8^\circ$ , matrix =  $192 \times 192$ )<sup>2</sup>. The cortical surfaces were reconstructed via the CIVET pipeline [48]. The 9 major curves were employed on the left hemispheres: central, arcuate, principal, superior temporal, lunate, cingulate, intraparietal, occipito-parietal, and sylvian sulcus.

#### 4.6.2 IBIS Paediatric Cortical Dataset

Pediatric 2-year-old subjects were acquired on 3T Siemens Tim Trio scanners at  $1 \text{ mm} \times 1 \text{ mm} \times 1 \text{ mm}$  resolution with  $T_1$ -weighted (160 slices with TR = 2400 ms, TE = 3.16 ms, flip angle =  $8^\circ$ , matrix =  $256 \times 256$ ) and  $T_2$ -weighted (160 slices with TR = 3200 ms, TE = 499 ms, flip angle =  $120^\circ$ , matrix =  $256 \times 256$ ) scans. 25 subjects were randomly selected from scans acquired as part of the Infant Brain Imaging Study (IBIS) network at four different sites (University of North Carolina at Chapel Hill, University of Washington at Seattle, Washington University at Saint Louis, and the Children’s Hospital of Philadelphia)<sup>3</sup>. The cortical surfaces were reconstructed via the CIVET pipeline [48]. The 13 major sulcal curves on each left hemisphere were manually delineated: superior temporal (STS), inferior temporal (ITS), temporo-occipital (TOS), central (CS), precentral (PreCS), postcentral (PostCS), inferior frontal (IFS) and superior frontal (SFS), intraparietal (IPS), cingulate (CingS), calcarine (CalcS), occipito-parietal (OPS), and sylvian (SylS) sulci.  $l$  was set to 15 as degrees of

---

<sup>2</sup>All experiments described in this study were performed in accordance with the NIH Guide for the Care and Use of Laboratory Animals and approved by the Emory University Institutional Animal Care and Use Committee (IACUC).

<sup>3</sup><http://www.ibis-network.org>, IRB approval, Informed consent was obtained from all parents of participants for screening and evaluations.

spherical harmonic basis functions. For the macaque data the 9 major curves on the left hemispheres were labeled including the central, arcuate, principal, superior temporal, lunate, cingulate, intraparietal, occipito-parietal, and sylvian sulci.

### 4.6.3 Non-human Primate Molar Shape Dataset

The shapes analyzed in this study consist of 12 second mandibular molars from 6 living or fossil euarchontan species: *Donrussellia* (subject 1, 2), *Pronothodectes* (subject 3, 4, 11, 12), *Saxonella* (subject 5), *Ptilocercus* (subject 6, 7), *Altanius* (subject 8, 9), and *Elphidotarsius* (subject 10). These molars are a subset of the sample utilized by Boyer et al. [8]; a detailed explanation of sample preparation can be found in [7]. In brief, molds of actual toothrows were molded using a polyvinylsiloxane material (PresidentJet Plus) and cast in epoxy (EpoTek 301). The second mandibular molar was trimmed from the tooth row and scanned with the Scanco  $\mu$ CT-40 machine at Stony Brook University’s Center for Biotechnology. Three-dimensional surfaces of each tooth were segmented from the resulting DICOM or TIFF stacks using Amira 5.1 or Avizo 6.0. SPHARM-PDM was then employed to create surface models with a spherical topology. For landmark labeling, five distinct molar cusps were manually annotated on each surface model. Figure 4.8 shows a complete set of the molars.

## 4.7 Results

My proposed method was applied on the dataset described above to evaluate the established correspondence quality. Since there exists no ground-truth for a cortical correspondence, comparisons were made with the initial spherical mapping and the pair-wise method via analyses on cortical thickness as well as the agreement with manually extracted sulcal curves.

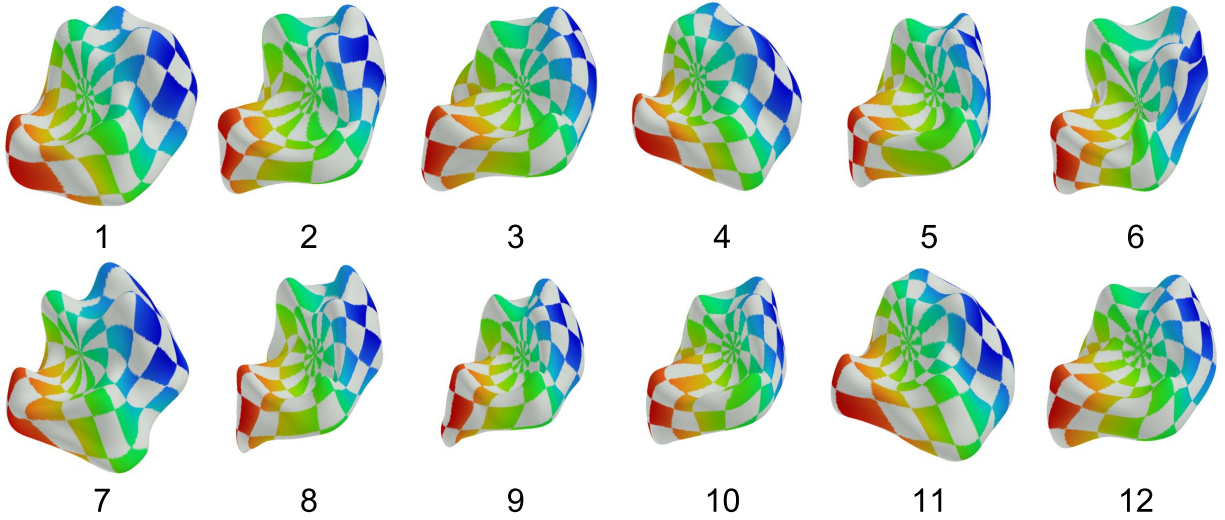
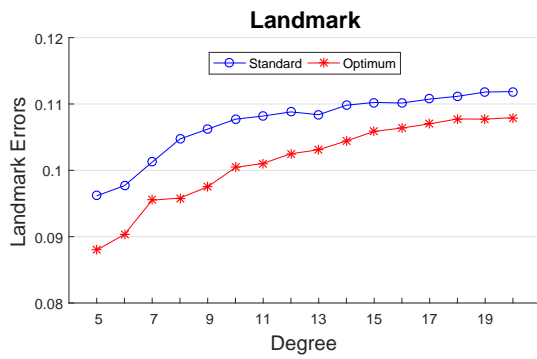


Figure 4.8: A complete set of 12 primate fossil molar shapes with their shape correspondence (different colors) established by the proposed method.

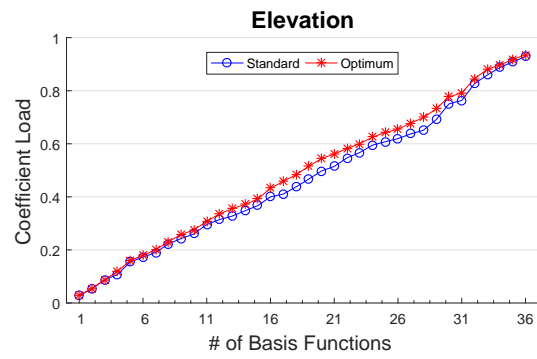
The experimental results showed consistency and reliability through quantitative and visual comparisons with the existing methods.

#### 4.7.1 Optimal Pole Selection

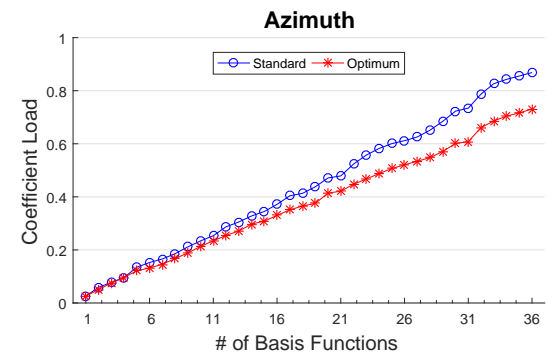
A leave-one-out cross-validation technique was applied for evaluation of the optimal pole selection, in which a single sulcus is removed from each individual subject during registration and measured landmark (reconstruction) errors between the removed sulcus reconstructed by the deformation field and its corresponding one in the template. Figure 4.9 shows the smaller average reconstruction errors for the optimal pole and the reduced coefficient load of the azimuth displacement for the high-frequency harmonic basis functions by the proposed pole selection.



(a)



(b)



(c)

Figure 4.9: Reconstruction errors by a pole selection. (a) landmark errors and cumulative coefficient load for (b) elevation and (c) azimuth displacements. The optimal pole selection yields less landmark reconstruction errors than the standard pole selection. No major differences are observed for the elevation displacements, whereas for the azimuth displacements, the total amount of the coefficient load significantly decreases for the optimal pole selection.

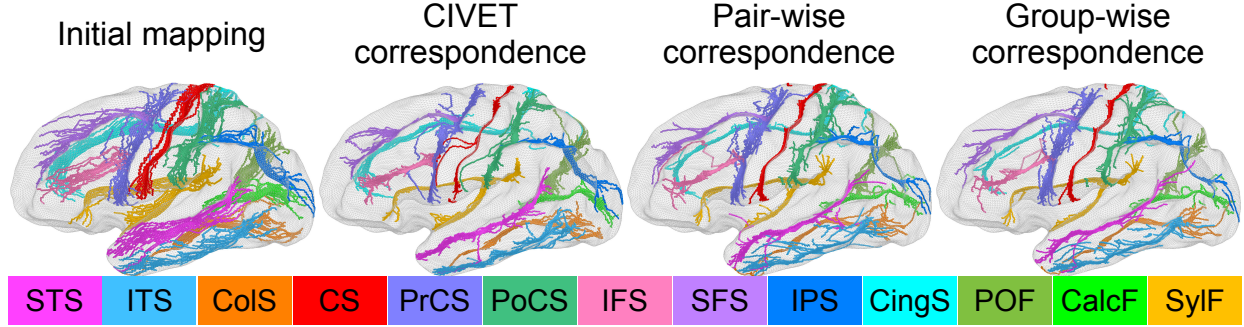


Figure 4.10: Sulcal curve alignment by (1st column) initial spherical mapping, (2nd) CIVET correspondence, (3rd) pair-wise correspondence, and (4th) group-wise correspondence.

	STS	ITS	ColS	CS	PrCS	PoCS	IFS
CIVET	12.0908	12.2759	12.6610	12.2135	13.0999	11.7675	9.5944
Group-wise	11.9334	13.0723	11.1198	12.0140	12.6433	12.1376	7.9299
	SFS	IPS	CingS	POF	CalcF	SylF	
CIVET	12.2897	12.2183	15.9611	9.9457	14.3972	12.0675	
Group-wise	11.7407	11.8827	15.8695	9.6593	11.6527	11.3509	

Table 4.1: Sulcal curve entropy measured based on the proposed metric. Most major sulcal curves achieve small entropy except for ITS and PoCS due to a difficulty in automatic sulcal labeling.

#### 4.7.2 Sulcal Curve Variability

It is important to investigate how tightly the sulcal curves were aligned in the group-wise common space. Only automatically labeled curves were used for the cortical correspondence establishment. Also, the manually delineated curves were employed for validation purpose only and thus were independent of the optimization step in the proposed method. Visually the mapped major sulcal curves showed improved agreement in several regions as compared to the pair-wise correspondence shown in Figure 4.10. As shown in Table 4.1, the proposed method achieved lower entropy except for ITS and PoCS as compared to that computed via CIVET. This is because ITS and PoCS labelings are more difficult to establish during automatic sulcal labeling.

	depth		thickness	
	mean	std	mean	std
CIVET	1.1996	0.5103	0.4942	0.3314
initial	2.1313	0.9938	0.5317	0.3547
pair-wise	1.5815	0.8358	0.4996	0.3539
group-wise	1.5568	0.8180	<b>0.4712</b>	<b>0.3375</b>

Table 4.2: Variances of cortical properties for different correspondence methods (unit: *mm*): For both sulcal depth and thickness variances, the proposed method shows significant differences against both the initial mapping and the pair-wise method ( $p < 0.0001$ ).

### 4.7.3 Variance over Sulcal Depth Maps and Cortical Thickness

For quantitative evaluation on the correspondence quality, cross-subject variance estimates of sulcal depth were first measured over all vertices on the entire surface across subjects. However, such an evaluation is biased, as I employ sulcal depth maps in the cost function. Thus, I also considered variance estimates of cortical thickness as well as visual assessment of manually labeled sulcal curves for unbiased evaluation. In Table 4.2, the variance analysis indicates superior performance of the proposed method for sulcal depth and cortical thickness measures, with significant differences to both the initial mapping and the pair-wise method, revealed by Student’s *t*-test ( $p < 0.0001$ ).

### 4.7.4 Visual Validation on Macaque Dataset

The cortical correspondence on the macaque dataset is obtained by applying my proposed group-wise correspondence. In Figure 4.11, the proposed group-wise correspondence method shows qualitative improvement over the pair-wise correspondence.

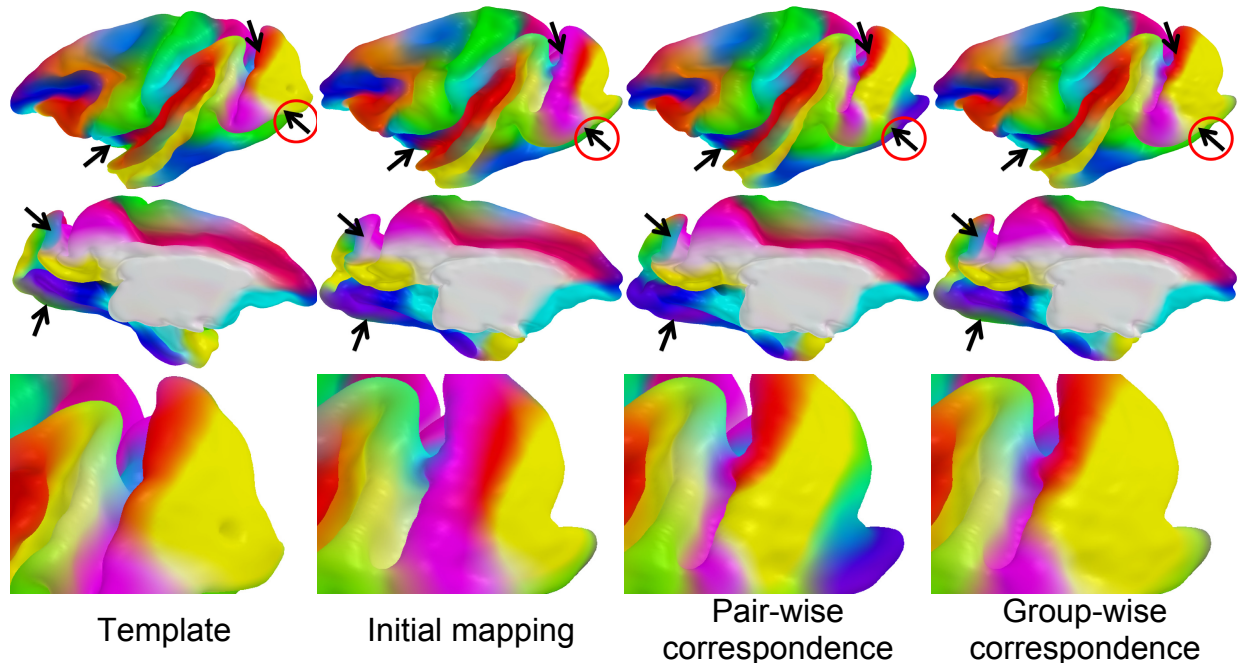


Figure 4.11: Visual comparison of correspondence results: (1st column) the colored template surface is propagated to a selected, representative example surface via (2nd) the initial spherical mapping, (3rd) pair-wise correspondence, and (4th) group-wise correspondence. The arrows indicate areas of visual differences across the correspondence methods. Visually well-distinguishable regions are circled in red.

#### 4.7.5 Evaluation of Average Shape Models

A primate molar dataset was used for evaluation of the proposed group-wise method. For the primate molar shape correspondence, I used two geometric properties: curvedness and shape index proposed in [51] (see also Section 2.2 for details). Those two properties are of complementary geometric characteristics, in that regions not covered by curvedness are well represented by shape index and vice versa. For the weighting balance between landmarks and geometric properties, it can be observed that the equally weighted optimization achieves the best representation of the population average. In Figure 4.12, the average model generated by the proposed method nicely captures five molar cusps and enhanced sharpness of the ridge/valley of the average model. That average model also well represents variance of each

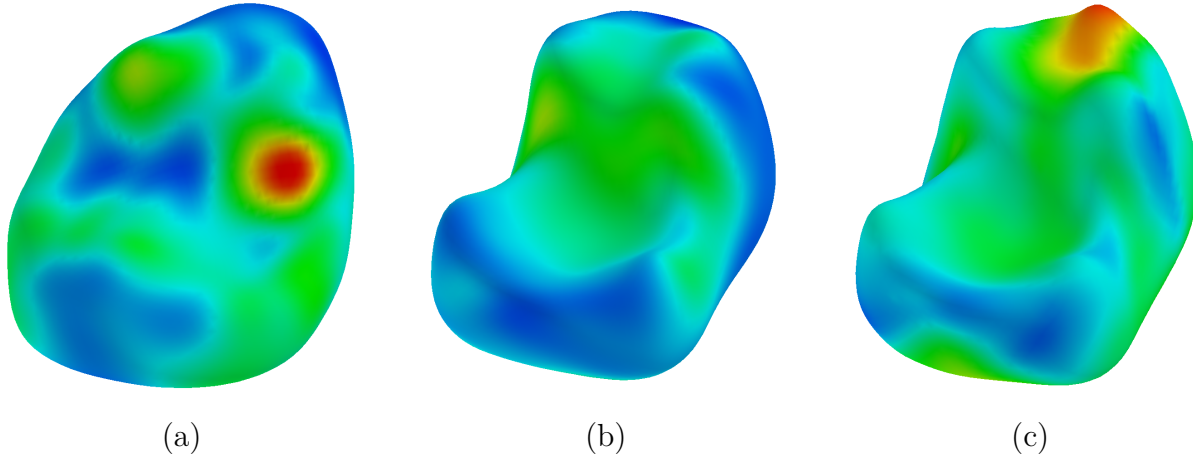


Figure 4.12: Average model reconstruction of 12 primate molar shapes with different shape correspondence: (a) initial SPHARM-PDM, (b) rigid transformation in  $\mathbb{S}^2$ , and (c) the proposed group-wise shape correspondence. The colors indicate location variance at each vertex (color scale: 0 - 0.1 (blue - red)). The group-wise correspondence clearly captures five cusps across multi subjects, whereas most cusps are hard to see in (a) and one cusp is missing in (b).

area especially in the most anterior cusp that has a high variability across species.

To quantitatively evaluate the average shape models (and their shape correspondences), I used two model evaluation techniques: generalization (the ability to describe instances outside of the training set) and specificity (the ability to represent only valid instances of the object) as described in [20]. Figure 4.13 illustrates generalization and specificity of the average models. In both cases, it was observed that the reconstruction errors of the proposed method are smaller than those of other methods. Also, the proposed method achieved high compactness that the largest eigenvalue of the proposed method is relatively high. This indicates that the eigenvalue better explains a majority of the shape variability.

#### 4.7.6 Principal Component Analysis on Molar Shapes

As an application to shape classification, principal component analysis (PCA) was applied on the primate fossil molars using different PCA models reconstructed by three correspon-

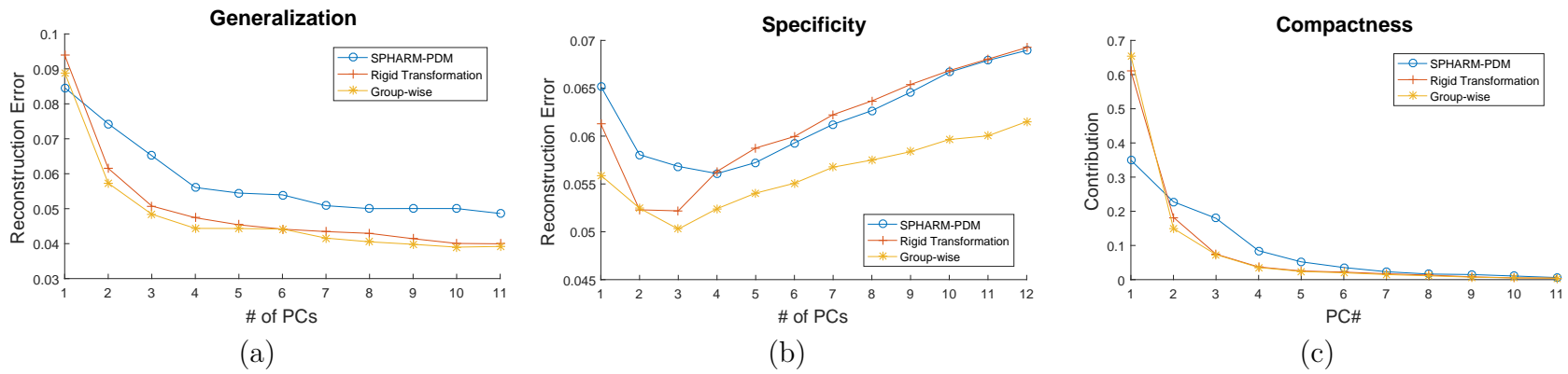


Figure 4.13: Shape correspondence evaluation using reconstruction error on the primate molar dataset: (a) generalization, (b) specificity, and (c) compactness. The proposed method achieves better generalization and specificity in terms of the instance reconstruction error. Also, the largest eigenvalue gives higher contribution of the shape variability than in other methods. This implies that only few principal components are enough for the shape reconstruction with small reconstruction errors.

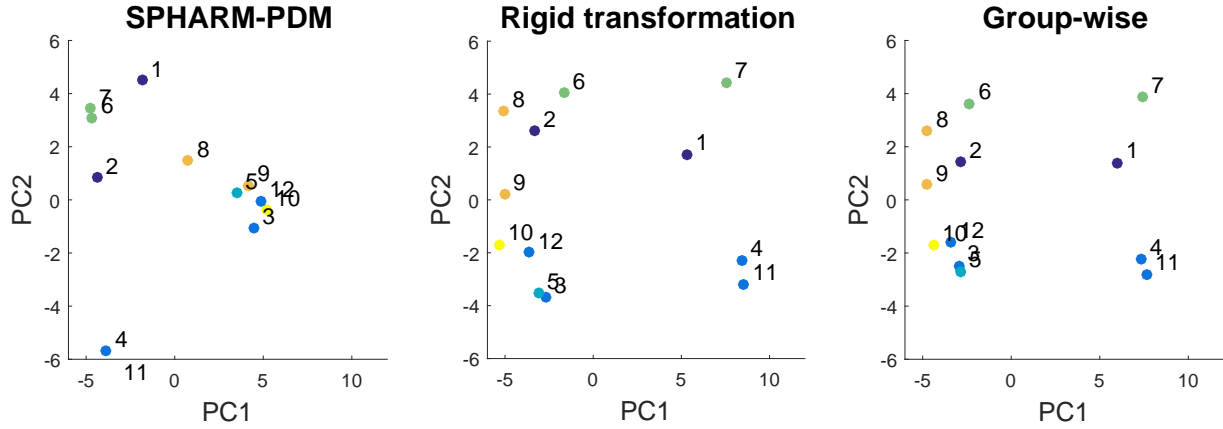


Figure 4.14: Primate fossil molar shape space defined by different correspondences. The species are labeled by color: *Donrussellia* (subject 1, 2), *Pronothodectes* (subject 3, 4, 11, 12), *Saxonella* (subject 5), *Ptilocercus* (subject 6, 7), *Altanius* (subject 8, 9), and *Elphidotarsius* (subject 10). Group-wise correspondence shows slightly better separation than rigid correspondence along PC2; *Donrussellia* has similar values along PC2 for example.

dences (SPHARM-PDM, rigid transformation, and proposed method). As compared to the initial correspondence, both rigid transformation and the proposed method can nicely separate the topmost peak that has the largest variation across subjects. It can be easily determined whether the location of the topmost peak is left or right according to that separation. In Figure 4.14, the topmost peaks of subject 1, 4, 7, and 11 are located to the same side (also see Figure 4.8) along the first principal direction. There was no significant difference of the first principal direction between rigid transformation and the proposed method, yet for several species (*Donrussellia*, *Ptilocercus*, and *Pronothodectes*) they were better classified along the the second principal direction in the proposed method.

## 4.8 Summary

This chapter presented an automatic group-wise cortical correspondence method that estimates a smooth continuous deformation field using entropy minimization incorporating two terms: sulcal landmarks for local alignment and sulcal depth map for the cortical regions

that are not covered by sulcal curves. The proposed framework is versatile, so it further allows an extension to multidimensional geometric properties, which is not limited to a specific population. To overcome potential mislabeling in the sulcal curve labeling procedure, I used two robust metrics: median estimation of the sulcal points on the tangential plane and weighted distances for reduction of mislabeling influences. To measure sulcal curve alignments, an entropy-based metric is employed that quantifies variability in the sulcal alignment. In addition, surface triangle regularity was addressed by introducing an additional regularization term during the optimization. A detailed description of cortical surface coloring was demonstrated for visual comparisons.

In my experiments, the proposed method outperformed the pair-wise method in human subjects via quantitative analysis and visual comparisons as well as in non-human subjects via visual assessment. Statistical analysis also provided evidence that the proposed method has better consistency and reliability on different dataset as compared to the existing CIVET method ( $p \leq 0.001$  in both cases). Specifically, for consistency the proposed method achieved tighter sulcal curve alignment and sharper sulcal depth map average. Also, the shape correspondence established by the proposed method achieved a tight and reliable alignment, and the average model nicely captured inter-subject variability in visual and quantitative comparisons.

## CHAPTER 5: SULCAL SHAPE-AWARE QUANTIFICATION OF CORTICAL FOLDING

### 5.1 Overview

An appropriate quantification of the cortical folding is a critical step for surface-based cortical folding analyses. However, a consistent cortical folding analysis is a challenging due to highly complex and variable nature of human cortical folding patterns. In general, cortical folding quantification consists of two major components: 1) the cortical folding metric definition and 2) the local region definitions over which the metric is computed. This chapter focuses on the latter, i.e., the design of a local region size/shape (geodesic kernel) on the cortical surface such that this region is locally adaptive to sulcal and gyral patterns. Initial attempts to quantify cortical gyrification were made by observation from the cortical folding change during mammalian evolution [42, 29]. In their approach the evolution process was assumed that the cortical surface is deformed from a simple convex hull-like surface. As discussed in Section 1, although the ground truth of cortical gyrification remains largely unclear yet, I follow the same idea of the evolution process as proposed in [42, 29]. Recent approaches employing the 3D convex hull are also found in [110, 56].

By defining local regions along sulci and gyri, cortical patterns with similar functions are more likely to be captured with the same region. In contrast, existing methods employ regional kernels typically without taking cortical folding into account. To compensate, the

commonly chosen kernel size is large and subsequently covers multiple sulcal regions that are less functionally related. This often results in smoothing out the detailed representations of cortical folding, consequently blurring folding measurements as well. In this chapter, a novel sulcal-shape aware kernel for cortical folding analyses is proposed with the aim of less blurring and more biologically plausible quantification of local gyrification. In contrast to conventional kernel-based approaches, it is important for such an adaptive kernel design to investigate the geometric properties of the local cortical shape. Briefly, the proposed method consists of two components: 1) local cortical region segmentation and 2) adaptive kernel creation based on the region segmentation. Figure 5.1 illustrates a schematic overview of the proposed pipeline.

Section 5.2 defines the objective of this chapter. Section 5.3 describes the outer hull creation needed for the computation of local gyrification indices and the correspondence establishment between the hull and the pial surface. Section 5.4 describes a sulcal/gyral curve-based cortical region segmentation. Section 5.5 presents a travel-time map computation from this segmentation required in Section 5.6 to define a tensor field. Finally the tensor field leads to the generation of the shape-adaptive kernel and the local gyrification index in Section 5.7.

## 5.2 Objective

The objective of this work is to design a cortical-shape-adaptive kernel taking into account information of sulcal and gyral regions. As highlighted in existing anatomic label maps [134, 22, 138], there are several distinguishing regions on the cortex: sulcal fundi (valleys), gyral crowns (ridge like regions), and sulcal banks (flat regions). I design an adaptive kernel

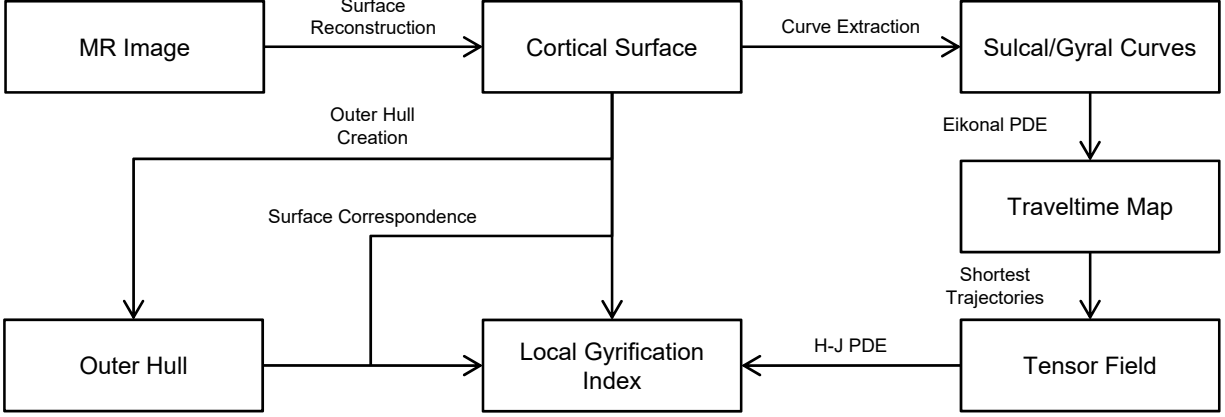


Figure 5.1: A schematic overview of the proposed pipeline.

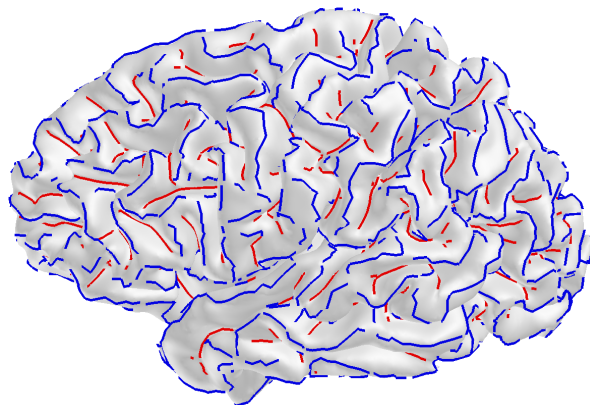
to capture these cortical regions via two different kernel shapes:

- At sulcal fundi/gyral crowns: an elongated kernel along the fundi and crowns
- At sulcal banks: an isotropic kernel that uniformly covers sulcal banks

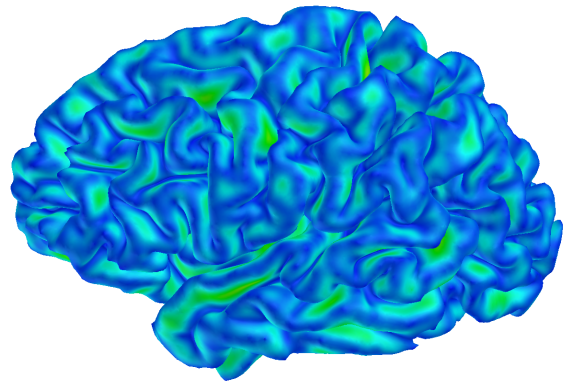
In order to make it more specific, the kernel design problem can be transformed into performing wavefront propagation over the cortical surface. In terms of wavefront propagation, the desirable kernel design can be redefined equivalently as follows.

- At sulcal fundi/gyral crowns: anisotropic speed faster along the fundi and crowns
- At sulcal banks: isotropic speed in every direction

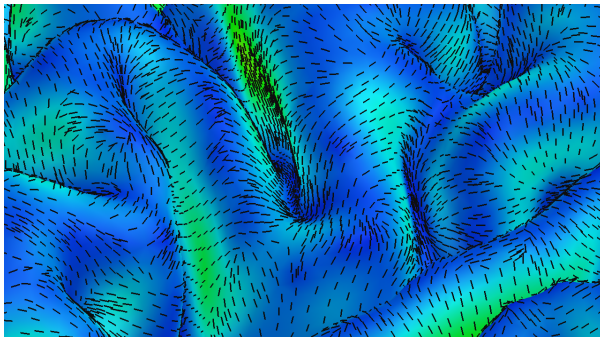
From this definition, the next question is how to design a tensor field for the wavefront propagation to follow the above properties. Thus, my proposed kernel design can be achieved in several steps: 1) sulcal/gyral region segmentation, 2) complete region segmentation based on the segmented sulcal/gyral regions, 3) tensor estimation at every location of the surface, and 4) local kernel creation via wavefront propagation on the tensor field. Figure 5.2 illustrates an overview of the tensor field computation.



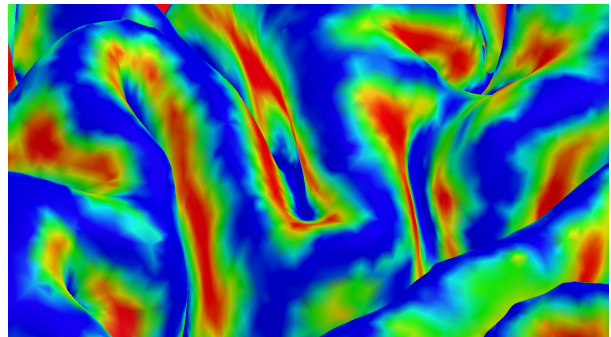
(a) a set of sulcal/gyral curves  $\zeta$



(b) travel-time map  $T$



(c) gradient map  $\nabla T$



(d) normalized travel-time map  $S$

Figure 5.2: An overview of the tensor field computation. (a) Sulcal (*red*) and gyral (*blue*) curves are automatically extracted from the cortex as sources for wavefront propagation. (b) Travel-time to every vertex is computed by solving the eikonal equation. (c) A gradient map is obtained in the tangent space of the cortex. (d) The travel-time map is normalized to capture cortical properties: sulcal fundus/gyral crown (*blue*) or sulcal bank (*red*).

### 5.3 Outer Hull Creation and Correspondence Establishment

The main idea of my proposed kernel-based local gyrification quantification is to measure an area ratio between a cortical region and its corresponding region on the outer hull. Thus, a key step is to create an outer hull as a reference that compactly contains a given pial surface and to establish a surface correspondence between them. As proposed in [46], a morphological closing operation is applied to the pial surface in the volume space to create an outer hull that tightly envelops the pial surface, following the same parameter setting as used in [110]. Briefly, the pial surface is transformed into a binary volume, and then a morphological closing operation is applied to sulci using a sphere of 15 *mm* diameter as the structural element. This results in an outer hull in the volume space. For correspondence establishment the surface evolution method [58] is then applied to trace sub-voxel accuracy trajectories from the pial surface to the outer hull in the volume space by solving the Laplacian equation. As shown in several studies [43, 62], such a method guarantees a bijective, smooth correspondence and no intersections across trajectories. Finally, the outer hull is obtained by replacing vertices of the original pial surface with the endpoints of the trajectories touching the outer hull in the volume. In the experiment, the same voxel size to compute the surface evolution is used as provided in the original input volume.

### 5.4 Sulcal/Gyral Curve Extraction

Cortical region segmentation into sulcal and gyral regions is needed to classify each cortical region at which an adaptive kernel is created. As initialization, sulcal/gyral curves can guide the sulcal/gyral cortical region segmentation. For this purpose the automatic sulcal curve

extraction method presented in Chapter 3 is employed to obtain the sulcal/gyral curves from the cortical surface. Then, this sulcal curve extraction is applied to inversely extract gyral curves as shown in [77]. Briefly, the method consists of two main steps: 1) sulcal/gyral point selection using a line simplification method and 2) curve delineation by tracing the selected points, constrained by a smoothing term. In the sulcal/gyral point selection, the point is evaluated along the direction associated with the principal curvature. The final curves are of a piece-wise point set constrained by curvature smoothness. For the remainder of the chapter,  $\zeta$  denotes a set of the extracted gyral curves. The pial and white matter surfaces are employed to accommodate the differing sharpness of sulcal fundus/gyral crown in these two surfaces. Sulcal curves are extracted from the pial surface while gyral curves are extracted from the white matter surface. The resulting gyral curves are projected onto pial surface using the surface correspondence between the pial and white matter surfaces. Figure 5.2a shows an example of the extracted sulcal/gyral curves on the pial surface.

## 5.5 Travel-time Map

As mentioned before, an adaptive kernel can be obtained via wavefront propagation driven over a tensor field of the cortical surface. For this purpose, the entire cortical surface needs to be segmented to define a tensor at every location of the cortex. This can be achieved by extending the extracted sulcal/gyral curves (see Section 5.4). Specifically, for the entire cortical surface segmentation a travel-time map  $T$  between sulcal/gyral curves is employed and is obtained by computing shortest trajectories from the sulcal curves  $\zeta$  to all the locations of the cortical surface. This is a shortest geodesic path finding problem at an isotropic speed at each location, which can be formulated by the eikonal equation by simplifying

Equation 2.14 described in Chapter 2. A set of points  $\in \zeta$  serves as sources of the wavefront propagation, and in Equation 2.14, let the tensor matrix  $M$  be the identity matrix  $I$ . Thus, with a boundary condition  $T(\mathbf{p}) = 0$  for  $\forall \mathbf{p} \in \zeta$ , Equation 2.15 becomes

$$F\left(\mathbf{x}, \frac{\nabla T(\mathbf{x})}{\|\nabla T(\mathbf{x})\|}\right) = 1. \quad (5.1)$$

For  $M = I$ , this rather reduces the H-J PDE to

$$\|\nabla T(\mathbf{x})\| = 1. \quad (5.2)$$

The solution provides a travel-time map  $T$  for all locations of the surface as illustrated in Figure 5.2b.

## 5.6 Tensor Field

To guide an adaptive kernel a tensor field over  $\Omega$  is computed from  $T$  via wavefront propagation. My goal is to design a kernel, in which the propagation speed is getting anisotropic as it reaches sulcal/gyral regions and isotropic as it reaches sulcal banks. The tensor field is decomposed into two components: principal propagation directions and their associated propagation speeds.

### 5.6.1 Principal Propagation Direction

It is important to determine the directions along which the propagation is performed. The basic idea is to utilize the orthogonal and tangent directions to the sulcal/gyral curves. However, since the curves exist only in few cortical regions, it is necessary in other regions

to define something acting like the curves, as well. For this purpose the iso-travel-time contours of  $T$  are employed. This modeling issue can thus be addressed by finding shortest trajectories (orthogonal to the contours) of  $T$  between sulcal fundi and gyral crowns. As defined in [113], the shortest trajectory for anisotropic equations is computed by tracing characteristic directions rather than gradients while they become coincident when it comes to the eikonal equation. Thus, as  $T$  encodes the minimum travel-times from the sources, the shortest geodesic trajectory is easily obtained along the gradient field  $\nabla T$ .

For a given point  $\mathbf{x} \in \Omega$ , its two principal propagation directions  $\mathbf{v}_1(\mathbf{x})$ ,  $\mathbf{v}_2(\mathbf{x})$  are defined in the tangent plane by letting

$$\mathbf{v}_1(\mathbf{x}) = \frac{\nabla T(\mathbf{x})}{\|\nabla T(\mathbf{x})\|} \text{ and } \mathbf{v}_2(\mathbf{x}) = \frac{\nabla T^\perp(\mathbf{x})}{\|\nabla T^\perp(\mathbf{x})\|}, \quad (5.3)$$

such that  $\nabla T(\mathbf{x}) \perp \nabla T^\perp(\mathbf{x})$ .  $\mathbf{v}_1$  encodes the tangent direction to the geodesic trajectory between the corresponding sulcal fundus and gyral crown, and  $\mathbf{v}_2$  does the orthogonal direction to  $\mathbf{v}_1$ . In a triangulated mesh, the mean curvature normal approximation is achieved by minimizing the Dirichlet energy using [83], and a local gradient  $\nabla T(\mathbf{x})$  is then obtained by the weighted mean of the projected first-order directional derivatives [141]. Figure 5.2c illustrates an example of  $\nabla T$ .

### 5.6.2 Principal Propagation Speed

The second modeling issue is to determine the speed associated with the principal propagation direction at the two cortical region types of sulcal fundi/gyral crowns and sulcal banks. For the former type it is desirable that the speed has minimum and maximum along

$\mathbf{v}_1$  and  $\mathbf{v}_2$ , respectively, which yields an elongated kernel as a result. On the other hand, the speed needs to be almost the same along every direction in the sulcal bank to produce an isotropic kernel. However, it can be easily observed that the middle of sulcal banks does not possess the same travel-time  $T$  over the entire surface as it varies at the depth of the corresponding sulcus. To better classify the local region type using  $T$  at a given point  $\mathbf{x} \in \Omega$ , a novel parametrization is required with respect to local regions such that  $T$  is normalized over  $\Omega$  ranging from  $\eta$  to 1 ( $0 < \eta \leq 1$ ).

The maximum travel-time is computed across the shortest trajectories passing through a given point and then normalize the travel-time at that point by the local maximum. Specifically, for a given point  $\mathbf{x} \in \Omega$  its source  $\mathbf{s}_\mathbf{x} \in \zeta$  is obtained by tracing gradients over  $-\nabla T$  until  $T = 0$  while holding  $T > 0$  and  $T(\mathbf{x}) > T(\mathbf{x} + \nabla T d\mathbf{x})$ . This gives a label map of  $\Omega$  that represents the source of any point  $\in \Omega$ . For a given source  $\mathbf{s}$ ,  $D_L(\mathbf{s})$  denotes its label region  $\subseteq \Omega$ , i.e.,  $D_L(\mathbf{s}) = \{\mathbf{x} \in \Omega | \mathbf{s}_\mathbf{x} = \mathbf{s}\}$ . Similarly, the maximum travel-time through  $\mathbf{x}$  is obtained by tracing over  $\nabla T(D_L(\mathbf{s}_\mathbf{x}))$  until it touches  $\partial D_L(\mathbf{s}_\mathbf{x})$ . The normalized travel-time map  $S$  is thus obtained via simple linear interpolation.

$$S(\mathbf{x}) = (1 - \eta) \cdot \frac{T(\mathbf{x})}{T_{\max}(\mathbf{x})} + \eta, \quad (5.4)$$

where

$$T_{\max}(\mathbf{x}) = \max_{\mathbf{y} \in D_L(\mathbf{s}_\mathbf{x})} T(\mathbf{y}). \quad (5.5)$$

$T_{\max}(\mathbf{x})$  is the maximum travel-time along the shortest trajectory from the source through  $\mathbf{x}$  and holds  $T(\mathbf{x}) \leq T_{\max}(\mathbf{x})$ . Thus, the normalized travel-time map  $S$  captures the region properties in an easy way; for example,  $S(\mathbf{x}) = 1$  if it belongs to the middle of a sulcal bank,

as shown in Figure 5.2d. Regardless of sulcal depth,  $S$  now supports consistent speed in the principal propagation direction  $\mathbf{v}_1$  and  $\frac{1}{S}$  to  $\mathbf{v}_2$ . They are reciprocal to each other to guarantee the amount of the propagation at any point in  $\Omega$  is constant, which is equal to 1.

### 5.6.3 Tensor Matrix

From Equation 5.3 and Equation 5.4, the new tensor matrix  $\tilde{M}$  is defined in the tangent plane as

$$\tilde{M}(\mathbf{x}) = S(\mathbf{x}) \cdot \mathbf{v}_1(\mathbf{x})\mathbf{v}_1(\mathbf{x})^T + S(\mathbf{x})^{-1} \cdot \mathbf{v}_2(\mathbf{x})\mathbf{v}_2(\mathbf{x})^T. \quad (5.6)$$

The tensor matrix  $\tilde{M}(\mathbf{x})$  ultimately guides the spatial-varying wavefront propagation. Recall that  $\eta$  is used to prevent  $M$  from being degenerative. The minimum bound  $\eta$  is thus employed as a regularization term. Furthermore, the H-J PDE governed by Equation 5.6 is convex because it holds the Lipschitz-continuity that bounds the propagation speed  $F$  such that  $0 < \eta \leq S \leq F \leq S^{-1} < \infty$ . As stated in [113], therefore, the propagation converges to a viscosity solution at the bounded propagation speed  $F$ . Note that the speed tensor  $\tilde{M}$  becomes isotropic when  $\eta = 1.0$ . Figure 5.3 shows behaviors of the proposed adaptive kernel varying in  $\eta$ .

## 5.7 Adaptive Kernel and Local Gyrfication Index

My proposed local-shape-adaptive kernel at  $\mathbf{x} \in \Omega$  is obtained by solving the H-J PDE equipped with the proposed tensor matrix  $\tilde{M}$  in Equation 5.6. In contrast to the conventional kernel-based approaches, the cortical surface is employed to define the kernel specifically suitable to the cortical folding while the kernel size is determined on the outer hull. Formally,

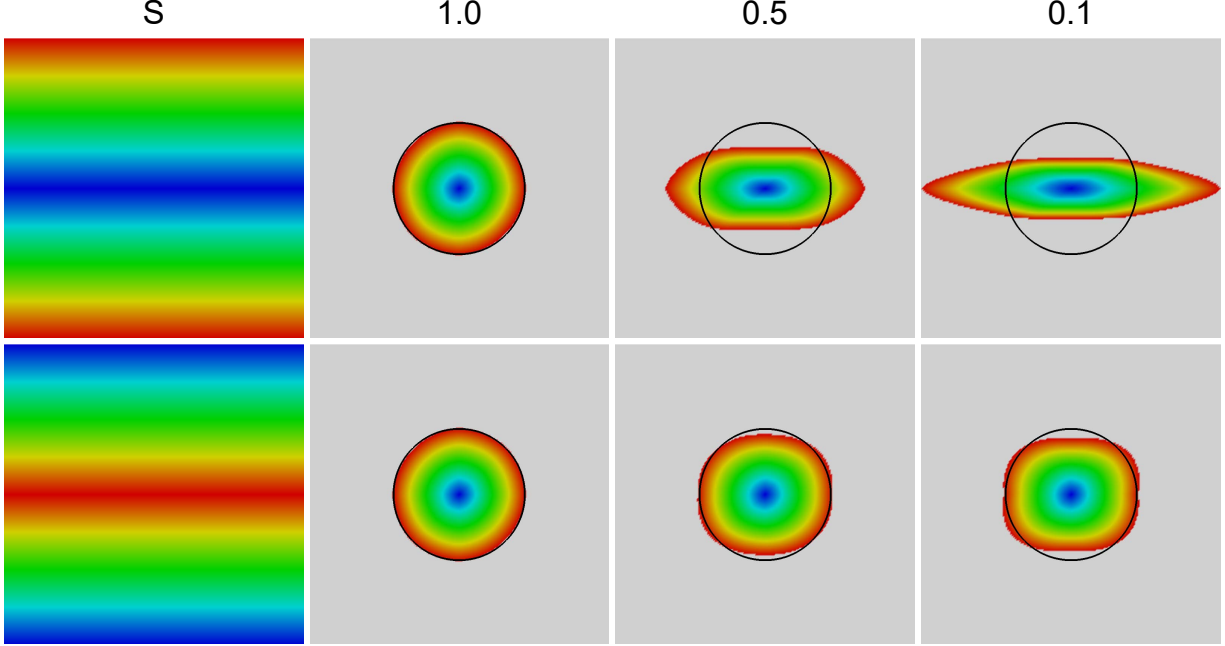


Figure 5.3: Two different types of synthetic normalized travel-time maps  $S$  on the plane and their kernel shapes with a constant area by varying  $\eta$  with a jet color scale (*blue - red*): 0-1. The respective travel-time maps are obtained from the center horizontal (*top*) and marginal horizontal (*bottom*) sources (*blue*). The kernel is created at the center of the map as a source point. The kernel is adaptively elongated faster as  $\eta$  becomes smaller (*top*), whereas the kernel remains as isotropic as possible even with a small value of  $\eta$  (*bottom*). From the second to fourth columns, the color indicates iso-contours over time.

the proposed wavefront propagation  $K$  for an adaptive kernel is formulated by recalling the H-J PDE that satisfies the following equation with a boundary condition  $K(\mathbf{x}) = 0$  such that

$$\|\nabla K(\mathbf{x})\| \cdot \left( \frac{\nabla K(\mathbf{x})^T}{\|\nabla K(\mathbf{x})\|} \tilde{M}(\mathbf{x}) \frac{\nabla K(\mathbf{x})}{\|\nabla K(\mathbf{x})\|} \right) = 1. \quad (5.7)$$

Once travel-time  $K$  is computed, a kernel can be created by tracing one of the iso-travel-time contours of  $K$ . Denote a bijective function between  $\Omega$  and  $H$  by  $f : \mathbb{R}^3 \rightarrow \mathbb{R}^3$ . Recall that  $f$  is established via a Laplace-based outer hull creation method so it is differentiable. To select a proper iso-travel-time contour at  $\mathbf{x}$  for the adaptive kernel creation, all the iso-travel-time contours of  $K$  are projected onto  $H$  via  $f$ . Then, a projected iso-travel-time contour is

chosen such that the area contained by the contour over  $H$  is equal to some positive constant (typically, user-defined parameter). Now assume that  $\Omega$  is parametrized by  $\varphi : \mathbb{R}^2 \rightarrow \mathbb{R}^3$  such that  $\varphi(u, v) = (x(u, v), y(u, v), z(u, v)) \in \Omega$ . Formally, given  $K$  and travel-time  $\delta$ , the corresponding area of  $H$  to the iso-travel-time contour ( $T = \delta$ ) is formulated as the following surface integral.

$$A_H(\mathbf{x}; \delta) = \iint_{D_A(\mathbf{x}; \delta)} \left\| \frac{\partial(f \circ \varphi)}{\partial u} \times \frac{\partial(f \circ \varphi)}{\partial v} \right\| dudv, \quad (5.8)$$

where  $D_A(\mathbf{x}; \delta) = \{(u, v) \in \mathbb{R}^2 | K(\varphi(u, v)) \leq \delta(\mathbf{x})\}$ . The resulting kernel is then determined by fixing the corresponding area of  $H$  by finding  $\delta$  such that  $A_H(\mathbf{x}; \delta)$  is equal to some constant function  $\rho(\delta) \in \mathbb{R}^+$ . Once  $\delta$  is obtained by solving Equation 5.8, the surface area of  $\Omega$  governed by  $\delta$  can be obtained as follows.

$$A_\Omega(\mathbf{x}; \delta) = \iint_{D_A(\mathbf{x}; \delta)} \left\| \frac{\partial\varphi}{\partial u} \times \frac{\partial\varphi}{\partial v} \right\| dudv. \quad (5.9)$$

From Equation 5.8 and Equation 5.9, my proposed local gyrification index is then given by the area ratio

$$lGI(\mathbf{x}; \rho(\delta)) = \frac{A_\Omega(\mathbf{x}; \delta)}{A_H(\mathbf{x}; \delta)} = \frac{1}{\rho(\delta)} A_\Omega(\mathbf{x}; \delta). \quad (5.10)$$

The local surface area for each vertex is approximated by using barycentric cells in a triangulated mesh. Figure 5.4 shows the different kernels applied to the actual human cortex at  $\rho = 316 \text{ mm}^2$ .

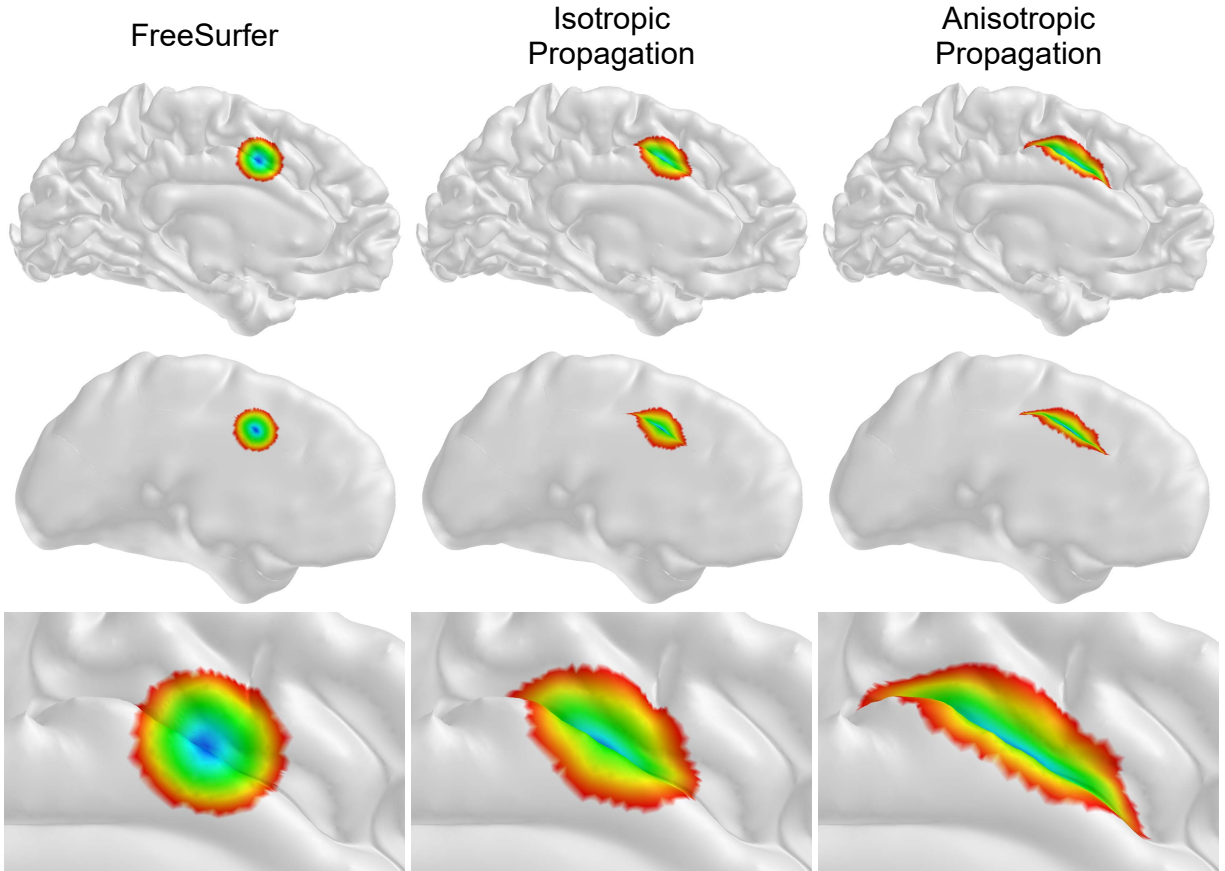


Figure 5.4: Kernels at an arbitrary example sulcal point on the same subject surface using different approaches with a fixed area on the outer hull  $\rho = 316 \text{ mm}^2$ . The circular kernel (intersection of the outer hull and the sphere) is obtained in FreeSurfer (*left*). The proposed kernel can be obtained with different regularization factors: isotropic ( $\eta = 1.0$ , *middle*) and anisotropic ( $\eta = 0.5$ , *right*) propagations. The FreeSurfer kernel has a circular shape on the outer hull, whereas the isotropic one does so on the cortical surface. The color indicates iso-contours over time.

## 5.8 Materials

In my experiments, pial cortical surfaces were created using the standard FreeSurfer pipeline [17]. The proposed method was evaluated on the left hemispheres at a fine sampling of 163,842 points (uniform sampling in spherical parameter space via icosahedron subdivision) and compared with FreeSurfer’s local gyrification index [110].

### 5.8.1 IBIS Living Phantom

The reproducibility of the proposed local gyrification index was evaluated on a large set of scan/rescan data. A human phantom (male, age 26 at the start of this study) was scanned at the four different imaging sites, equipped with a Siemens 3T Tim Trio scanner (Siemens, Erlangen, Germany) for evaluation, at irregular intervals over the period of 2.5 years. The same scanning sequences were employed for the developmental MRI scans; 36 scans were acquired in total.

### 5.8.2 KIRBY Dataset

The Kirby dataset of 21 healthy volunteers' scan/rescans already employed in Section 3 was also used here for reproducibility analysis [53], available on NITRC<sup>1</sup>. Scan-rescan imaging sessions with  $T_1$ -weighted scans were acquired using MP-RAGE sequence on the 21 subjects. To compute relative measurement errors, the average local gyrification index was used for each subject between the scan and rescan sessions. Refer to Section 3.6 for a detailed description.

### 5.8.3 Simulated Cortical Folding

Due to a high variability of the cortical folding, it would be computationally expensive and difficult to model every possible sulcal folding pattern and determine the kernel size that fully contains the sulcal fundus/gyral crown. For simplicity, I simulated such an ideal scenario for numerical validation, in which the gyral crowns are parallel to the sulcal fundi

---

<sup>1</sup><http://www.nitrc.org/>, Neuroimaging Informatics Tools and Resources Clearinghouse

and symmetric at the sulcal fundus.

**Parametric Simulated Model and Local Gyrfication Index** To create a simple cortical folding model, an implicit plane was rendered in the  $x$ - and  $y$ -parametric space in  $\mathbb{R}^2$  given by  $(x, y) \in [-\infty, \infty] \times [-0.75, 0.75]$ . Then a sine wave (amplitude =  $a/2$  and wavelength =  $1/2$ ) was applied over such a domain to obtain a sine waved plane  $F$ :

$$F(x, y) = \frac{a}{2} [-\cos(2\pi(2y + 1)) - 1]. \quad (5.11)$$

This gives three identical sulci having the same depth  $a$  (see Figure 5.5a). The magnitude of the middle sulcus  $y \in [-0.25, 0.25]$  was then modified, while fixing  $a = 1$  for the others to simulate two different scenarios: shallow ( $a = 0.5$ ) and deep ( $a = 2.0$ ) sulci. A line integral was performed along the sine wave to compute the ground-truth local gyrfication indices of shallow, deep, and neighboring sulci, respectively: 2.30, 8.11, and 4.19. The gyral/sulcal points were selected as the sources of the propagation by finding the extreme points of  $F$ . The propagation was then performed at the origin of the plane  $(0, 0, F(0, 0))$ .

**Travel-time of Simulated Symmetric Cortical Folding** Consider total travel-time from a sulcal fundus to its neighboring gyral crowns (see Figure 5.5a). The wavefront propagation thus begins at the sulcal fundus of  $\mathbf{x}$  such that  $T(\mathbf{x}) = 0$ . Let  $l$  be the length of its trajectory to the gyral crown with a linear parametrization of  $t \in [0, l]$ . This encodes that, for example,  $t = 0$  corresponds to the sulcal fundus and  $t = l$  to the gyral crown. From Equation 5.4, the travel-time along the gradient directions  $\mathbf{v}_1$  is obtained by the inverse of

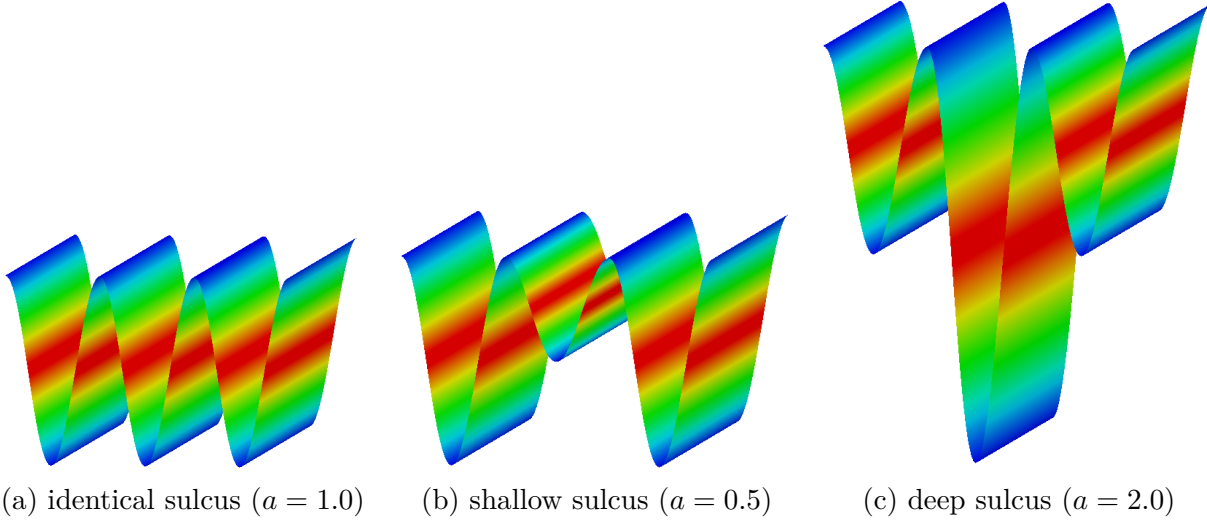


Figure 5.5: Simulated equally-spaced identical (a), shallow (b), and deep (c) sulci with their normalized travel-time maps: sulcal fundus/gyral crown (*blue*) or sulcal bank (*red*). The neighboring sulci are identical with the same depth ( $a = 1.0$ ). The sulcal/gyral regions are selected by finding extreme points as sources of the wavefront propagation. The travel-time map is normalized with respect to the spatial information over the cortical surface.

its speed:

$$\int_0^l \frac{1}{(1 - \eta)^{\frac{(l/2 - |t - l/2|)}{l/2}} + \eta} dt. \quad (5.12)$$

This is symmetric at  $t = l/2$ , which yields a closed form by simplifying the original formula in Equation 5.12.

$$\begin{aligned} & \int_0^{l/2} \frac{1}{(1 - \eta)^{\frac{t}{l/2}} + \eta} dt + \int_{l/2}^l \frac{1}{(1 - \eta)^{\frac{(l-t)}{l/2}} + \eta} dt \\ &= 2 \int_0^{l/2} \frac{1}{(1 - \eta)^{\frac{t}{l/2}} + \eta} dt = \int_0^1 \frac{l}{(1 - \eta)t + \eta} dt \\ &= -l \frac{\log \eta}{1 - \eta}. \end{aligned} \quad (5.13)$$

This implies the minimum travel-time to reach the neighboring gyral crowns. From Equation 5.13, as  $\eta$  decreases, it takes longer propagation time (proportional to  $-\log \eta / (1 - \eta)$ ) to reach two neighboring gyral crowns, whose resulting kernel spans more surface area. Figure 5.5 shows the two shallow and deep sulci generated by Equation 5.11.

## 5.9 Results

My proposed local gyrification index is determined by two parameters  $\eta$  (amount of anisotropy) and  $\rho$  (kernel size). In this section, I evaluated the behaviors of the proposed adaptive kernel by varying those parameters in several different settings. First, I show a reproducibility of the proposed kernel on the same subject with different MRI scans. Second, a comparison between different kernel shapes is made on the simulated folding. Finally, based on the above described experiments on both simulated and real dataset, I investigate an optimal parameter setting on a given population.

### 5.9.1 Reproducibility

The IBIS living phantom was used for the quantitative evaluation reproducibility without and with outer hull correspondence.

**Local Kernel Shape** The kernel reproducibility itself was evaluated without an inclusion of the outer hull correspondence. All the cortical surfaces were aligned via a generalized Procrustes alignment. Then a kernel with a fixed size on the pial surface was created and the average closest distance was measured for every possible pair (36 different scans = total  $36 \times 35$  combinations) of the acquired kernel boundaries at the corresponding locations from different scans. Such extensive comparisons were made because no ground truth of boundary correspondence is available and the metrics are asymmetric (one-sided) in general. I varied the kernel size from 316 to 1,264  $mm^2$  with an interval of 316  $mm^2$  as well as  $\eta$  at 1.0, 0.5, 0.2, and 0.1. The average closest distance over the entire cortex are summarized in Table 5.1.

Area ( $mm^2$ )	316	632	948	1,264
$\eta = 1.0$	$0.56 \pm 0.19$	$0.66 \pm 0.22$	$0.72 \pm 0.23$	$0.76 \pm 0.24$
$\eta = 0.5$	$0.65 \pm 0.21$	$0.78 \pm 0.24$	$0.85 \pm 0.25$	$0.91 \pm 0.26$
$\eta = 0.2$	$0.71 \pm 0.23$	$0.85 \pm 0.26$	$0.94 \pm 0.28$	$1.01 \pm 0.29$
$\eta = 0.1$	$0.73 \pm 0.24$	$0.88 \pm 0.27$	$0.97 \pm 0.29$	$1.04 \pm 0.30$

Table 5.1: Average closest distance of the adaptive kernel between all pairs of surfaces of the same subject (unit:  $mm$ ). The proposed adaptive kernel achieves a great reliability even for large area with high anisotropy in terms of triangulated size, given that the average edge length is  $1.16 \pm 0.46 mm$ .

The result reveals that the boundaries of the corresponding kernels were almost completely overlapped as measured by the average closest distance that differs less than a single triangle edge on average. This is partially due to utilizing the discrete wavefront propagation whose boundary stops at a discrete vertex on the triangulated surface. In terms of the triangulated quality of the pial surface (average edge length:  $1.16 \pm 0.46 mm$ ), however, this implies that the proposed approach is able to achieve an excellent reproducibility in computing the proposed adaptive kernel even at a high anisotropic speed  $\eta = 0.1$ . Note that the adaptive kernel is getting more sensitive to the sulcal/gyral curve extraction method as  $\eta$  decreases and thus that the average closest distance increases while the resulting reproducibility decreases.

**Local Gyrfication Index** The local gyrfication index was computed using the conventional FreeSurfer method [110] and the proposed adaptive kernel for the comparison purpose. The kernel area on the outer hull  $\rho$  varies from 316 to 1,264  $mm^2$  with an interval of 316  $mm^2$  for  $\eta = 1.0, 0.5, 0.2,$  and  $0.1$ . Since the local gyrfication index is unitless, a coefficient of variation (CoV) was used to measure the percentage of its measurement error that quantifies how local gyrfication indices vary across multiple scans. Figure 5.6 illustrates the reproducibility over the entire surface for the conventional and proposed methods. Although

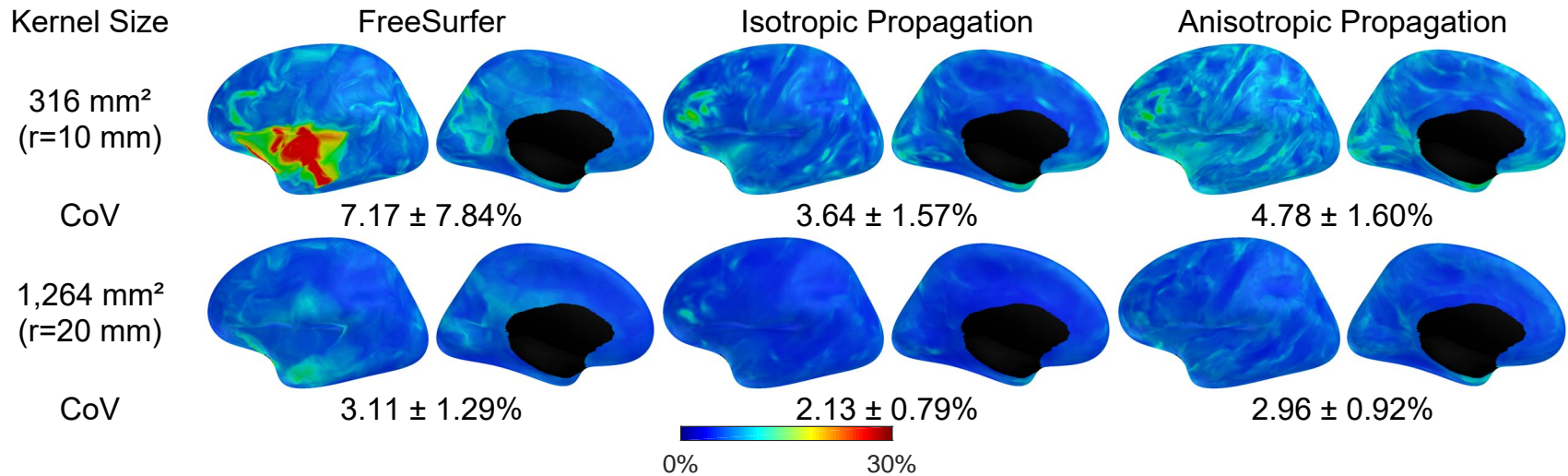


Figure 5.6: Reproducibility of the conventional and proposed method. The reproducibility is measured by coefficient of variation (CoV). Overall, the proposed kernel-based local gyrification index achieves a better reproducibility than the conventional method for both small and large sized kernels. The proposed kernel shows better performance as it gets isotropic due to a less influence of sulcal/gyral patterns that might further introduce curve extraction errors in measurement. The inflated surface is used for better visualization (*blue - red*): 0-30%.

Area ( $mm^2$ )	316	632	948	1,264
Radius ( $mm$ )	10	14	17	20
FreeSurfer	$7.17 \pm 7.84$	$4.87 \pm 2.12$	$3.93 \pm 1.65$	$3.11 \pm 1.29$
$\eta = 1.0$	$3.64 \pm 1.57$	$2.67 \pm 1.05$	$2.31 \pm 0.89$	$2.13 \pm 0.79$
$\eta = 0.5$	$4.16 \pm 1.49$	$3.18 \pm 1.04$	$2.76 \pm 0.88$	$2.52 \pm 0.80$
$\eta = 0.2$	$4.78 \pm 1.60$	$3.74 \pm 1.17$	$3.26 \pm 1.00$	$2.96 \pm 0.92$
$\eta = 0.1$	$5.21 \pm 1.79$	$4.13 \pm 1.38$	$3.61 \pm 1.19$	$3.28 \pm 1.09$

Table 5.2: Coefficient of variation of the local gyrification index (unit: %). Overall, the proposed method achieves a better reliability than the conventional method (FreeSurfer). The proposed local gyrification index exhibited a slightly lower (but still comparable) reproducibility in the anisotropic propagation due to the sulcal/gyral curve extraction.

the reproducibility might be influenced by the surface correspondence  $f$ , the proposed local gyrification index achieved a comparable reproducibility to the conventional method for both the isotropic and anisotropic propagation. For the small kernel size ( $316 mm^2$ ), the conventional method was unstable (as expected) around the Sylvian fissure likely due to its deeply buried sheet, whereas the proposed kernel provided a consistently high reproducibility even in that area. Note that the isotropic propagation should be considered as a lower bound of the proposed method as it does not take into account the sulcal/gyral curves for the local gyrification index computation. Table 5.2 summarizes the average coefficient of variation of the local gyrification index over the entire cortex at different anisotropic speed  $\eta$ . As expected, the local gyrification index achieved a slightly lower (but still comparable) reproducibility when using anisotropic propagation due to being more sensitive to the variability in the sulcal/gyral curve extraction.

### 5.9.2 Evaluation of Simulated Cortical Folding

To examine how my local gyrification index varies over  $\eta$ , I generated the cortical folding via the simulation with an areal interval proportional to the standardized propagation area,

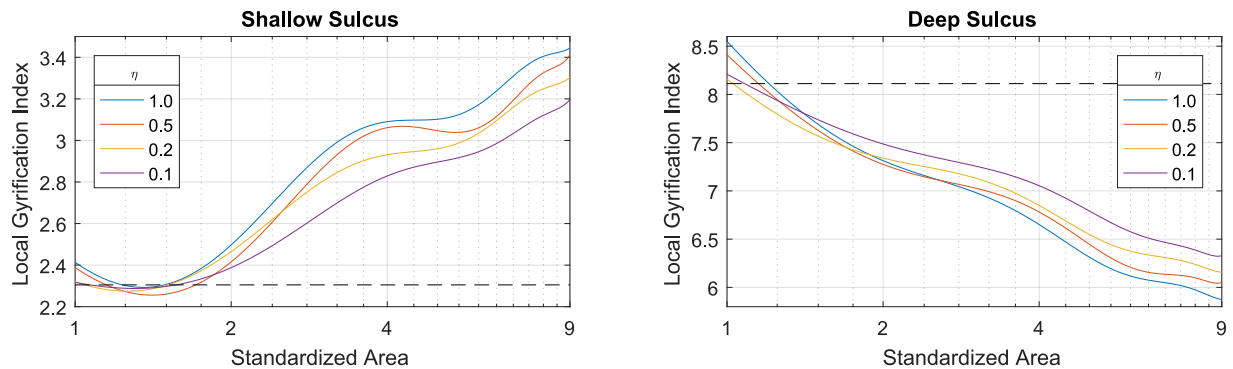


Figure 5.7: Local gyrification index of the sine waved plane in two different simulated scenarios: shallower ( $a = 0.5$ ) and deeper ( $a = 2$ ) sulci than the neighboring ones ( $a = 1$ ) (see Figure 5.5). Ground truth values for both scenarios are shown by *dashed line*. The local gyrification indices are assessed on the two simulated sulcal depths. When the proposed kernel touches two gyral crowns (area = 1), it gets closer to the ground truth as  $\eta$  decreases (higher anisotropic speed) along the sulcal fundus. *Left*: Since the two neighboring sulcal fundi are deeper ( $a = 1$ ) than the sulcus being evaluated, the gyrification index increases as the propagation covers more area of the neighboring fundi. *Right*: The gyrification index constantly decreases as the depth of the neighboring sulcal fundi is shallower ( $a = 1$ ) than the sulcus being evaluated.

in which the kernel touches the two neighboring gyral crowns. In Figure 5.7, the local gyrification index is getting closer to the ground truth as  $\eta$  decreases due to its increasing anisotropic speed along the sulcal fundus. I further increased the kernel size until it almost fully covers the two neighboring sulcal fundi. The local gyrification index was decreasing as the neighboring sulcal fundi increasingly influenced the local gyrification index. For both shallow and deep sulci, the local gyrification index changes slowly as  $\eta$  decreases. This implies that the anisotropic propagation computed the local gyrification index in a more accurate cortical-shape-adaptive way than the isotropic propagation.

### 5.9.3 A Choice of Kernel Size

It is important to cover sulcal/gyral regions completely to capture sulcal folding appropriately. For this purpose, the minimum kernel size was computed for a given subject population. It is noteworthy that the outer hull squeezes the sulcal regions while leaving the

gyral crown with subtle distortion because a correspondence to the outer hull is obtained by the Laplace-based surface evolution. Thus, I focused on fixing the outer hull area  $A_H$  corresponding to sulcal fundi. To determine the minimum kernel size that fully spans a sulcal region (i.e., at least two gyral crowns),  $A_H$  was computed for  $\forall \mathbf{x} \in \Omega$  belonging to the sulcal curves. Since the cortical area is different across the subjects, the kernel size was normalized with the average total cortical surface area over the population to remove the impact of differently sized surfaces.

Using the Kirby dataset, I computed the average local gyrification index for each subject between the scan and rescan sessions. Since there is a trade-off between reproducibility and measurement accuracy,  $\eta$  was set to 0.2 to more adaptively capture cortical folding, while keeping a comparable reproducibility to the conventional method. I also chose  $\rho = 316.66 \text{ mm}^2$  over the population to guarantee the kernel size that completely covers any sulcus in this subject population. Figure 5.8 shows local gyrification indices using different kernel sizes. The proposed kernel more adaptively captured the cortical folding especially using a small kernel size. Despite a high blurring effect with a large kernel, the proposed adaptive kernel provided comparable local gyrification indices over the entire cortex as can be well seen by the detailed gyrification index at the central or cingulate sulcus, for example.

## 5.10 Methodological Issues

### 5.10.1 Local Gyrification Index

Several metrics have been proposed to measure local cortical gyrification. The most prevalent ways are based on an area ratio of the pial surface over the reference model (e.g.,

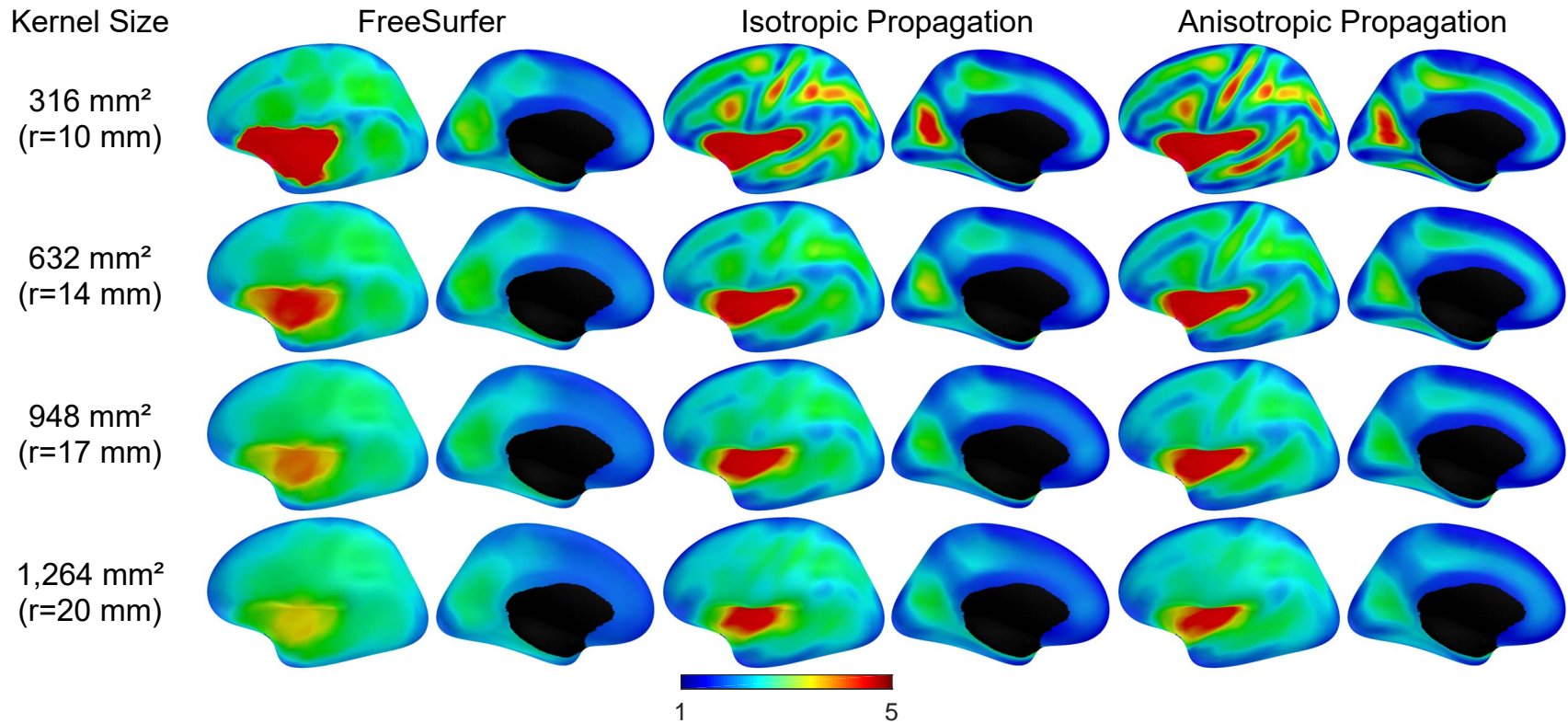


Figure 5.8: The average local gyrification indices on the Kirby dataset in the lateral and medial views. The sulcal folding patterns are well captured by the isotropic (*middle*) and anisotropic (*right*) kernels. The sulcal fundi/gyral crowns are more adaptively captured in the anisotropic kernel, whereas several folding patterns (e.g., precentral gyrus or superior temporal sulcus) are smoothed out in the isotropic kernel at proposed local size (*top*). Even with a large kernel, the folding patterns are better revealed by the anisotropic kernel than by that of FreeSurfer or the isotropic kernel (*bottom*). The inflated surface is used for better visualization. The area of 1,264 mm<sup>2</sup> corresponds to approximately a circle with a radius of 20 mm, which is a typical size of the kernel used in the FreeSurfer method.

outer hull). Depending on the metric definition, the denominator could be either the reference model or the pial surface. Lebed *et al.* [56] used an area ratio reciprocal to the one used in [110], for instance, so that a constant kernel over the pial surface captures cortical folding more uniformly. However, considering cortical folding evolution, it is more plausible that the amount of cortical folding is measured from the outer hull as proposed in [110]. A main challenge in these conventional approaches was to find a proper kernel size to cover at least a single sulcus. They used a large kernel to guarantee a complete coverage of deeply buried sulcal fundi such as the Sylvian fissure [110] with corresponding loss of sensitivity or just used a small kernel [56] that cannot sufficiently cover a highly variable sulcus. Neither methods capture the folding patterns appropriately across the entire cortical surface.

By improving the conventional approaches, the proposed adaptive kernel provides an improved sensitivity while appropriately capturing differently sized cortical folding regions. The main difference to the conventional approaches is based on the wavefront propagation over the pial surface and the Laplace-based correspondence between pial surface and outer hull. In the conventional method [110], local cortical folding is hard to be captured since the kernel was determined only on the outer hull. Even with a kernel defined on the pial surface like [56], a large kernel might be needed to span a deeply buried sulcus. In my method, the adaptive kernel size is determined by fixing the corresponding area to the outer hull while the wavefront propagation is performed over the pial surface to capture a local cortical shape. Thanks to the Laplace-based correspondence between the pial surface and the outer hull, the cortical folding is represented in a more consistent way regardless of sulcal depth, as the contribution of the sulcal fundus is relatively small to its neighboring gyral regions in computing the corresponding outer hull area. This consequently enables the computation of

a local gyrification index along sulcal fundic regions with the anisotropic kernel, providing a more localized measurement as shown in Figure 5.8. Furthermore, compared to the isotropic propagation, the local gyrification index can be refined along sulcal fundi/gyral crowns via the proposed anisotropic propagation. For instance, in contrast to the anisotropic propagation, Figure 5.8 shows that the isotropic propagation produces the discontinued local gyrification indices at the gyral junction between central and middle frontal gyrus. Also, the anisotropic propagation better quantifies the average gyrification indices along the cingulate sulcus even with a large kernel size.

### 5.10.2 Cortical-Shape-Adaptive Kernel

My shape-adaptive kernel can be defined anywhere on the cortex, so it does not require any particular interpolation scheme to assign a local gyrification index for a given location in contrast to [110, 77]. There are two major issues in the proposed kernel creation, though, related to a parameter choice: the amount of anisotropy and the kernel size. As shown in my experiments, there is a trade-off between sensitivity and reproducibility in the amount of anisotropy. In terms of sensitivity, cortical folding is better quantified with a higher anisotropic speed, which adaptively captures cortical folding along the sulcal fundus/gyral crown. In contrast, a higher anisotropic speed is more influenced by the quality of the sulcal/gyral curve extraction, as these curves are the sources of the wavefront propagation, although it maintains a reproducibility comparable to the conventional method. Note that the conventional method evaluates its local gyrification index within a spherical region that is not of exactly the same circular area at the corresponding location as the authors pointed out in [110]; the intersected area of the outer hull is usually larger than the corresponding circular area. This leads to a

higher blurring effect on the measurements with loss of sensitivity. I provided a suggested anisotropic speed based on the experiment, yet depending on the application, the user can choose alternative parameters to leverage sensitivity and reproducibility.

Another issue is to find the proper kernel size. A large sized kernel tends to smooth out cortical folding patterns as already shown in several studies. In this chapter, for the local gyrification index computation I used the minimal kernel size that completely covers any of the sulcal fundic region. In the Kirby dataset, the kernel size at sulcal points was one sixth of the minimal kernel size on average. The experimental results also revealed that such a blurring effect is getting emphasized as the anisotropic speed becomes isotropic. In the present studies, that effect is rarely avoidable as long as the kernel size is fixed across the entire surface due to the variable nature of the cortical folding. With an incorporation of the anisotropic wavefront propagation, the blurring effect can be reduced by minimizing the influences of the neighboring sulci though. It would be interesting to see if an optimal kernel size can be adaptively determined based on its neighborhood. One way to do so would be to use the spatial information of sulci and gyri where the adaptive kernel size can be computed based on neighboring gyral/sulcal curves, similar to [77]. Though this approach looks promising, the adaptive kernel size might need to be justified at any point rather than just at sulcal/gyral locations.

### **5.10.3 Computation Issues**

There are several computation issues with the proposed adaptive kernel. Although sulcal/gyral curves were employed as the source of the anisotropic propagation, other information could be used for the travel-time computation as the proposed approach is versatile. One

can also incorporate sulcal depth or local curvature as potential candidate sources for the travel-time map computation for example. The processing was performed over the discretized surface model from which numerical errors arise. In the cortical surface model, the average errors in the reproducibility were less than the average edge length ( $1.16 \pm 0.46 \text{ mm}$ ), which was acceptable also relative to the MR image resolution ( $1 \text{ mm}$ ). However, this error could be reduced by further approximation of the wavefront propagation at each triangle using a barycentric (or other interpolation) technique, which would result in more stable and reliable measurements.

### 5.11 Summary

In this chapter, I proposed a local gyrification index using a novel shape-adaptive kernel computed via wavefront propagation over the cortical surface. Unlike a simple geodesic/nearest neighboring ring-based kernel, the proposed kernel is adaptively elongated along the cortical geometry. The proposed kernel is well formulated by the H-J PDE with a sufficient condition that guarantees a unique viscosity solution to this specific problem. Sulcal/gyral curves serve as the source of the wavefront propagation to create a travel-time map. The proposed kernel is then guided over the gradient field computed by the travel-time map.

The experimental results have shown that the proposed kernel a) achieves a high reproducibility even at highly anisotropic kernels, b) shows minimally a comparable reproducibility of the local gyrification index to the conventional method, and c) in my simulation produces a local gyrification index close to the ground truth in both shallow and deep sulci. For high shape adaptiveness and reproducibility, I also proposed a proper kernel size based on the observation of the anisotropic propagation with a reproducibility comparable to the

conventional method. The results showed that the proposed kernel adaptively captures local folding patterns in the scan-rescan human dataset for both small and large kernel sizes.

## CHAPTER 6: CORTICAL MORPHOMETRY AND COGNITIVE DEVELOPMENT IN EARLY POSTNATAL STAGE

### 6.1 Overview

In recent years an increasing number of studies have focused on cognitive development or cortical gyrification in the early postnatal phase starting at neonate to 2 years of age. However, to the best of my knowledge, no present study has yet revealed the association between cognition development and cortical gyrification. In this chapter, I focus on employing my local gyrification index to reveal its relationship with cognitive development as quantified via cognitive associations. Section 6.3 describes the UNC Early Brain Development Study (EBDS) dataset and the exclusion procedure used in this study. Section 6.4 presents the statistical models used in this study, and Section 6.5 provides its findings.

### 6.2 Objective

The objective of this chapter is to investigate the relationship of cortical folding and cognitive development. I investigate the following hypotheses:

1. Cortical gyrification dramatically changes in early postnatal development at spatially ranging growth ratio.
2. There is a significant association between local cortical gyrification and cognitive development.

3. My proposed gyrification index reveals novel patterns of association in more sulcal specific regions than existing methods [36].

### 6.3 The UNC Early Brain Development Studies (EBDS)

This section briefly describes the EBDS dataset<sup>1</sup> administered at the University of North Carolina at Chapel Hill under the principal investigator, Dr. Gilmore.

#### 6.3.1 MR Image Acquisition

Subjects were part of large prospective studies of EBDS in healthy singletons and twins [36, 50, 37, 38]. Subjects were recruited prenatally and scanned shortly after birth, at age 1 year, and at age 2 years with cognitive assessment also at age 1 and 2 years. MR Images were acquired on both a Siemens Allegra and a Siemens Timm Trio head-only 3T scanner (Siemens Medical Systems, Erlangen, Germany). Children were scanned un sedated while asleep, fitted with ear protection and with their heads secured in a vacuum-fixation device.  $T_1$ -weighted structural pulse sequences were a 3D MP-RAGE (TR = 1,820 ms, inversion time = 1,100 ms, TE = 4.38 ms, flip angle = 7°, resolution = 1 mm × 1 mm × 1 mm). Proton density and  $T_2$ -weighted images were obtained with a TSE sequence (TR = 6,200 ms, TE1 = 20 ms, TE2 = 119 ms, flip angle = 150°, resolution = 1.25 mm × 1.25 mm × 1.95 mm). For neonates who were deemed likely to fail due to difficulty sleeping, a fast  $T_2$  sequence was done with a 15% decreased TR, smaller image matrix and fewer slices (5,270

---

<sup>1</sup>The Institutional Review Board of the University of North Carolina at Chapel Hill approved this study.

*ms*, 104 mm × 256 mm, 50 slices).

### 6.3.2 Mullen Scales of Early Learning (MSEL)

The Mullen Scales of Early Learning [86] test is administered at the 1 and 2 years visits in this study. It consists of the following measurement scales thought to be involved in the corresponding cortical regions.

- The gross motor (GM) and fine motor (FM) measures evaluate postural and limb control, bimanual manipulation, and fine motor movements related to the following regions: primary motor cortex, premotor cortex, frontal lobe.
- The expressive language (EL) and receptive language (RL) measures evaluate language processing and production related to the following regions: Broca's area, Wernicke's area, Geschwind's area, middle temporal lobe.
- The visual reception (VR) measure evaluates visual discrimination, memory, sequencing, spatial awareness related to the following regions: visual cortex, occipital lobe, fusiform gyrus, orbital frontal cortex, precuneus lobe, parietal lobe.
- The early learning composite score (ELC = FM + EL + RL + VR) evaluates general cognition related to the following regions: frontal lobe, parietal lobe, visual cortex, cingulate cortex, precuneus lobe.

Mullen scale *t*-scores ( $\mu = 50$ ,  $\sigma = 10$ , range=20-80) and scaled scores ( $\mu = 100$ ,  $\sigma = 15$ , range=49-155) are standardized with a nationally representative sample of 1,849 children (roughly 50% male). The MSEL has high internal consistency (median: 0.83) and reliability (median: 0.91).

### 6.3.3 Data Exclusion Criteria

Subjects assessed via MSEL at 1 and 2 years of age were excluded if they met at least one of the following conditions: 1) gestational age at birth less than 32 weeks, 2) the length of stay in the neonatal intensive care unit for greater than 1 day, 3) abnormality on MRI other than a minor intracranial hemorrhage, common in the neonatal period [66], 4) major medical or neurologic illness after birth, 5) ELC score of  $< 71$ , or 6) high genetic risks for schizophrenia and bipolar illness. In the EBDS dataset about 30% of the entire population is at familial risk, as these subjects were specifically recruited as part of EBDS. In this study I only considered singleton subjects. Table 6.1 summarizes the final dataset that meets the above criteria, the one used in this study. Figure 6.1 illustrates the Pearson’s correlation coefficients of every possible pair of the MSEL categories in my study. The ELC not surprisingly shows strong correlations with other MSEL scores except GM, as ELC is composed of the other categories except GM.

### 6.3.4 Surface Model Reconstruction and Local Gyrfication Index

The surface models were reconstructed via the FreeSurfer pipeline and were resampled at 163,842 vertices via a standard icosahedron subdivision. The surface correspondence was established using my group-wise method described in Chapter 4. Due to the large number of the subjects in this study, I employed the proposed subgroup division scheme described in Chapter 4, in which a surface correspondence for each subgroup with 20 subjects was established. To quantify cortical gyrfication, the local gyrfication index was computed within the cortical-shape-adaptive kernel described in Chapter 5. Since the cortical surface area dramatically changes over ages, I further regularized the kernel size based on two observations.

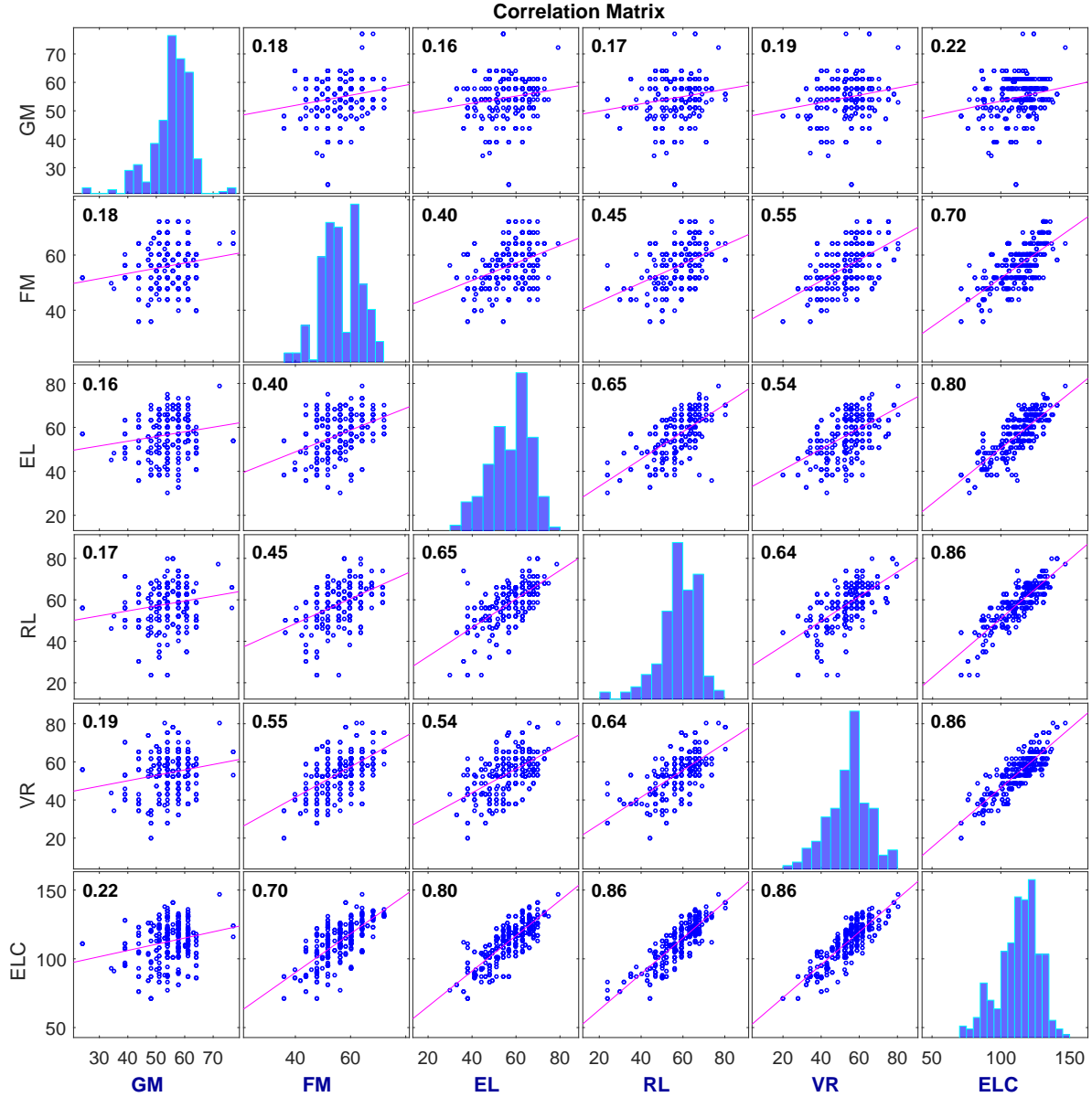


Figure 6.1: The Pearson’s correlation coefficients of MSEL scores of the EBDS dataset. Every pair of the scores has a positive correlation ( $p < 0.005$ ). The ELC forms strong correlations with other categories except GM, whereas GM has relatively low correlations.

First, the experimental results in Chapter 5 revealed that the minimum kernel size fully spanning all the sulcal regions on the adult outer surface was roughly  $316 \text{ mm}^2$ . Second, in the EBDS dataset the average cortical surface areas at neonate, 1 year, and 2 year have respective scaling factors of 0.36, 0.6, 0.66 compared to an average adult cortical surface area,

Scans	Total number	Male	Female	Age (days)	Age range	Gestational age (days)
Neonate	178	88	90	$20.89 \pm 9.50$	6-68	$275.27 \pm 11.29$
1 year	85	44	41	$385.27 \pm 22.84$	343-481	$273.36 \pm 11.86$
2 years	76	44	32	$746.54 \pm 25.03$	693-827	$272.62 \pm 14.04$
Total	339	176	163	-	-	$274.20 \pm 12.12$
Scans	GM	FM	EL	RL	VR	ELC
Neonate	$54.76 \pm 6.71$	$55.84 \pm 6.83$	$57.14 \pm 9.56$	$58.53 \pm 9.32$	$54.44 \pm 9.82$	$112.99 \pm 13.88$
1 year	$55.32 \pm 6.92$	$56.64 \pm 8.01$	$57.31 \pm 8.73$	$58.26 \pm 9.32$	$54.31 \pm 11.24$	$113.31 \pm 15.23$
2 years	$54.17 \pm 7.73$	$56.13 \pm 7.19$	$55.67 \pm 8.15$	$57.16 \pm 10.20$	$53.89 \pm 10.98$	$111.49 \pm 15.01$
Total	$54.77 \pm 7.01$	$56.11 \pm 7.23$	$56.85 \pm 9.08$	$58.15 \pm 9.54$	$54.28 \pm 10.46$	$112.73 \pm 14.50$

Table 6.1: Early brain development studies (EBDS) dataset with population statistics and the 6 MSEL scores

respectively. In order to take into account the inter-subject variability in cortical surface area, I adaptively rescaled the kernel size for each subject according to the corresponding age group. Specifically, for both left and right hemispheres, the average kernel size was  $108 \text{ mm}^2$  ( $r \approx 5.9 \text{ mm}$ ),  $180 \text{ mm}^2$  ( $r \approx 5.9 \text{ mm}$ ),  $200 \text{ mm}^2$  ( $r \approx 8.0 \text{ mm}$ ) for neonate, 1 year and 2 years, respectively.

#### 6.4 Linear Mixed Model for the Longitudinal Study

I designed longitudinal linear mixed models to investigate the association between cortical morphological change (local gyrification change) and cognitive development in early childhood. The local gyrification index was used as a dependent variable  $Y$ , and the fixed effects were composed of 9 covariates: postnatal age at scan, gender, gestational age at birth, and 6 categories of MSEL. I only considered MSEL measured at 2 years old as fixed effects. The effects were tested via a longitudinal mixed model developed in SurfStat<sup>2</sup>. For each subject  $i$ , the following linear mixed models were fitted to my data, with  $U_i$  capturing estimates for the subject-specific random effects.

$$Y_i = \beta_0 + \beta_{\text{Age}}\text{Age}_i + \beta_{\text{Gender}}\text{Gender}_i + \beta_{\text{Gest}}\text{Gest}_i + U_i + \varepsilon_i, \quad (6.1)$$

$$Y_i = \beta_0 + \beta_{\text{Age}}\text{Age}_i + \beta_{\text{Gender}}\text{Gender}_i + \beta_{\text{Gest}}\text{Gest}_i + \beta_{\text{GM}}\text{GM}_i + U_i + \varepsilon_i, \quad (6.2)$$

$$Y_i = \beta_0 + \beta_{\text{Age}}\text{Age}_i + \beta_{\text{Gender}}\text{Gender}_i + \beta_{\text{Gest}}\text{Gest}_i + \beta_{\text{FM}}\text{FM}_i + U_i + \varepsilon_i, \quad (6.3)$$

---

<sup>2</sup>SurfStat is a MATLAB toolbox for statistical analysis of cortical surface data employing random field theory for statistical inference [139], publicly available at <http://www.stat.uchicago.edu/faculty/InMemoriam/worsley/research/surfstat/index.htm>

$$Y_i = \beta_0 + \beta_{\text{Age}}\text{Age}_i + \beta_{\text{Gender}}\text{Gender}_i + \beta_{\text{Gest}}\text{Gest}_i + \beta_{\text{EL}}\text{EL}_i + U_i + \varepsilon_i, \quad (6.4)$$

$$Y_i = \beta_0 + \beta_{\text{Age}}\text{Age}_i + \beta_{\text{Gender}}\text{Gender}_i + \beta_{\text{Gest}}\text{Gest}_i + \beta_{\text{RL}}\text{RL}_i + U_i + \varepsilon_i, \quad (6.5)$$

$$Y_i = \beta_0 + \beta_{\text{Age}}\text{Age}_i + \beta_{\text{Gender}}\text{Gender}_i + \beta_{\text{Gest}}\text{Gest}_i + \beta_{\text{VR}}\text{VR}_i + U_i + \varepsilon_i, \quad (6.6)$$

$$Y_i = \beta_0 + \beta_{\text{Age}}\text{Age}_i + \beta_{\text{Gender}}\text{Gender}_i + \beta_{\text{Gest}}\text{Gest}_i + \beta_{\text{ELC}}\text{ELC}_i + U_i + \varepsilon_i, \quad (6.7)$$

where  $\varepsilon_i$  is an error term. In my experiment, standard false discovery rate (FDR) correction was applied to correct for the multiple comparisons for models in Equation 6.1 [6]. Since each surface model is composed of the large number of vertices ( $= 163,842$ ), I employed an ROI-based correction using a pre-labeled parcellation (76 regions for each hemisphere) [23] for the models (Equation 6.2 to Equation 6.7). In this ROI correction, rather than testing all vertices independently, for each region the maximum  $t$ -value was selected and employed as the representative statistical measurement of that region. Figure 6.2 illustrates the correlation of gyrification index within subject across time revealed in the linear mixed model. Most gyral regions and the frontal lobe show a high correlation, whereas several sulcal regions show a low (or nearly zero) correlation especially in deep sulcal regions such as central sulcus. Due to the highly correlated regions, subject-specific random effects need to be considered in the linear mixed model.

## 6.5 Findings of Early Morphometry and Cognitive Development

### 6.5.1 Cortical Gyrification in Early Stage

As expected, statistical analysis showed that local gyrification is highly associated with age as visualized in Figure 6.3. Most cortical regions have a positive change rate of cortical

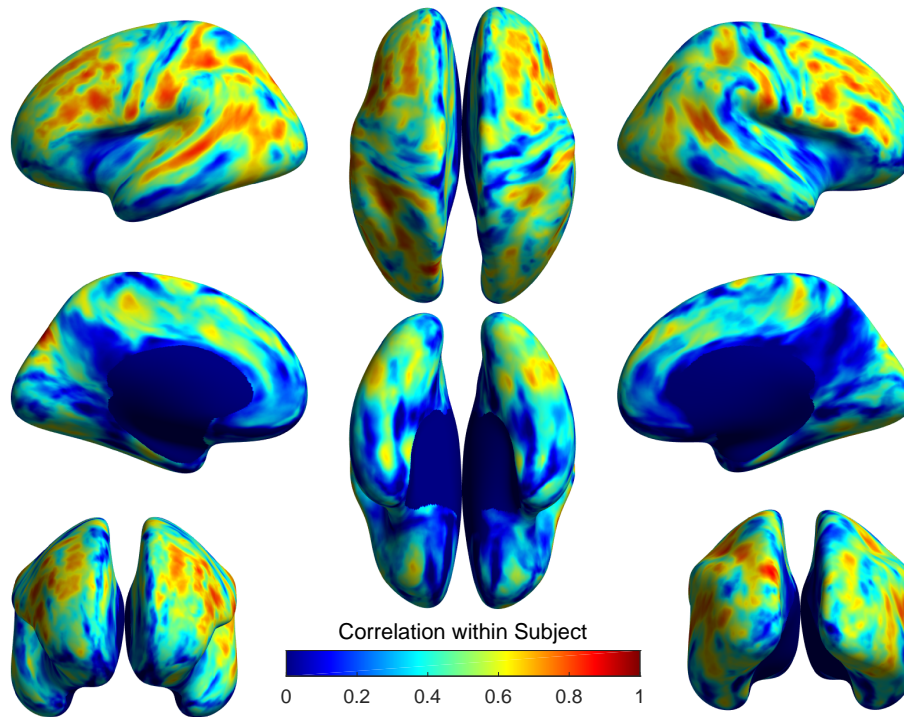


Figure 6.2: The correlation of gyrification index within subject. The linear mixed model reveals a high correlation mostly in the gyral regions and the frontal lobe, compared with several sulcal regions such as central sulcus.

folding, whereas the deep sulcal regions such as central and cingulate sulci have almost zero (and even negative) change rates. It is likely due to different growth rates across cortex such as the myelination process [59] that 1) such deep cortical folding is nearly full at an early postnatal age, whereas 2) the width between gyral crowns increases. This yields that the gyrification index is getting smaller in those sulcal regions. For the gender effect, male subjects show persistently higher local gyrification in the visual cortex and right pre-central sulcal region, whereas female subjects show higher gyrification in superior temporal, right inferior frontal lobe, and parieto-occipital sulcal regions, as shown in Figure 6.4. As only few studies have focused on the gender effect of cortical gyrification in the early childhood ages, gender

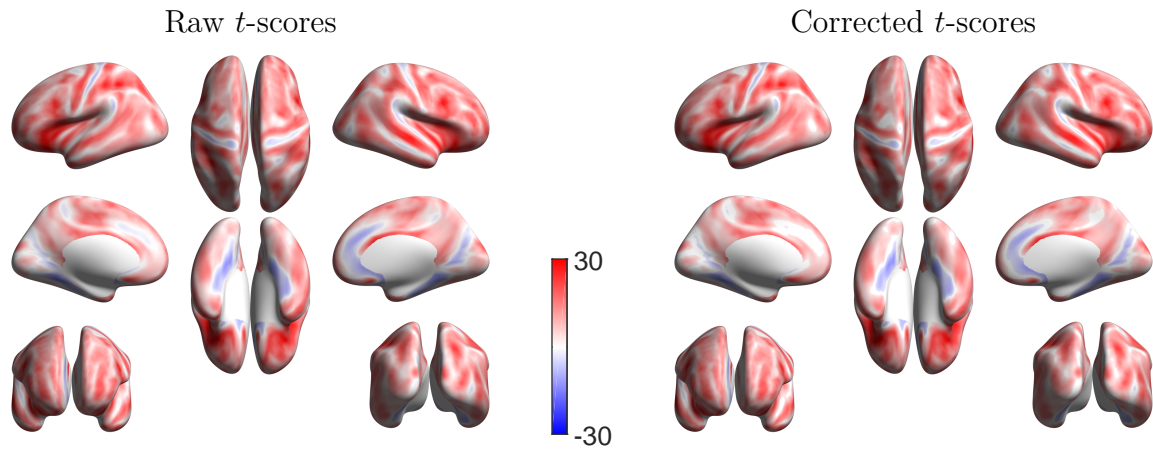


Figure 6.3: The age effect on cortical gyrification. Most cortical regions have positive association of cortical gyrification over ages with  $t$ -value maps before (*left*) and after (*right*) correction ( $q < 0.05$ ). Deep sulcal regions such as central and cingulate sulci have negative association since they are well developed during the gestational period.

differences of developmental trajectories still remain largely unclear in the early postnatal phase. Despite the lack of findings, the results in Figure 6.4 are somewhat comparable to the few previous studies [62, 49]. Specifically, Li et al. [62] argued that the local gyrification index increases across the entire cortical regions over ages. In this study I found similar results with their study but also my refined analysis revealed several regions, such as the central motor and cingulate sulci, that show negative association in the early postnatal phase. The main reasons for differences between my study and Li et al. [62] are 1) the sulcal-folding-adaptive quantification and 2) more localized analysis with the smaller kernel size. For the gestational age effect at birth, the cortical gyrification changes asymmetrically in the left and right hemispheres as illustrated in Figure 6.5. Overall, a positive association with the gestational age is revealed over most cortical regions while showing a negative association in the primary motor cortex and collateral fissure.

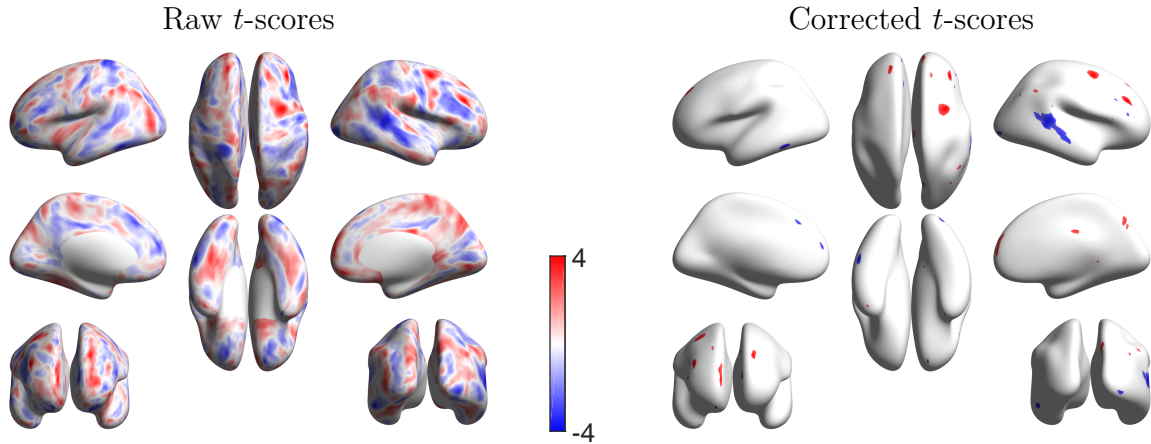


Figure 6.4: The gender effect (red: male, blue: female) on cortical gyrification with  $t$ -value maps before (*left*) and after (*right*) correction ( $q < 0.05$ ). Most cortical regions have positive association of cortical gyrification over ages. The female subjects show higher gyrification in the right superior temporal lobe, whereas the male subjects show higher development in primary motor.

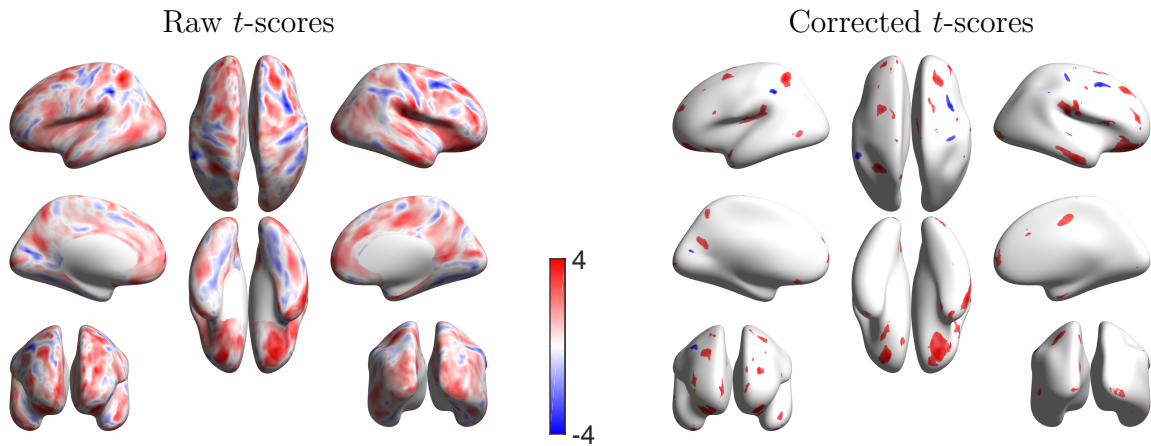


Figure 6.5: The gestational age effect at birth on cortical gyrification with  $t$ -value maps before (*left*) and after (*right*) correction ( $q < 0.05$ ). Most cortical regions have positive association of cortical gyrification over ages (uncorrected  $p$ -values).

### 6.5.2 Association of Cognitive Development

Next, I discuss the association of cortical morphological changes with cognitive development in the early postnatal phases. Visually, Figure 6.1 illustrates the  $t$ -value map of ELC is quite similar to that of other categories except GM, as expected. Mostly, the sulcal regions show a negative association with cognitive development in contrast to the gyral regions that have

positive association (see Figure 6.6 for raw  $t$ -values and Figure 6.7 for  $t$ -values after multiple comparison correction). As hypothesized, specific significant associations with functionally well-known regions (Section 6.3.2). For motor development, there was a negative association in the left and right primary motor and premotor cortices, whereas other regions show a positive association such as the left parieto-occipital sulcus. For language development, positive association was observed in parts of Broca’s area. For visual perception, the left visual cortex in the medial side has positive association with local gyrification index, whereas the parietal sulcus has negative association. There were several regions with positive and negative association in ELC: right frontal lobe, left fusiform gyrus, and left visual cortex.

Surprisingly, the association patterns of local gyrification change with age and cognitive development. Even though most regions show a positive correlation of local gyrification over ages shown in Figure 6.3, their associations with cognitive development possess a different pattern (Figure 6.8). For example, the precentral gyrus shows a positive correlation with age, whereas it shows a negative correlation with ELC, i.e., the smaller local gyrification index, the higher ELC score.

### 6.5.3 Comparisons with FreeSurfer

The ability of the local gyrification index to reveal statically significant regions is a key feature in a population analysis. In this section, I computed the local gyrification index using my method proposed in Chapter 5 and FreeSurfer [110]. The same kernel size of  $800\text{ mm}^2$  ( $r \approx 16\text{ mm}$ ) was employed for fair comparisons of age effects (see Figure 6.9) and cognitive scores of MSEL (see Figure 6.10). The experiment revealed that the proposed local gyrification index achieves more refined results than FreeSurfer, as the proposed index

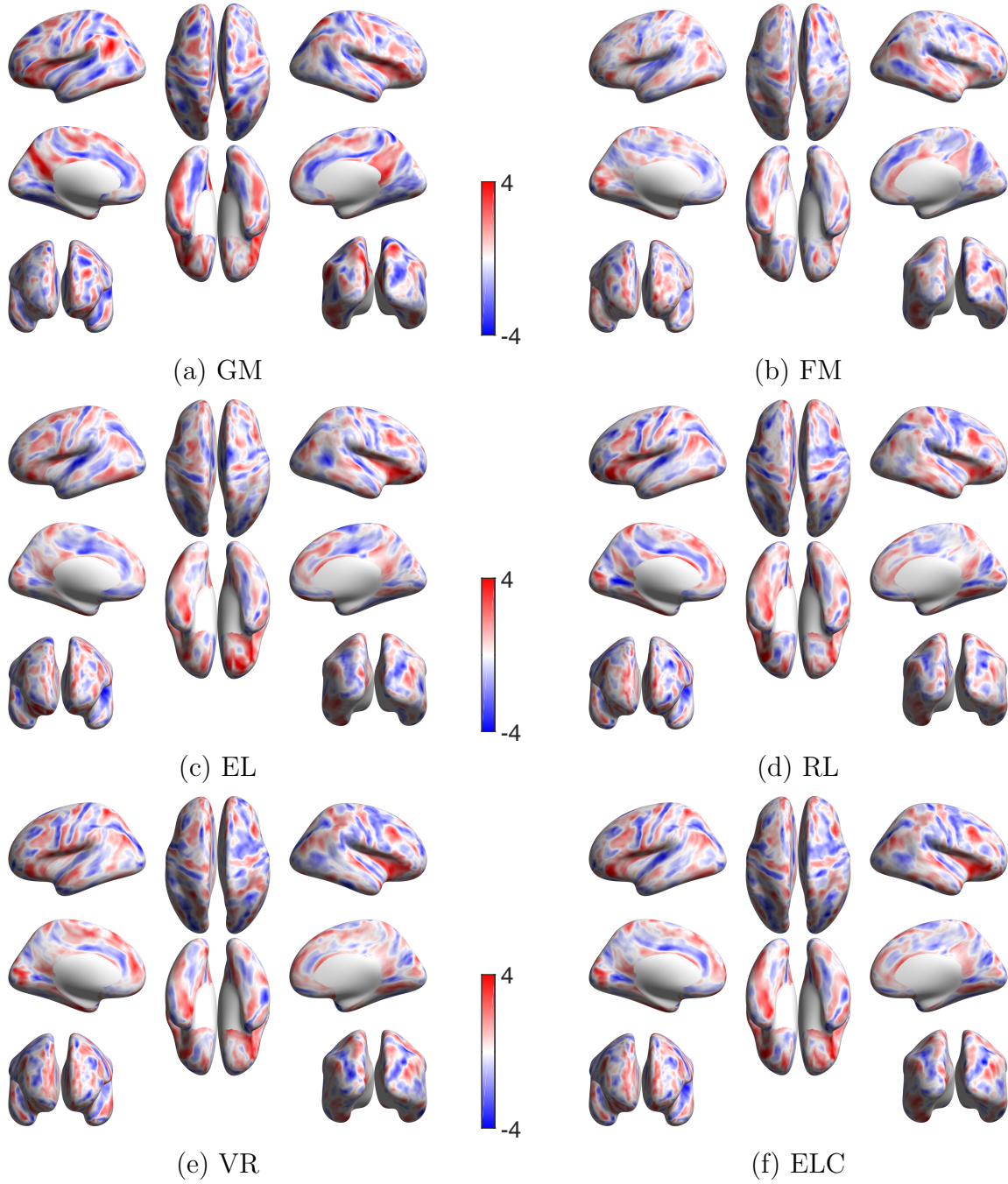


Figure 6.6: Raw association with cognitive development using optimal kernel size ( $200 \text{ mm}^2$  ( $r \approx 8 \text{ mm}$ )) with 6 categories of MSEL. The overall pattern of GM is quite different from other categories as their correlations shown in Figure 6.2.

more adaptively captures local gyrification along the cortical folding as shown in Figure 6.9.

Compared with the results with kernel size ( $200 \text{ mm}^2$ ) in Figure 6.6, the overall patterns

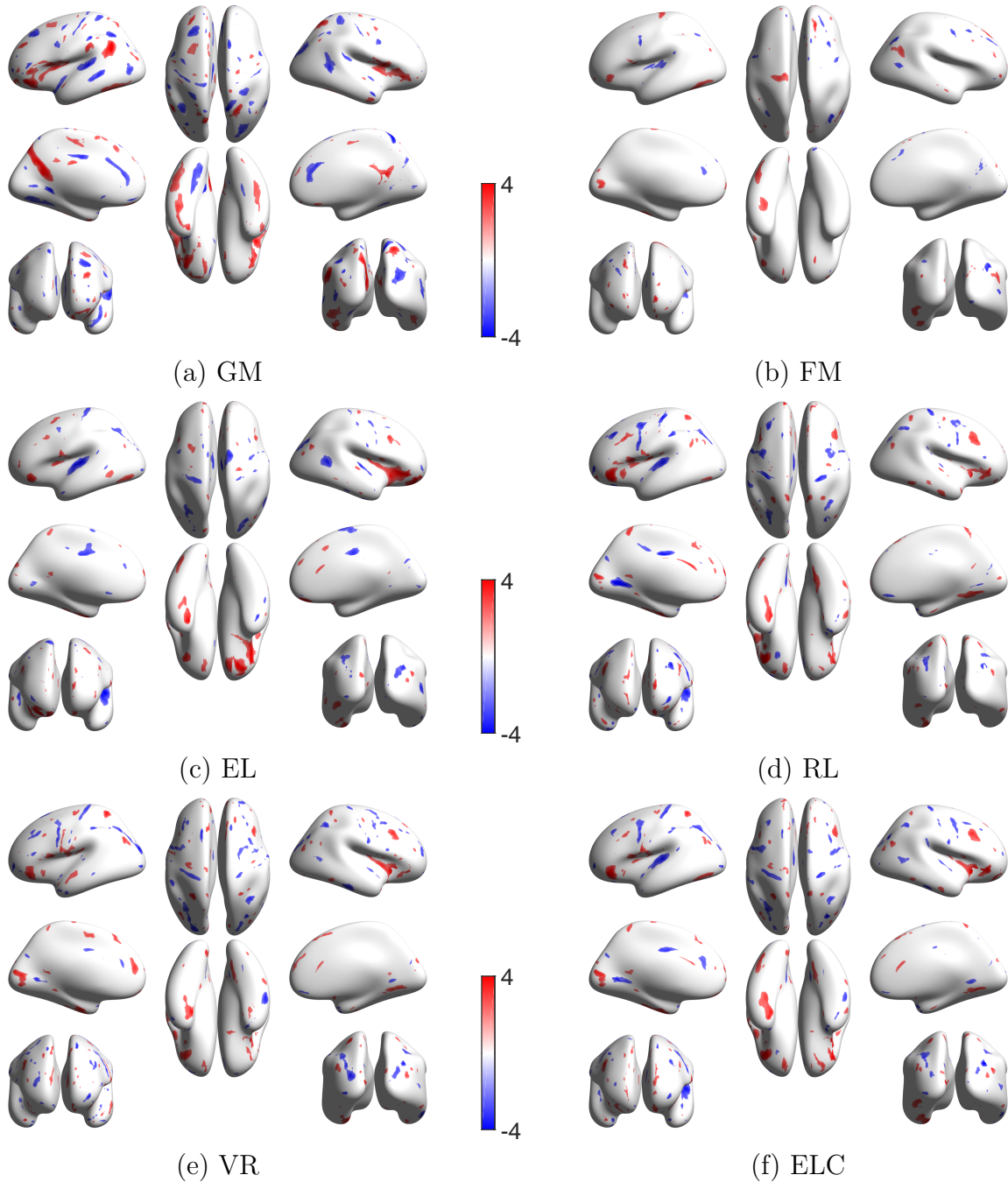
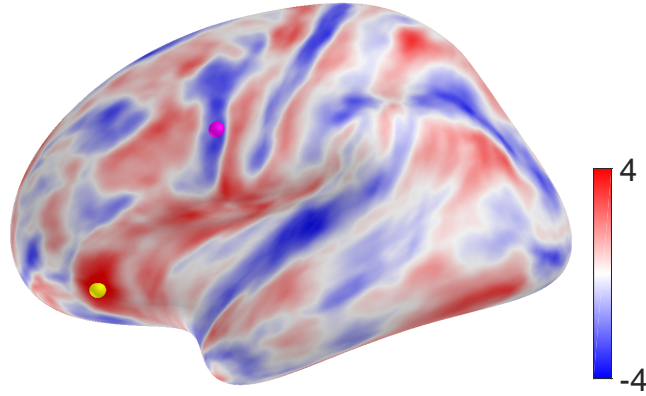
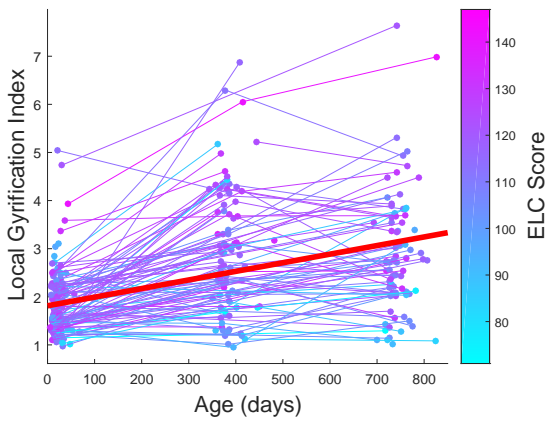


Figure 6.7: Corrected association with cognitive development with 6 categories of MSEL. Each hemisphere is divided into 76 parcels based on the pre-labeled atlas for multi-comparison correction. The overall pattern of GM is quite different from other categories as their correlations shown in Figure 6.2.

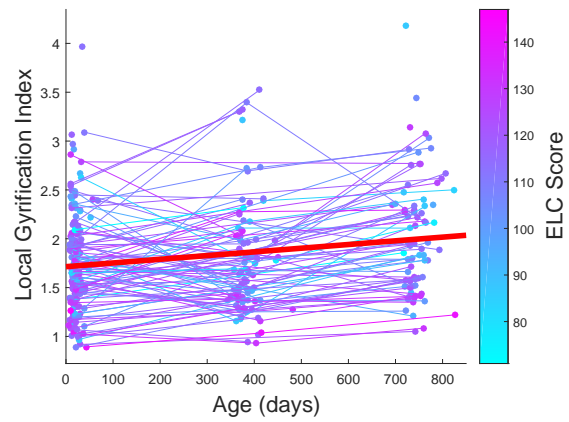
with the large kernel size ( $800 \text{ mm}^2$ ) are similar such that the average Pearson correlation of the local gyrification index across vertices is 0.65 and 0.66 for the left and right hemispheres,



(a)  $t$ -score: association with ELC on the left hemisphere



(b) positive association



(c) negative association

Figure 6.8: Local gyrification change over age and its association with ELC in two representative cortical locations. The (b) positive and (c) negative associations with ELC are illustrated in the cortical surface (a) colored by *yellow* and *magenta*, respectively. The red line in (b) and (c) indicates a linear fitting of the local gyrification index with respect to the age effect. Both locations have positive correlation with age, while showing different associations with ELC.

respectively. As expected, increasing kernel size smoothed out the observed cortical folding patterns.

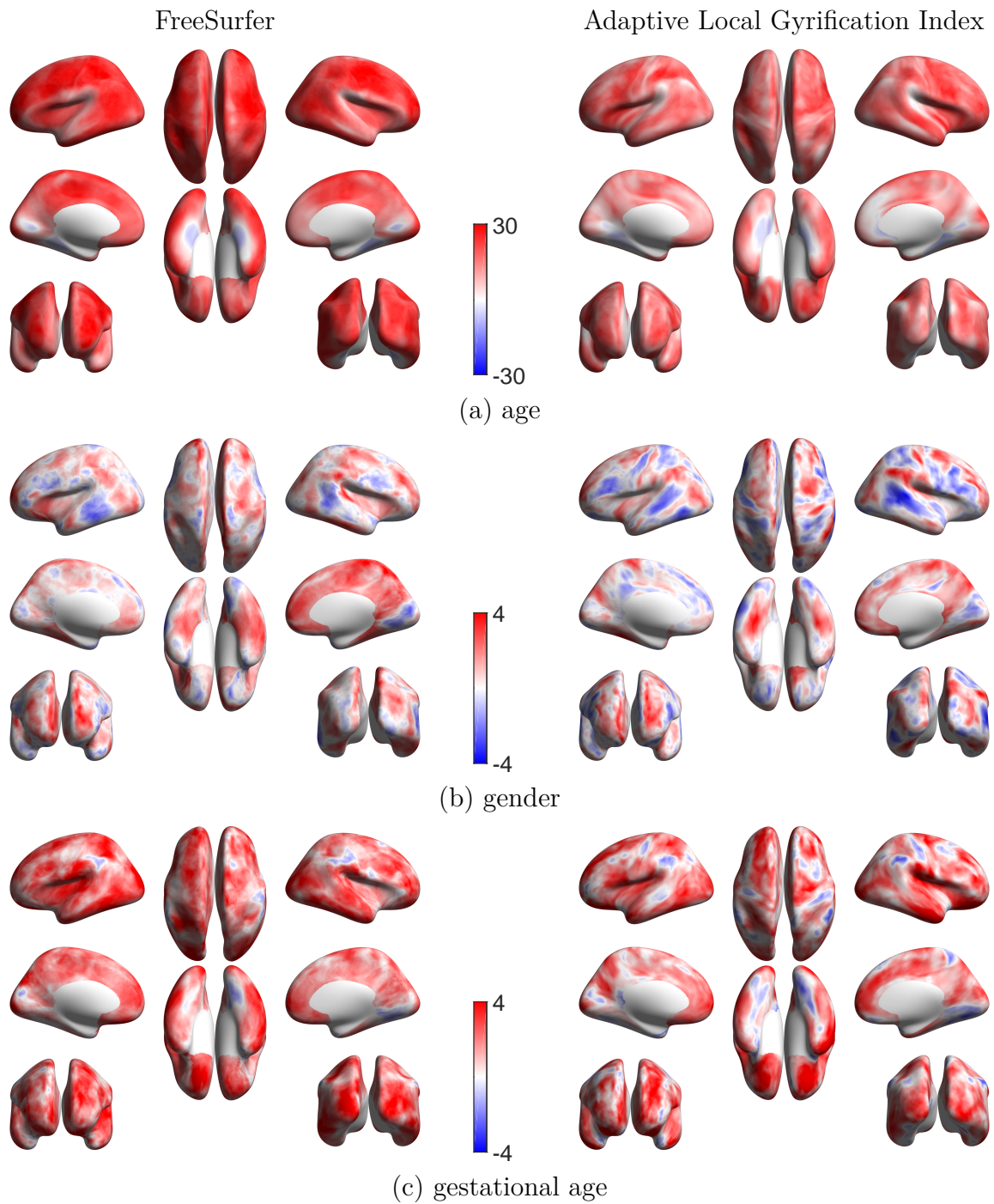


Figure 6.9: Comparison: association with demographic effects using large kernel size ( $800 \text{ mm}^2$  ( $r \approx 16 \text{ mm}$ )). The FreeSurfer method captures overall blurred measurements across the entire cortex, whereas the proposed method reveals correlation in a more adaptive and detailed way along the sulcal folding. In addition, even with a large kernel size, the proposed gyrfication index has similar patterns to that with the small kernel size.

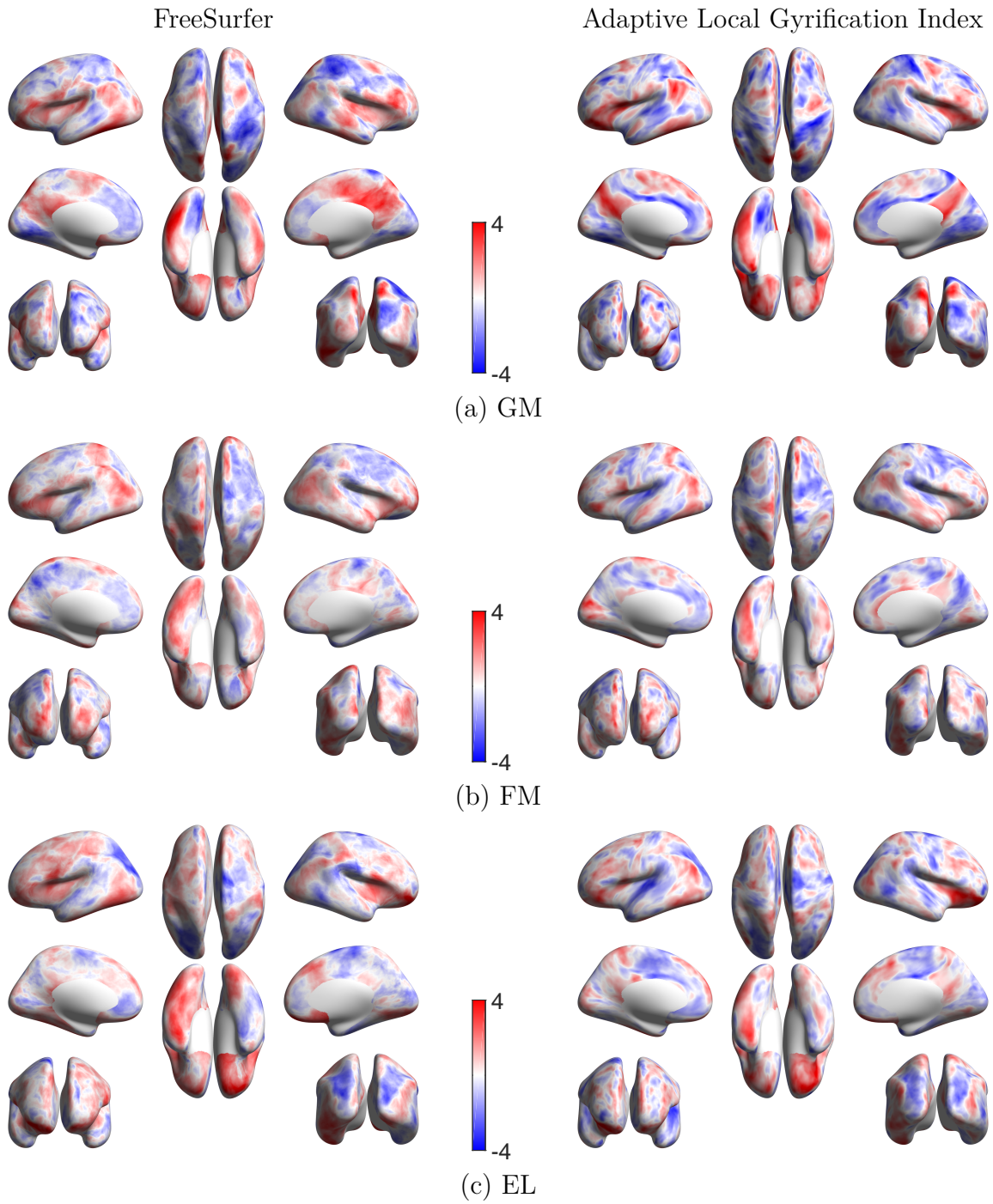


Figure 6.10: Comparison: association with 6 categories of MSEL using large kernel size ( $800 \text{ mm}^2$  ( $r \approx 16 \text{ mm}$ )). The overall pattern is quite similar to the optimal kernel-based results as shown in Figure 6.6. The larger regions have higher  $t$ -scores as the kernel size increases.

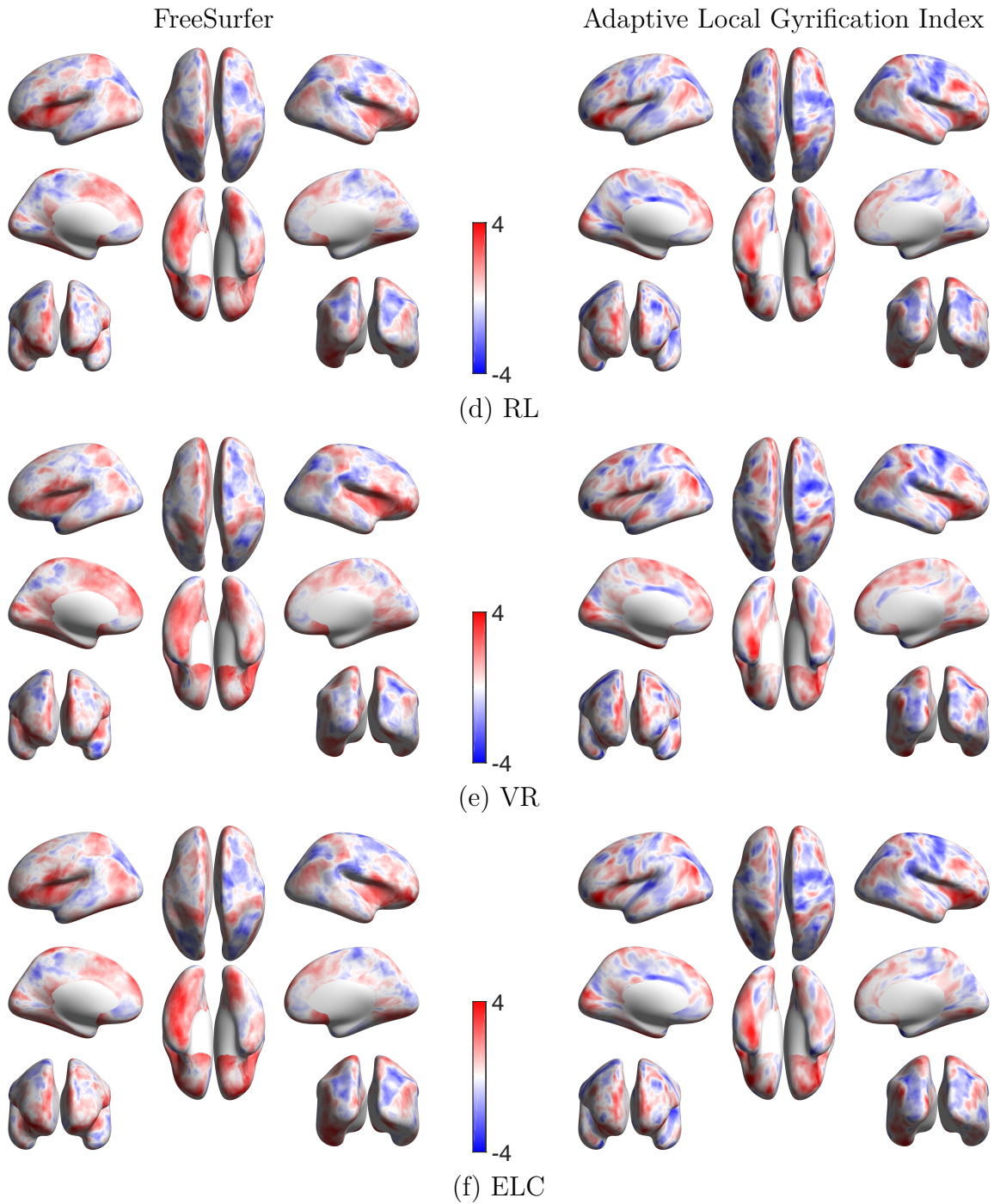


Figure 6.10: Comparison: association with 6 categories of MSEL using large kernel size ( $800 \text{ mm}^2$  ( $r \approx 16 \text{ mm}$ )) (continued).

## 6.6 Summary

In this chapter, I presented an application of my method to the EBDS dataset. Due to a high within-subject correlation, linear mixed models were proposed to incorporate fixed

effects including age and demographic information. In addition to those mixed effects, the early cognitive scores measured via MSEL were employed in the linear models to reveal the association between local gyrification and early cognitive development.

The experimental results revealed several findings via my proposed pipeline. First, most cortical regions have positive correlation with age, and my method revealed more refined regions of significant change along the sulcal foldings than existing methods. For gender and gestational age effects, I also observed several regions to be statistically significant. Second, the associations with ELC showed a strongly similar pattern across different categories of MSEL except for GM. Moreover, several regions show totally different associations with cognitive scores compared to the age effects. Finally, the statistically significant regions revealed via the proposed local gyrification index roughly agreed with those of existing methods. However, the statistically significant regions were more to local cortical folding, displaying far more detail than existing methods.

## CHAPTER 7: SUMMARY AND CONCLUSION

In this last chapter, I review and discuss the contributions of my work in Section 7.1 and its limitations in Section 7.2 followed by a discussion of possible future work in Section 7.3.

### 7.1 Summary of Contributions

This dissertation investigated cortical surface correspondence and cortical shape analysis including 1) sulcal curve extraction from the cortical surface, 2) sulcal-curve-guided cortical surface registration via entropy minimization, 3) sulcal/gyral-curve-adaptive gyrification index computation, and 4) a population study of the association between local gyrification index changes and cognitive development from neonate to 2 years of age. The contributions of this dissertation are as follows.

1. *Sulcal curves were automatically extracted from the cortical surface in a robust way to surface noise.*

Chapter 3 demonstrated the automatic sulcal curve extraction in two main steps. To select candidate sulcal points, the line simplification method was employed due to its denoising effects that naturally handles surface noise. Sulcal curves were extracted from the candidate sulcal points by tracing their curvature flow with a smoothing constraint. In the experiment, the proposed algorithm achieved a high quality of automatic sulcal curve extraction from two points of view: 1) the resulting sulcal curves were consistently extracted at different noise levels, and 2) smaller distance errors on curve extraction

were observed compared to a selected conventional method.

Unlike surface registration-based methods, the proposed sulcal curve extraction does not necessitate a template, and only a single parameter was required, to control the number of candidate sulcal points. In general, this sulcal curve extraction can be applied to any type of surface models to delineate their ridge/valley curves. In Chapter 5, the gyral curves were extracted as an inverse sulcal curve problem with the same methodology.

2. *A population correspondence was established and optimized simultaneously across the population free of a template selection bias.*

In Chapter 4, a set of labeled sulcal curves were employed for landmark matching, and each deformation field was estimated via entropy minimization. Sulcal curves were automatically labeled, resulting in the curve correspondence across a population. In this algorithm each deformation field was decomposed using spherical harmonic basis functions for a smooth and continuous representation of the deformation. An optimal pole selection was proposed to minimize the singularity effects at the poles. The entire optimization was then achieved by minimizing the entropy of the corresponding sulcal curve landmarks and the geometric features over the unit sphere. Compared to conventional shape correspondence, the proposed shape correspondence performed better in several ways in my experiments: 1) smaller variability of sulcal curve/cortical thickness, 2) better visual assessments, 3) smaller reconstruction errors in generalization and sensitivity, and 4) enhanced classification of shape models. Moreover, since the resulting deformation field was continuous and smooth, a deformation field can be created at any desired level of smoothness by simply adding/removing high frequency

basis functions. Overall, the group-wise correspondence method was able to provide improved shape correspondence for not only human cortical surfaces but also several non-human surfaces, even for highly variable models like the presented primate molar shape.

3. *A cortical-shape-adaptive kernel design was proposed to quantify cortical folding patterns.*

The cortical-shape-adaptive kernel was presented in Chapter 5. The H-J PDE was employed to incorporate the local cortical folding via a wavefront propagation approach. The surface model was represented as a medium having anisotropic speed functions to guide the wavefront propagation over the surface. To adaptively capture the local cortical folding, the local regions were segmented based on the sulcal/gyral curve information. Then, for the adaptive kernel creation a speed tensor was determined depending on the cortical location having 1) almost isotropic speed around the sulcal banks and 2) highly anisotropic speed at the sulcal fundi/gyral crowns. In my experiments, the proposed kernel-based local gyrification index achieved better performance than the conventional method in reproducibility and sensitivity by varying kernel size and the amount of the anisotropy. In the human phantom dataset, the shape-adaptive kernel produced comparable (even a bit better) reliability to the conventional method, and the cortical gyrification achieved high sensitivity along the cortical folding patterns. In contrast to the conventional geodesic kernel, the adaptive kernel covered the cortical regions with spatial similarity and improved biological interpretation as it follows sulcal patterns belonging to regions with similar functionality.

4. *As an application, a population study of early cortical morphometric development was*

*conducted to reveal the association between local gyrification index changes and cognitive development.*

Chapter 6 revealed the association between local gyrification index changes and cognitive development over early ages. The early brain development study (EBDS) database was employed for that analysis. The experimental results showed high (positive and negative) correlation of cortical folding changes over the early postnatal phase. In addition, several cortical regions exhibited strong associations with early cognitive development, and the resulting statistically significant regions were more detailed along the functionally related sulcal folding patterns than in existing methods. The proposed local gyrification index achieved overall a higher sensitivity in the cortical gyrification analysis.

5. *The source codes of the proposed methods are publicly available.*

The source codes of the methods proposed in this dissertation are open to the public. They are available at <http://github.com/ilwoolyu/>. The implementation details are described in each source code.

## **7.2 Limitations**

Here is a brief summary of the limitations of each proposed method:

1. *Automatic cortical sulcal curve extraction*

The curve extraction is purely based on the cortical surface geometry. The sulcal points are selected based only on a 2D contour shape associated with principal curvature. Since the extracted sulcal curves are obtained along the nearest neighboring sulcal

points, it could be also different from the manual delineation although there is no ground-truth or commonly agreed protocol of the sulcal curve delineation.

### 2. *Sulcal-curve-guided cortical surface registration via entropy minimization*

The surface registration based on the spherical harmonics representation requires a spherical mapping that distorts the original cortical shape like many applications employing spherical representations. A large number of basis functions are required for a fine, sharp spherical harmonic representation. Finally, the entropy computation is based on the eigendecomposition of the covariance matrix whose size is proportional to the number of subjects. Since the covariance matrix is generally non-sparse and of full rank, it is computationally demanding.

### 3. *Sulcal/gyral-curve-adaptive local gyrification index*

The adaptive kernel is created without biological information such as cortical labels. The kernel thus could still cover several regions that have different functionality although the proposed method shows in the experiment better region-specific performance than the existing method. Moreover, since the cortical folding (size, shape, etc.) varies across the surface, the use of the fixed kernel size is not optimal. An optimal kernel size would be preferable in many applications. However, as discussed in Section 5.10, choosing such an optimal kernel size is difficult for every location of the cortical surface due to a high shape variability.

### 7.3 Future Work

There are several directions for future research related to this dissertation. Some of these are reviewed in this section.

#### 7.3.1 Computational Issues

**Parallel Processing** The candidate sulcal point detection is clearly an independent task across vertices in the sulcal curve extraction method presented in Chapter 3. This implies that the proposed method has a high scalability, so it could be well organized into parallel processing to expedite the entire candidate point selection procedure. It is generally time-consuming to compute a local gyrification index for each vertex on the pial surface, as shown in Chapter 5. Such an issue could be handled by a uniform (or shape-adaptive) sampling over the cortical surface to reduce redundantly overlapped regions that produce almost the same index as its neighboring vertices. Similar to the sulcal curve extraction, the proposed method has a high scalability by parallelizing the entire processing to simultaneously handle each vertex due to their independent computations. This parallelization may yield significant computational improvements.

**Query to Closest Triangle** Through the chapters in this dissertation, a standard AABB tree representation was employed to find the closest triangle at a given surface location. For static surface objects, such a tree representation is fairly efficient for fast culling of the farthest triangles, resulting in  $O(\log N)$  computation time with only  $O(N)$  space, where  $N$  is the number of the triangles. This was well incorporated with the contour extraction even

for a large number of vertices, as shown in Chapter 3. For dynamic objects such as the deformable spheres discussed in Chapter 4, however, a tree update was required at every iteration, which takes  $O(N)$  computation time. This could be improved with an incorporation of either parallelized hierarchical representations of the deformable object, widely used in the collision detection field, or a sphere-oriented culling technique. A cache hit/miss technique could also be an alternative to this approach since the amount of the spherical deformation was small at each iteration as long as the subjects remain roughly aligned, which increases the chance to refer to the previous closest triangle again.

### 7.3.2 Applications

There could be several applications of the proposed pipeline, as it is flexible and can be easily adapted to any shape analysis study.

**Geometric Landmarks and Features** The proposed method allows the inclusion of additional information such as DTI-based connectivity [92] or myelination map alignment [108]. Furthermore, any known prior information can be straightforwardly propagated from the template to assist cortical correspondence establishment. The proposed method could further be improved by incorporating the entropy-based sulcal variability as proposed in Chapter 4. The inter-subject variability of sulcal curves and sulcal depth defined in the template space could be straightforwardly integrated into the entropy estimation. Finally, the current mean/median computation of the landmarks over the sphere is performed under Euclidean assumptions. It could be more accurately estimated using a Fréchet mean framework for example.

**Shape Quantification** As the proposed kernel is not limited to a local gyrification index computation, it can be applied to evaluate different cortical measures such as cortical thickness or shape complexity index [49]. I plan to apply the proposed method to cortical development using such different cortical measures. In addition, a combination of those different metrics measured in the proposed kernel could support geometric surface-related methods such as cortical surface registration.

**Clinical Studies** The current study has focused on the cortical gyrification in the typically developing population. There could be several other studies using the pipeline proposed throughout this dissertation. As mentioned before, one third of the EBDS study subjects exhibit high potential risk to schizophrenia. It would be interesting to figure out the difference between typically developing and at-risk groups in the early postnatal phase.

## REFERENCES

- [1] A. V. Aho and J. E. Hopcroft. *The design and analysis of computer algorithms*. Pearson Education India, 1974.
- [2] E. Armstrong, A. Schleicher, H. Omran, M. Curtis, and K. Zilles. The ontogeny of human gyrification. *Cerebral Cortex*, 5(1):56–63, 1995.
- [3] G. Auzias, J. Lefevre, A. Le Troter, C. Fischer, M. Perrot, J. Régis, and O. Coulon. Model-driven harmonic parameterization of the cortical surface: Hip-hop. *IEEE transactions on medical imaging*, 32(5):873–887, 2013.
- [4] P. G. Batchelor, A. C. Smith, D. L. G. Hill, D. J. Hawkes, T. C. S. Cox, and A. Dean. Measures of folding applied to the development of the human fetal brain. *IEEE transactions on medical imaging*, 21(8):953–965, 2002.
- [5] K. J. Behnke, M. E. Rettmann, D. L. Pham, D. Shen, S. M. Resnick, C. Davatzikos, and J. L. Prince. Automatic classification of sulcal regions of the human brain cortex using pattern recognition. In *Medical Imaging 2003*, pages 1499–1510. International Society for Optics and Photonics, 2003.
- [6] Y. Benjamini and Y. Hochberg. Controlling the false discovery rate: a practical and powerful approach to multiple testing. *Journal of the royal statistical society. Series B (Methodological)*, pages 289–300, 1995.
- [7] D. M. Boyer. Relief index of second mandibular molars is a correlate of diet among prosimian primates and other euarchontan mammals. *Journal of Human Evolution*, 55(6):1118–1137, 2008.
- [8] D. M. Boyer, Y. Lipman, E. M. St. Clair, J. Puente, B. A. Patel, T. A. Funkhouser, J. Jernvall, and I. Daubechies. Algorithms to automatically quantify the geometric similarity of anatomical surfaces. *Proceedings of the National Academy of Sciences*, 108(45):18221–18226, 2011.
- [9] C. M. Brechbühler. *Description and analysis of 3-D shapes by parametrization of closed surfaces*. PhD thesis, Diss. Techn. Wiss. ETH Zürich, Nr. 10979, 1995. Ref.: Guido Gerig; Korref.: Nicholas Ayache, 1995.
- [10] A. Cachia, M.-L. Paillère-Martinot, A. Galinowski, D. Januel, R. de Beaurepaire, F. Bellivier, E. Artiges, J. Andoh, D. Bartrés-Faz, E. Duchesnay, et al. Cortical folding abnormalities in schizophrenia patients with resistant auditory hallucinations. *Neuroimage*, 39(3):927–935, 2008.
- [11] J. Cates, P. Fletcher, M. Styner, M. Shenton, and R. Whitaker. Shape modeling and analysis with entropy-based particle systems. In N. Karssemeijer and B. Lelieveldt, editors, *Information Processing in Medical Imaging 2007*, volume 4584 of *LNCS*, pages 333–345. Springer, Heidelberg, 2007.

- [12] V. S. Caviness, J. Meyer, N. Makris, and D. N. Kennedy. Mri-based topographic parcellation of human neocortex: an anatomically specified method with estimate of reliability. *Journal of Cognitive Neuroscience*, 8(6):566–587, 1996.
- [13] M. K. Chung, K. M. Dalton, and R. J. Davidson. Tensor-based cortical surface morphometry via weighted spherical harmonic representation. *IEEE transactions on medical imaging*, 27(8):1143–1151, 2008.
- [14] T. M. Cover and J. A. Thomas. *Elements of information theory*. John Wiley & Sons, 2012.
- [15] M. D. Cykowski, O. Coulon, P. V. Kochunov, K. Amunts, J. L. Lancaster, A. R. Laird, D. C. Glahn, and P. T. Fox. The central sulcus: an observer-independent characterization of sulcal landmarks and depth asymmetry. *Cerebral Cortex*, 18(9):1999–2009, 2008.
- [16] M. D. Cykowski, P. V. Kochunov, R. J. Ingham, J. C. Ingham, J.-F. Mangin, D. Rivière, J. L. Lancaster, and P. T. Fox. Perisylvian sulcal morphology and cerebral asymmetry patterns in adults who stutter. *Cerebral Cortex*, 18(3):571–583, 2008.
- [17] A. M. Dale, B. Fischl, and M. I. Sereno. Cortical surface-based analysis: I. segmentation and surface reconstruction. *Neuroimage*, 9(2):179–194, 1999.
- [18] J. Damon. Swept regions and surfaces: modeling and volumetric properties. *Theoretical Computer Science*, 392(1):66–91, 2008.
- [19] R. Davies, C. Twining, T. Cootes, and C. Taylor. Building 3-d statistical shape models by direct optimization. *IEEE Transactions on Medical Imaging*, 29(4):961–981, 2010.
- [20] R. H. Davies. *Learning shape: optimal models for analysing natural variability*. PhD thesis, University of Manchester, 2002.
- [21] R. H. Davies, C. J. Twining, P. D. Allen, T. F. Cootes, and C. J. Taylor. Shape discrimination in the hippocampus using an mdl model. In *Information Processing in Medical Imaging*, pages 38–50. Springer, 2003.
- [22] R. S. Desikan, F. Ségonne, B. Fischl, B. T. Quinn, B. C. Dickerson, D. Blacker, R. L. Buckner, A. M. Dale, R. P. Maguire, B. T. Hyman, et al. An automated labeling system for subdividing the human cerebral cortex on mri scans into gyral based regions of interest. *Neuroimage*, 31(3):968–980, 2006.
- [23] C. Destrieux, B. Fischl, A. Dale, and E. Halgren. Automatic parcellation of human cortical gyri and sulci using standard anatomical nomenclature. *Neuroimage*, 53(1):1–15, 2010.
- [24] G. Douaud, T. E. Behrens, C. Poupon, Y. Cointepas, S. Jbabdi, V. Gaura, N. Golestani, P. Krystkowiak, C. Verny, P. Damier, et al. In vivo evidence for the selective subcortical degeneration in huntington’s disease. *Neuroimage*, 46(4):958–966, 2009.

- [25] D. Douglas and T. Peucker. Algorithms for the reduction of the number of points required to represent a digitized line or its caricature. *Cartographica: The International Journal for Geographic Information and Geovisualization*, 10(2):112–122, 1973.
- [26] J. Du, L. Younes, and A. Qiu. Whole brain diffeomorphic metric mapping via integration of sulcal and gyral curves, cortical surfaces, and images. *NeuroImage*, 56(1):162–173, 2011.
- [27] J. Dubois, M. Benders, C. Borradori-Tolsa, A. Cachia, F. Lazeyras, R. H.-V. Leuchter, S. Sizonenko, S. Warfield, J. Mangin, and P. S. Hüppi. Primary cortical folding in the human newborn: an early marker of later functional development. *Brain*, 131(8):2028–2041, 2008.
- [28] S. Durrleman, X. Pennec, A. Trouvé, and N. Ayache. Measuring brain variability via sulcal lines registration: a diffeomorphic approach. In *Medical Image Computing and Computer-Assisted Intervention–MICCAI 2007*, pages 675–682. Springer, 2007.
- [29] H. Elias and D. Schwartz. Surface areas of the cerebral cortex of mammals determined by stereological methods. *Science*, 166(3901):111–113, 1969.
- [30] B. Fischl. Freesurfer. *Neuroimage*, 62(2):774–781, 2012.
- [31] B. Fischl, M. Sereno, R. Tootell, and A. Dale. High-resolution intersubject averaging and a coordinate system for the cortical surface. *Human Brain Mapping*, 8(4):272–284, 1999.
- [32] B. Fischl, A. Liu, and A. M. Dale. Automated manifold surgery: constructing geometrically accurate and topologically correct models of the human cerebral cortex. *IEEE transactions on medical imaging*, 20(1):70–80, 2001.
- [33] B. Fischl, A. van der Kouwe, C. Destrieux, E. Halgren, F. Ségonne, D. H. Salat, E. Busa, L. J. Seidman, J. Goldstein, D. Kennedy, et al. Automatically parcellating the human cerebral cortex. *Cerebral cortex*, 14(1):11–22, 2004.
- [34] A. Fornito, S. J. Wood, S. Whittle, J. Fuller, C. Adamson, M. M. Saling, D. Velakoulis, C. Pantelis, and M. Yücel. Variability of the paracingulate sulcus and morphometry of the medial frontal cortex: associations with cortical thickness, surface area, volume, and sulcal depth. *Human brain mapping*, 29(2):222–236, 2008.
- [35] C. Gaser, E. Luders, P. M. Thompson, A. D. Lee, R. A. Dutton, J. A. Geaga, K. M. Hayashi, U. Bellugi, A. M. Galaburda, J. R. Korenberg, et al. Increased local gyrification mapped in williams syndrome. *Neuroimage*, 33(1):46–54, 2006.
- [36] J. H. Gilmore, W. Lin, M. W. Prastawa, C. B. Looney, Y. S. K. Vetsa, R. C. Knickmeyer, D. D. Evans, J. K. Smith, R. M. Hamer, J. A. Lieberman, et al. Regional gray matter growth, sexual dimorphism, and cerebral asymmetry in the neonatal brain. *The Journal of neuroscience*, 27(6):1255–1260, 2007.

- [37] J. H. Gilmore, J. E. Schmitt, R. C. Knickmeyer, J. K. Smith, W. Lin, M. Styner, G. Gerig, and M. C. Neale. Genetic and environmental contributions to neonatal brain structure: a twin study. *Human brain mapping*, 31(8):1174–1182, 2010.
- [38] J. H. Gilmore, F. Shi, S. L. Woolson, R. C. Knickmeyer, S. J. Short, W. Lin, H. Zhu, R. M. Hamer, M. Styner, and D. Shen. Longitudinal development of cortical and subcortical gray matter from birth to 2 years. *Cerebral Cortex*, 22(11):2478–2485, 2012.
- [39] D. Holland, L. Chang, T. M. Ernst, M. Curran, S. D. Buchthal, D. Alicata, J. Skranes, H. Johansen, A. Hernandez, R. Yamakawa, et al. Structural growth trajectories and rates of change in the first 3 months of infant brain development. *JAMA neurology*, 71(10):1266–1274, 2014.
- [40] K. Im, H. J. Jo, J.-F. Mangin, A. C. Evans, S. I. Kim, and J.-M. Lee. Spatial distribution of deep sulcal landmarks and hemispherical asymmetry on the cortical surface. *Cerebral cortex*, 20(3):602–611, 2010.
- [41] M. Jackowski, C. Y. Kao, M. Qiu, R. T. Constable, and L. H. Staib. White matter tractography by anisotropic wavefront evolution and diffusion tensor imaging. *Medical image analysis*, 9(5):427–440, 2005.
- [42] H. J. Jerison. Quantitative analysis of evolution of the brain in mammals. *Science*, 133(3457):1012–1014, 1961.
- [43] S. E. Jones, B. R. Buchbinder, and I. Aharon. Three-dimensional mapping of cortical thickness using laplace’s equation. *Human brain mapping*, 11(1):12–32, 2000.
- [44] A. A. Joshi, D. W. Shattuck, P. M. Thompson, and R. M. Leahy. Surface-constrained volumetric brain registration using harmonic mappings. *Medical Imaging, IEEE Transactions on*, 26(12):1657–1669, 2007.
- [45] C. Y. Kao, S. Osher, and J. Qian. Lax–friedrichs sweeping scheme for static hamilton–jacobi equations. *Journal of Computational Physics*, 196(1):367–391, 2004.
- [46] C.-Y. Kao, M. Hofer, G. Sapiro, J. Stern, K. Rehm, and D. A. Rottenberg. A geometric method for automatic extraction of sulcal fundi. *Medical Imaging, IEEE Transactions on*, 26(4):530–540, 2007.
- [47] J. Kent, K. Mardia, and J. West. Ridge curves and shape analysis. In *The British Machine Vision Conference 1996*, pages 43–52, 1996.
- [48] J. Kim, V. Singh, J. Lee, J. Lerch, Y. Ad-Dab’bagh, D. MacDonald, J. Lee, S. Kim, and A. Evans. Automated 3-d extraction and evaluation of the inner and outer cortical surfaces using a laplacian map and partial volume effect classification. *NeuroImage*, 27(1):210–221, 2005.
- [49] S. H. Kim, I. Lyu, V. S. Fonov, C. Vachet, H. C. Hazlett, R. G. Smith, J. Piven, S. R. Dager, R. C. Mckinstry, J. R. Pruett, et al. Development of cortical shape in the human brain from 6 to 24months of age via a novel measure of shape complexity. *NeuroImage*, 135:163–176, 2016.

- [50] R. C. Knickmeyer, S. Gouttard, C. Kang, D. Evans, K. Wilber, J. K. Smith, R. M. Hamer, W. Lin, G. Gerig, and J. H. Gilmore. A structural mri study of human brain development from birth to 2 years. *The Journal of Neuroscience*, 28(47):12176–12182, 2008.
- [51] J. J. Koenderink and A. J. van Doorn. Surface shape and curvature scales. *Image and vision computing*, 10(8):557–564, 1992.
- [52] A. C. Kotcheff and C. J. Taylor. Automatic construction of eigenshape models by direct optimization. *Medical Image Analysis*, 2(4):303–314, 1998.
- [53] B. A. Landman, A. J. Huang, A. Gifford, D. S. Vikram, I. A. L. Lim, J. A. Farrell, J. A. Bogovic, J. Hua, M. Chen, S. Jarso, et al. Multi-parametric neuroimaging reproducibility: a 3-t resource study. *Neuroimage*, 54(4):2854–2866, 2011.
- [54] G. Le Goualher, E. Procyk, D. L. Collins, R. Venugopal, C. Barillot, and A. C. Evans. Automated extraction and variability analysis of sulcal neuroanatomy. *IEEE transactions on medical imaging*, 18(3):206–217, 1999.
- [55] A. Le Troter, G. Auzias, and O. Coulon. Automatic sulcal line extraction on cortical surfaces using geodesic path density maps. *NeuroImage*, 61(4):941–949, 2012.
- [56] E. Lebed, C. Jacova, L. Wang, and M. F. Beg. Novel surface-smoothing based local gyrification index. *Medical Imaging, IEEE Transactions on*, 32(4):660–669, 2013.
- [57] J. Lee, I. Lyu, I. Oguz, and M. A. Styner. Particle-guided image registration. In *Medical Image Computing and Computer-Assisted Intervention–MICCAI 2013*, pages 203–210. Springer, 2013.
- [58] J. Lee, S. H. Kim, I. Oguz, and M. Styner. Enhanced cortical thickness measurements for rodent brains via lagrangian-based rk4 streamline computation. In *SPIE Medical Imaging*, pages 97840B–97840B. International Society for Optics and Photonics, 2016.
- [59] P. F. O. Leipsic. Developmental (myelogenetic) localisation of the cerebral cortex in the human subject. *The Lancet*, 158(4077):1027–1030, 1901.
- [60] M. Leordeanu and M. Hebert. A spectral technique for correspondence problems using pairwise constraints. In *Tenth IEEE International Conference on Computer Vision (ICCV’05) Volume 1*, volume 2, pages 1482–1489. IEEE, 2005.
- [61] G. Li, L. Guo, J. Nie, and T. Liu. An automated pipeline for cortical sulcal fundi extraction. *Medical image analysis*, 14(3):343–359, 2010.
- [62] G. Li, L. Wang, F. Shi, A. E. Lyall, W. Lin, J. H. Gilmore, and D. Shen. Mapping longitudinal development of local cortical gyrification in infants from birth to 2 years of age. *The Journal of Neuroscience*, 34(12):4228–4238, 2014.
- [63] G. Lohmann. Extracting line representations of sulcal and gyral patterns in mr images of the human brain. *IEEE Transactions on Medical Imaging*, 17(6):1040–1048, 1998.

- [64] G. Lohmann and D. Von Cramon. Automatic labelling of the human cortical surface using sulcal basins. *Medical Image Analysis*, 4(3):179–188, 2000.
- [65] H. Lombaert, J. Sporring, and K. Siddiqi. Diffeomorphic spectral matching of cortical surfaces. In *Information Processing in Medical Imaging*, pages 376–389. Springer, 2013.
- [66] C. B. Looney, J. K. Smith, L. H. Merck, H. M. Wolfe, N. C. Chescheir, R. M. Hamer, and J. H. Gilmore. Intracranial hemorrhage in asymptomatic neonates: prevalence on mr images and relationship to obstetric and neonatal risk factors 1. *Radiology*, 242(2): 535–541, 2007.
- [67] E. Luders, K. L. Narr, P. M. Thompson, D. E. Rex, L. Jancke, H. Steinmetz, and A. W. Toga. Gender differences in cortical complexity. *Nature neuroscience*, 7(8):799–800, 2004.
- [68] J. H. Lui, D. V. Hansen, and A. R. Kriegstein. Development and evolution of the human neocortex. *Cell*, 146(1):18–36, 2011.
- [69] L. M. Lui, S. R. Thiruvankadam, Y. Wang, P. M. Thompson, and T. F. Chan. Optimized conformal surface registration with shape-based landmark matching. *SIAM J. Imaging Sciences*, 3(1):52–78, 2010.
- [70] O. Lyttelton, M. Boucher, S. Robbins, and A. Evans. An unbiased iterative group registration template for cortical surface analysis. *NeuroImage*, 34(4):1535–1544, 2007.
- [71] I. Lyu, J. Seong, S. Shin, K. Im, J. Roh, M. Kim, G. Kim, J. Kim, A. Evans, D. Na, and J. Lee. Spectral-based automatic labeling and refining of human cortical sulcal curves using expert-provided examples. *NeuroImage*, 52(1):142–157, 2010.
- [72] I. Lyu, G. Li, M. Kim, and D. Shen. Multiple atlases-based joint labeling of human cortical sulcal curves. In *Medical Computer Vision. Recognition Techniques and Applications in Medical Imaging*, pages 124–132. Springer Berlin Heidelberg, 2012.
- [73] I. Lyu, S. Kim, J. Seong, S. Yoo, A. Evans, Y. Shi, M. Sanchez, M. Niethammer, and M. Styner. Cortical correspondence via sulcal curve-constrained spherical registration with application to macaque studies. In *Medical Imaging 2013: Image Processing*, volume 8669. SPIE, 2013.
- [74] I. Lyu, S. H. Kim, J.-K. Seong, S. W. Yoo, A. C. Evans, Y. Shi, M. Sanchez, M. Niethammer, and M. A. Styner. Group-wise cortical correspondence via sulcal curve-constrained entropy minimization. In *Information Processing in Medical Imaging*, pages 364–375. Springer, 2013.
- [75] I. Lyu, S. Kim, J. Seong, S. Yoo, A. Evans, Y. Shi, M. Sanchez, M. Niethammer, and M. Styner. Robust estimation of group-wise cortical correspondence with an application to macaque and human neuroimaging studies. *Frontiers in Neuroscience*, 9:210, 2015.
- [76] I. Lyu, S. Kim, and M. Styner. Automatic sulcal curve extraction on the human cortical surface. In *Medical Imaging 2015: Image Processing*, volume 9413, pages 941324–1–941324–7. SPIE, 2015.

- [77] I. Lyu, S. H. Kim, and M. A. Styner. Cortical surface shape assessment via sulcal/gyral curve-based gyrification index. In *2016 IEEE 13th International Symposium on Biomedical Imaging (ISBI)*, pages 221–224. IEEE, 2016.
- [78] D. MacDonald, D. Avis, and A. C. Evans. Multiple surface identification and matching in magnetic resonance images. In *Visualization in Biomedical Computing 1994*, pages 160–169. International Society for Optics and Photonics, 1994.
- [79] D. MacDonald, N. Kabani, D. Avis, and A. C. Evans. Automated 3-d extraction of inner and outer surfaces of cerebral cortex from mri. *NeuroImage*, 12(3):340–356, 2000.
- [80] J. D. MacDonald. *A method for identifying geometrically simple surfaces from three dimensional images*. PhD thesis, School of Computer Science, McGill University, Montreal, 1997.
- [81] J. Mangin, D. Riviere, A. Cachia, E. Duchesnay, Y. Cointepas, D. Papadopoulos-Orfanos, P. Scifo, T. Ochiai, F. Brunelle, and J. Régis. A framework to study the cortical folding patterns. *NeuroImage*, 23:S129–S138, 2004.
- [82] J.-F. Mangin, J. Régis, I. Bloch, V. Frouin, Y. Samson, and J. López-Krahe. A mrf based random graph modelling the human cortical topography. In *Computer Vision, Virtual Reality and Robotics in Medicine*, pages 177–183. Springer, 1995.
- [83] M. Meyer, M. Desbrun, P. Schröder, and A. H. Barr. Discrete differential-geometry operators for triangulated 2-manifolds. In *Visualization and mathematics III*, pages 35–57. Springer, 2003.
- [84] O. Monga, S. Benayoun, and O. Faugeras. From partial derivatives of 3-d density images to ridge lines. In *Computer Vision and Pattern Recognition, 1992. Proceedings CVPR'92., 1992 IEEE Computer Society Conference on*, pages 354–359. IEEE, 1992.
- [85] T. W. J. Moorhead, J. M. Harris, A. C. Stanfield, D. E. Job, J. J. Best, E. C. Johnstone, and S. M. Lawrie. Automated computation of the gyrification index in prefrontal lobes: methods and comparison with manual implementation. *Neuroimage*, 31(4):1560–1566, 2006.
- [86] E. M. Mullen et al. *Mullen scales of early learning*. AGS Circle Pines, MN, 1995.
- [87] C. A. Nelson, M. L. Collins, and M. Luciana. *Handbook of developmental cognitive neuroscience*. MIT Press, 2001.
- [88] C. A. Nelson, C. H. Zeanah, N. A. Fox, P. J. Marshall, A. T. Smyke, and D. Guthrie. Cognitive recovery in socially deprived young children: The bucharest early intervention project. *Science*, 318(5858):1937–1940, 2007.
- [89] M. Niethammer, M. Reuter, F.-E. Wolter, S. Bouix, N. Peinecke, M.-S. Koo, and M. E. Shenton. Global medical shape analysis using the laplace-beltrami spectrum. In *Medical Image Computing and Computer-Assisted Intervention–MICCAI 2007*, pages 850–857. Springer, 2007.

- [90] J. R. Ockendon. *Applied partial differential equations*. Oxford University Press on Demand, 2003.
- [91] I. Oguz, J. Cates, T. Fletcher, R. Whitaker, D. Cool, S. Aylward, and M. Styner. Cortical correspondence using entropy-based particle systems and local features. In *Biomedical Imaging: From Nano to Macro, 2008. ISBI 2008. 5th IEEE International Symposium on*, pages 1637–1640. IEEE, 2008.
- [92] I. Oguz, M. Niethammer, J. Cates, R. Whitaker, T. Fletcher, C. Vachet, and M. Styner. Cortical correspondence with probabilistic fiber connectivity. In J. Prince, D. Pham, and K. Myers, editors, *Information Processing in Medical Imaging 2009*, volume 5636 of *LNCS*, pages 651–663. Springer, Heidelberg, 2009.
- [93] Y. Ohtake, A. Belyaev, and H.-P. Seidel. Ridge-valley lines on meshes via implicit surface fitting. *ACM transactions on graphics (TOG)*, 23(3):609–612, 2004.
- [94] S. Osher and J. A. Sethian. Fronts propagating with curvature-dependent speed: algorithms based on hamilton-jacobi formulations. *Journal of computational physics*, 79(1):12–49, 1988.
- [95] H. Park, J. Park, J. Seong, D. Na, and J. Lee. Cortical surface registration using spherical thin-plate spline with sulcal lines and mean curvature as features. *Journal of Neuroscience Methods*, 206(1):46–53, 2012.
- [96] M. Perrot, D. Riviere, and J.-F. Mangin. Identifying cortical sulci from localization, shape and local organization. In *2008 5th IEEE International Symposium on Biomedical Imaging: From Nano to Macro*, pages 420–423. IEEE, 2008.
- [97] R. Perrot, R. Berges, A. Bocquet, and J. Eyer. Review of the multiple aspects of neurofilament functions, and their possible contribution to neurodegeneration. *Molecular neurobiology*, 38(1):27–65, 2008.
- [98] S. M. Pizer, S. Jung, D. Goswami, J. Vicory, X. Zhao, R. Chaudhuri, J. N. Damon, S. Huckemann, and J. Marron. Nested sphere statistics of skeletal models. In *Innovations for Shape Analysis*, pages 93–115. Springer, 2013.
- [99] M. Powell. The newuoa software for unconstrained optimization without derivatives. *Large-Scale Nonlinear Optimization*, 83:255–297, 2006.
- [100] J. D. Power, A. L. Cohen, S. M. Nelson, G. S. Wig, K. A. Barnes, J. A. Church, A. C. Vogel, T. O. Laumann, F. M. Miezin, B. L. Schlaggar, and S. E. Petersen. Functional Network Organization of the Human Brain. *Neuron*, 72(4):665–678, Nov. 2011.
- [101] J. Qian, Y.-T. Zhang, and H.-K. Zhao. A fast sweeping method for static convex hamilton-jacobi equations. *Journal of Scientific Computing*, 31(1):237–271, 2007.
- [102] J. Rademacher, A. Galaburda, D. Kennedy, P. Filipek, and V. Caviness. Human cerebral cortex: localization, parcellation, and morphometry with magnetic resonance imaging. *Journal of cognitive neuroscience*, 4(4):352–374, 1992.

- [103] U. Ramer. An iterative procedure for the polygonal approximation of plane curves. *Computer graphics and image processing*, 1(3):244–256, 1972.
- [104] G. B. Reggiori. Digital computer transformations for irregular line drawings. Technical report, DTIC Document, 1972.
- [105] M. E. Rettmann, X. Han, C. Xu, and J. L. Prince. Automated sulcal segmentation using watersheds on the cortical surface. *NeuroImage*, 15(2):329–344, 2002.
- [106] D. Riviere, J.-F. Mangin, D. Papadopoulos-Orfanos, J.-M. Martinez, V. Frouin, and J. Régis. Automatic recognition of cortical sulci of the human brain using a congregation of neural networks. *Medical image analysis*, 6(2):77–92, 2002.
- [107] D. Riviere, J. Régis, Y. Cointepas, D. Papadopoulos-Orfanos, A. Cachia, and J. Mangin. A freely available anatomist/brainvisa package for structural morphometry of the cortical sulci. *NeuroImage*, 19(2):934, 2003.
- [108] E. C. Robinson, S. Jbabdi, J. Andersson, S. Smith, M. F. Glasser, D. C. Van Essen, G. Burgess, M. P. Harms, D. M. Barch, and M. Jenkinson. Multimodal surface matching: fast and generalisable cortical registration using discrete optimisation. In *Information Processing in Medical Imaging*, pages 475–486. Springer, 2013.
- [109] S. Sandor and R. Leahy. Surface-based labeling of cortical anatomy using a deformable atlas. *IEEE transactions on medical imaging*, 16(1):41–54, 1997.
- [110] M. Schaer, M. B. Cuadra, L. Tamarit, F. Lazeyras, S. Eliez, and J. Thiran. A surface-based approach to quantify local cortical gyrification. *Medical Imaging, IEEE Transactions on*, 27(2):161–170, 2008.
- [111] J. Seong, K. Im, S. Yoo, S. Seo, D. Na, and J. Lee. Automatic extraction of sulcal lines on cortical surfaces based on anisotropic geodesic distance. *NeuroImage*, 49(1):293–302, 2010.
- [112] J. A. Sethian. A fast marching level set method for monotonically advancing fronts. *Proceedings of the National Academy of Sciences*, 93(4):1591–1595, 1996.
- [113] J. A. Sethian and A. Vladimirsky. Ordered upwind methods for static hamilton–jacobi equations: Theory and algorithms. *SIAM Journal on Numerical Analysis*, 41(1):325–363, 2003.
- [114] Y. Shi, P. M. Thompson, I. Dinov, and A. W. Toga. Hamilton–jacobi skeleton on cortical surfaces. *Medical Imaging, IEEE Transactions on*, 27(5):664–673, 2008.
- [115] Y. Shi, Z. Tu, A. L. Reiss, R. A. Dutton, A. D. Lee, A. M. Galaburda, I. Dinov, P. M. Thompson, and A. W. Toga. Joint sulcal detection on cortical surfaces with graphical models and boosted priors. *IEEE transactions on medical imaging*, 28(3):361–373, 2009.
- [116] Y. Shi, R. Lai, and A. W. Toga. Conformal mapping via metric optimization with application for cortical label fusion. In *Information Processing in Medical Imaging*, pages 244–255. Springer, 2013.

- [117] R. Shishegar, J. H. Manton, D. W. Walker, J. M. Britto, and L. A. Johnston. Quantifying gyrification using laplace beltrami eigenfunction level-sets. In *2015 IEEE 12th International Symposium on Biomedical Imaging (ISBI)*, pages 1272–1275. IEEE, 2015.
- [118] G. E. Smith. A new topographical survey of the human cerebral cortex, being an account of the distribution of the anatomically distinct cortical areas and their relationship to the cerebral sulci. *Journal of anatomy and physiology*, 41(Pt 4):237, 1907.
- [119] M. Styner, I. Oguz, S. Xu, C. Brechbuler, D. Pantazis, and G. Gerig. Statistical shape analysis of brain structures using spharm-pdm. In *Insight Journal DSpace*. Citeseer, 2006.
- [120] M. Styner, S. Xu, M. El-Sayed, and G. Gerig. Correspondence evaluation in local shape analysis and structural subdivision. In *Biomedical Imaging: From Nano to Macro, 2007. ISBI 2007. 4th IEEE International Symposium on*, pages 1192–1195. IEEE, 2007.
- [121] M. Styner, I. Oguz, T. Heimann, and G. Gerig. Minimum description length with local geometry. In *Biomedical Imaging: From Nano to Macro, 2008. ISBI 2008. 5th IEEE International Symposium on*, pages 1283–1286. IEEE, 2008.
- [122] S. Su, T. White, M. Schmidt, C.-Y. Kao, and G. Sapiro. Geometric computation of human gyrification indexes from magnetic resonance images. *Human brain mapping*, 34(5):1230–1244, 2013.
- [123] X. Tao, X. Han, M. E. Rettmann, J. L. Prince, and C. Davatzikos. Statistical study on cortical sulci of human brains. In *Information Processing in Medical Imaging*, pages 475–487. Springer, 2001.
- [124] X. Tao, J. L. Prince, and C. Davatzikos. Using a statistical shape model to extract sulcal curves on the outer cortex of the human brain. *IEEE Transactions on Medical Imaging*, 21(5):513–524, 2002.
- [125] P. Thompson and A. W. Toga. A surface-based technique for warping three-dimensional images of the brain. *Medical Imaging, IEEE Transactions on*, 15(4):402–417, 1996.
- [126] P. Thompson, C. Schwartz, and A. Toga. High-resolution random mesh algorithms for creating a probabilistic 3d surface atlas of the human brain. *NeuroImage*, 3(1):19–34, 1996.
- [127] J. Tohka, A. Zijdenbos, and A. Evans. Fast and robust parameter estimation for statistical partial volume models in brain mri. *Neuroimage*, 23(1):84–97, 2004.
- [128] R. Toro, M. Perron, B. Pike, L. Richer, S. Veillette, Z. Pausova, and T. Paus. Brain size and folding of the human cerebral cortex. *Cerebral cortex*, 18(10):2352–2357, 2008.
- [129] J. N. Tsitsiklis. Efficient algorithms for globally optimal trajectories. *IEEE Transactions on Automatic Control*, 40(9):1528–1538, 1995.

- [130] A. Tsui, D. Fenton, P. Vuong, J. Hass, P. Koehl, N. Amenta, D. Coeurjolly, C. DeCarli, and O. Carmichael. Globally optimal cortical surface matching with exact landmark correspondence. In *Information Processing in Medical Imaging*, pages 487–498. Springer, 2013.
- [131] L. Tu, J. Vicory, S. Elhabian, B. Paniagua, J. C. Prieto, J. N. Damon, R. Whitaker, M. Styner, and S. M. Pizer. Entropy-based correspondence improvement of interpolated skeletal models. *Computer Vision and Image Understanding*, 151:72–79, 2016.
- [132] Z. Tu, S. Zheng, A. L. Yuille, A. L. Reiss, R. A. Dutton, A. D. Lee, A. M. Galaburda, I. Dinov, P. M. Thompson, and A. W. Toga. Automated extraction of the cortical sulci based on a supervised learning approach. *IEEE Transactions on Medical Imaging*, 26(4):541–552, 2007.
- [133] C. J. Twining, T. Cootes, S. Marsland, V. Petrovic, R. Schestowitz, and C. J. Taylor. A unified information-theoretic approach to groupwise non-rigid registration and model building. In *Information Processing in Medical Imaging*, pages 1–14. Springer, 2005.
- [134] N. Tzourio-Mazoyer, B. Landeau, D. Papathanassiou, F. Crivello, O. Etard, N. Delcroix, B. Mazoyer, and M. Joliot. Automated anatomical labeling of activations in spm using a macroscopic anatomical parcellation of the mni mri single-subject brain. *Neuroimage*, 15(1):273–289, 2002.
- [135] M. Vaillant, C. Davatzikos, and R. N. Bryan. Finding 3d parametric representations of the deep cortical folds. In *Mathematical Methods in Biomedical Image Analysis, 1996., Proceedings of the Workshop on*, pages 151–159. IEEE, 1996.
- [136] D. Van Essen. Surface-based approaches to spatial localization and registration in primate cerebral cortex. *NeuroImage*, 23:S97–S107, 2004.
- [137] D. C. Van Essen, H. A. Drury, J. Dickson, J. Harwell, D. Hanlon, and C. H. Anderson. An integrated software suite for surface-based analyses of cerebral cortex. *Journal of the American Medical Informatics Association*, 8(5):443–459, 2001.
- [138] G. S. Wig, T. O. Laumann, and S. E. Petersen. An approach for parcellating human cortical areas using resting-state correlations. *Neuroimage*, 93:276–291, 2014.
- [139] K. Worsley, J. E. Taylor, F. Carbonell, M. Chung, E. Duerden, B. Bernhardt, O. Lyttelton, M. Boucher, and A. Evans. Surfstat: A matlab toolbox for the statistical analysis of univariate and multivariate surface and volumetric data using linear mixed effects models and random field theory. *Neuroimage*, 47:S102, 2009.
- [140] B. Yeo, M. Sabuncu, T. Vercauteren, N. Ayache, B. Fischl, and P. Golland. Spherical demons: Fast diffeomorphic landmark-free surface registration. *IEEE Transactions on Medical Imaging*, 29(3):650–668, 2010.
- [141] A. Zaharescu, E. Boyer, K. Varanasi, and R. Horaud. Surface feature detection and description with applications to mesh matching. In *Computer Vision and Pattern Recognition, 2009. CVPR 2009. IEEE Conference on*, pages 373–380. IEEE, 2009.

- [142] K. Zilles, E. Armstrong, A. Schleicher, and H.-J. Kretschmann. The human pattern of gyrification in the cerebral cortex. *Anatomy and embryology*, 179(2):173–179, 1988.
- [143] K. Zilles, E. Armstrong, K. H. Moser, A. Schleicher, and H. Stephan. Gyrification in the cerebral cortex of primates. *Brain, Behavior and Evolution*, 34(3):143–150, 1989.
- [144] K. Zilles, N. Palomero-Gallagher, and K. Amunts. Development of cortical folding during evolution and ontogeny. *Trends in neurosciences*, 36(5):275–284, 2013.